NMR CHARACTERIZATION OF UNFROZEN BRINE VEIN DISTRIBUTION AND STRUCTURE IN FROZEN SYSTEMS

by

Peng Lei

A dissertation submitted in partial fulfillment
of the requirements for the degree

of

Doctor of Philosophy

in

Chemical Engineering

MONTANA STATE UNIVERSITY
Bozeman, Montana

May 2022

DEDICATION

To my wife Zhou Ye, my daughter Layla Lei, and my parents.

TABLE OF CONTENTS

TABLE OF CONTENTS CONTINUED

TABLE OF CONTENTS CONTINUED

LIST OF TABLES

Table Page

LIST OF FIGURES

Figure Page

LIST OF FIGURES CONTINUED

Figure Page

LIST OF FIGURES CONTINUED

ABSTRACT

The liquid vein network (LVN) that forms in the interface of ice crystals or particles exists in frozen porous media due to the freezing point depression. The distribution and structure of the LVNs are dynamic due to the ice recrystallization phenomenon. In ice alone, the LVNs formed by the ice crystal interfaces can be characterized as a porous medium in terms of surface to volume ratio (S/V) and the tortuosity (α).The presence of solid particles or ice-binding proteins (IBPs) make the frozen system much more complex. The research presented uses nuclear magnetic resonance (NMR) experimental techniques, including magnetic resonance imaging (MRI), relaxation and self-diffusion measurements, to study the development of the LVNs in complex frozen systems containing solid particles or IBPs. Poly-methyl methacrylate (PMMA) particles of diameters 0.4, 9.9, and 102.2 μm are used with brine solution concentrations of 15, 30, and 60 mM Magnesium chloride ($MgCl_2$) to simulate complex frozen systems. The dynamic rearrangement with time of LVNs can be studied as a function of temperature, $MgCl_2$ concentration, and PMMA particle size. The results indicate that small solid particles dominate the structure dynamics while in larger solid particle packed beds the solute effect dominates. This behavior is quantified by determination of S/V and α from NMR relaxation and diffusion data.

Additionally, IBP produced from the V3519-10 organism isolated from the Vostok ice core in Antarctica is added to ice samples frozen from 30, 60 and 120 mM $MgCl_2$ solution to investigate its influence on LVNs over months of aging. The interplay of the solute and biological effects is complicated but it appears the biological effect is more pronounced at lower salt concentrations. The data provide a basis for eventual combination of salt, IBP and solid particulate studies. The result of MRI, relaxation and self-diffusion measurements indicate the inhibition of ice recrystallization as a function of particle size, $MgCl_2$ concentration and the presence of IBP. The non-invasive data presented along with calibration of the relaxation experiments with self-diffusion experiments, demonstrate the continued extension of NMR techniques developed from porous media to frozen porous media and ice LVN structure.

CHAPTER ONE

INTRODUCTION

The research presented in this dissertation investigates the application of nuclear magnetic resonance (NMR) techniques, including relaxation, self-diffusion and magnetic resonance imaging (MRI), to the dynamic liquid vein network (LVN) in complex frozen systems. Due to their non-invasive nature NMR techniques can be used to track the development process of the LVN over long time frame (*i.e.* one and half months) and visualize the change with MRI.

The study of grain coarsening in ice systems is interesting to many industries due to its wide presence in natural and man made systems. Ice recrystallization is common in our daily life: it's the process where tiny ice crystals melt and merge into giant crystals resulting in crystal growth. Human beings take advantage of it, like the invention of the ice maker to produce ice cubes, and be perplexed by it, like trying to find a way to inhibit the formation of big ice crystals in ice cream (Donhowe et al., 1991). Ice recrystallization phenomena indicates that the ice structure is complex and dynamic, primarily when impurities and other particles are present. A geophysical example is the formation of ice lens inside soil during the winter (Beskow, 1947). With the proper temperature, specific soil, and impurities, the ice inside the soil layer may move and merge, forming one or several ice lenses, which changes the structure of the soil layer and causes frost heave causing damage to building foundations, roadways and other built environments (Beskow, 1947; Rempel, 2007). To solve this kind of problem caused by ice, it's essential to study the dynamic, porous structure formed by ice-particle systems. Laboratory

studies are needed to expand our understanding of the complex freezing behavior in porous systems.

Furthermore, methods to inhibit ice recrystallization are of interest in biotechnology (Qin et al., 2007; Raymond, 2011), and food science applications (Kaleda et al., 2018; Mangiagalli et al., 2020; Zhu et al., 2019). In this research, NMR techniques were used to measure unfrozen water content, surface area to volume ratio (S/V) and tortuosity of the LVNs in ice-particle mixtures at different temperatures and salt concentrations. NMR relaxation using the Carr-Purcell-Meiboom-Gill (CPMG) method and diffusion by the Pulsed Gradient Spin Echo (PGSE) method were used to probe the freezing behavior of $MgCl_2$ saturated porous media comprised of model PMMA spheres. MRI was used to visualize the internal structure of the frozen porous media non-destructively over time and at various temperatures. The role of biological activity in geophysical and biotechnology cryopreservation systems was studied using a recombinant ice binding protein (rIBP) isolated from an organism recovered from the deep Vostok ice core (Christner et al., 2001; Wang et al., 2016; Wang et al., 2017). The rIBP acts as an ice crystal growth regulator in the ice brine systems (Raymond and DeVries, 1977).

The current study investigates the changing structure of the liquid vein network under varying conditions: salinity, solid particulate porous media, temperature and biological protein. Two topics are focused on: 1) the unfrozen brine vein distribution and structure in model-packed beds; and 2) the influence of ice-binding protein on the liquid vein network in frozen porous media. The first studies explore the ice recrystallization process in the different model-packed beds and discuss the LVNs development as a function of temperature ($-17.4℃$ to $3.6℃$), particle size (0.4, 9.9, and 102.2 μm) and brine concentration (15, 30, and 60 mM $MgCl_2$). The

second study investigates the recrystallization inhibition due to IBP activity over one and half months. In this way, we explore the application of advanced NMR in frozen media to gain a better understanding of ice-related coarsening and dynamics related to: food science (Mangiagalli et al., 2020; Zhu et al., 2019), frost heave (Beskow, 1947; Rempel, 2007), cell preservation (Xu et al., 2012), or even the planetary appplications (*i.e.* ice distribution on Mars) (Sizemore et al., 2015; Stillman et al., 2014).

Outline

Chapter 2 introduces the basic theory of NMR. An overview of quantum mechanics of NMR is provided. The classical mechanics concepts from excitation to signal detection and the spin relaxation mechanisms are presented. Basic pulse sequences, including inversion recovery, spin-echo and Carr-Purcell-Meiboom-Gill (CPMG) sequence applied in the research are discussed. More advanced NMR concepts are introduced in Chapter 3, including MRI and the basics of self-diffusion measurements, consisting of translational motion encoding, the Stejskal-Tanner experiment, restricted diffusion, Brownstein-Tarr relations and diffraction. The variables that influence the structure of the unfrozen vein network in the frozen system, the ice recrystallization phenomenon and the data analysis methods are discussed in Chapter 4.

The result of NMR characterization of the unfrozen brine vein distribution and structure in model packed beds composed of polymer spheres as a function of temperature, particle size, and salt concentration are presented in Chapter 5. While small solid particles (9.9 μm) introduced high curvature, the unfrozen water content in frozen model packed beds is primarily contributed to by the wetting film between the particle surfaces due to the curvature.

Comparatively, the solute effect is the dominant source of the unfrozen water content in the packed beds with large solid particles (102.2 μm). CPMG and PGSE methods were used to probe the dynamic variation of LVNs by tracking the change of the S/V and tortuosity α. The results quantify inhibition of ice recrystallization as a function of particle size (Lei et al., 2022) (Cold Regions Science and Technology accepted). The LVNs are relatively stable for small particles as the solid particle matrix restricts ice crystal growth. The boundary of the large particles limits the growth of the ice crystals imposing a length scale structure. This work has been accepted in *Cold Regions Science and Technology* for publication.

Chapter 6 presents novel data on the recrystallization inhibition of IBP in ice samples with different salt concentrations as a function of time. The results quantify the inhibition of ice crystal growth by IBP in terms of characterization of the ice crystals and LVNs as an effective porous media. The unique structure and distribution of LVNs due to the influence of IBP at different liquid water content has been measured and discussed in the context of S/V and tortuosity α. This work is being prepared for submission to the journal Cryobiology.

References

Beskow, G., 1947. Soil freezing and frost heaving with special application to roads and railroads.

Christner, B.C., Mosley‐Thompson, E., Thompson, L.G. and Reeve, J.N., 2001. Isolation of bacteria and 16S rDNAs from Lake Vostok accretion ice. Environmental Microbiology, 3(9): 570-577.

Donhowe, D., Hartel, R. and Bradley Jr, R., 1991. Determination of ice crystal size distributions in frozen desserts. Journal of dairy science, 74(10): 3334-3344.

Kaleda, A., Tsanev, R., Klesment, T., Vilu, R. and Laos, K., 2018. Ice cream structure modification by ice-binding proteins. Food chemistry, 246: 164-171.

Lei, P., Young, M.W., Seymour, J.D., Stillman, D.E., Primm, K., Sizemore, H.G., Rempe, l.W. and Codd, S.L., 2022. NMR Characterization of unfrozen brine vein distribution and structure in model packed beds. Cold Regions Science and Technology.

Mangiagalli, M., Brocca, S., Orlando, M. and Lotti, M., 2020. The "cold revolution". Present and future applications of cold-active enzymes and ice-binding proteins. New biotechnology, 55: 5-11.

Qin, W., Doucet, D., Tyshenko, M. and Walker, V., 2007. Transcription of antifreeze protein genes in Choristoneura fumiferana. Insect molecular biology, 16(4): 423-434.

Raymond, J.A., 2011. Algal ice-binding proteins change the structure of sea ice. Proceedings of the National Academy of Sciences, 108(24): E198-E198.

Raymond, J.A. and DeVries, A.L., 1977. Adsorption inhibition as a mechanism of freezing resistance in polar fishes. Proceedings of the National Academy of Sciences, 74(6): 2589-2593.

Rempel, A., 2007. Formation of ice lenses and frost heave. Journal of Geophysical Research: Earth Surface, 112(F2).

Sizemore, H.G., Zent, A.P. and Rempel, A.W., 2015. Initiation and growth of martian ice lenses. Icarus, 251: 191-210.

Stillman, D.E., Michaels, T.I., Grimm, R.E. and Harrison, K.P., 2014. New observations of martian southern mid-latitude recurring slope lineae (RSL) imply formation by freshwater subsurface flows. Icarus, 233: 328-341.

Wang, C., Oliver, E.E., Christner, B.C. and Luo, B.-H., 2016. Functional Analysis of a bacterial antifreeze protein indicates a cooperative effect between its two ice-binding domains. Biochemistry, 55(28): 3975-3983.

Wang, C., Pakhomova, S., Newcomer, M.E., Christner, B.C. and Luo, B.-H., 2017. Structural basis of antifreeze activity of a bacterial multi-domain antifreeze protein. PLoS One, 12(11): e0187169.

Xu, X., Liu, Y., Cui, Z., Wei, Y. and Zhang, L., 2012. Effects of osmotic and cold shock on adherent human mesenchymal stem cells during cryopreservation. Journal of biotechnology, 162(2-3): 224-231.

Zhu, Z., Zhou, Q. and Sun, D.-W., 2019. Measuring and controlling ice crystallization in frozen foods: A review of recent developments. Trends in Food Science & Technology, 90: 13-25.

CHAPTER TWO

INTRODUCTION TO NUCLEAR MAGNETIC RESONANCE

Quantum mechanics

Nuclear magnetic resonance relies on the quantum mechanical property of the spin angular momentum. By monitoring the response of the spin angular momentum generated by nuclei in macroscopic systems to a magnetic field, the physical ensemble properties can be studied. The angular momentum quantum number I, which depends on the angular momentum quantum number m, can describe the spin state of nuclei. While I is an integer or half-integer, the discrete value of m is possible in the range $[-I, (-I+1), \ldots, (I-1), I]$. For example, for the hydrogen ^{1}H with $I = 1/2$, there are two possible discrete values for m. Furthermore, these two values indicate two possible spin states of hydrogen ^{1}H: one is a spin-up or parallel state, one is the spin-down anti-parallel state.

While m has different possible values, as the quantum mechanics principle states, a vector space $|\Psi\rangle$ can be used to describe the quantum states, and the general linear superposition can be written as (Callaghan, 2011):

$$|\Psi\rangle = \sum_m a_m \, |m \tag{2.1}$$

while a_m is the probability.

For a single nucleus in a basic state $|m\rangle$, the component of I along the z-axis can be described by the eigenvalue equation:

$$I_z|m\rangle = m|m\rangle \tag{2.2}$$

where I_z is an observable property of interest, m is the eigenvalue after the observation of I_z. It is clear that after the observation, only one state will be observed in the range of eigenvalue, and the expectation value as the result of the measurements is given by:

$$\langle \Psi | I_z | \Psi \rangle = \sum_m |a_m|^2 \, m \tag{2.3}$$

The Schrödinger equation describes the time evolution of a quantum system:

$$i\hbar \frac{\delta}{Ot} |\Psi(t)\rangle = \mathcal{H} |\Psi(t)\rangle \tag{2.4}$$

$\hbar$ is Planck's constant, and $\mathcal{H}$ is the Hamiltonian operator. By ignoring the time influence associated with fluctuating disturbances, $\mathcal{H}$ can be independent of time and can be treated as a constant, and the Schrödinger equation can be solved as:

$$|\Psi(t)\rangle = U(t) |\Psi(0)\rangle \tag{2.5}$$

$$U(t) = \exp(-i\mathcal{H}t) \tag{2.6}$$

where U(t) is the evolution operator.

While an external magnetic field B_0 exists in the direction of gravity, the interaction of the external magnetic field with the nuclear spin will force the nuclei into different possible spin states. While the nucleus has different quantum spin states, the splitting of energy levels happens since there is an energy difference between these two energy states. And the Hamiltonian operator can be expressed as:

$$\mathcal{H} = -iB_0 I_z \tag{2.7}$$

And the energy between the two states for the hydrogen is:

$$\Delta E = \gamma \hbar B_0 \tag{2.8}$$

γ is the gyromagnetic ratio, $\hbar$ is plank constant, and B_0 is the applied field. This process is called the Zeeman interaction.

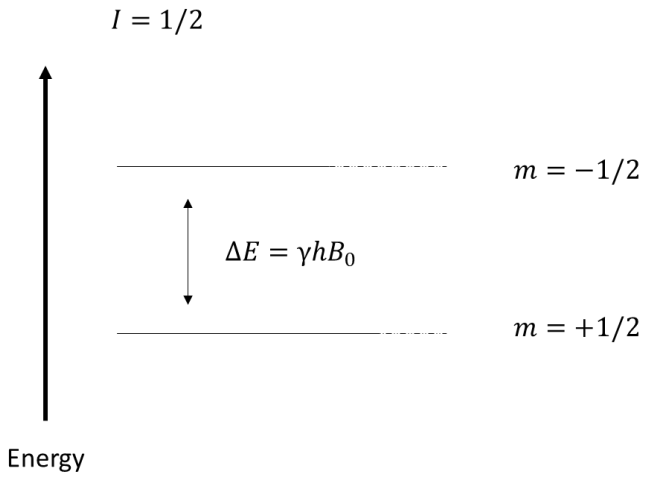

Figure 2.1 Zeeman interaction of spins with $I = 1/2$. The slight preference for the lower energy spin state $m = +1/2$ generates a net magnetization.

All states experience the external magnetic field, and the precession of all states caused by the external magnetic field are at an angular frequency called the Larmor precession

$$\omega_0 = \gamma B_0 \tag{2.9}$$

While in the macro system, the ensemble spins measured with NMR have lots of spins in the different spin states, but they are not equally distributed in each state. Due to the different energy of each spin state, a slight preference of nuclei exists in the lower energy state.

Furthermore, this leads to a net magnetization which can be observed. At equilibrium, the possibility of the nuclei and electrons in these two states is predicted by the Boltzmann distribution. In this case, with the known energy gap between these two states ΔE, the static Zeeman interaction in the macro system, can be calculated by the equation:

$$N^+/N^- = \exp(-\Delta E/kT) \tag{2.10}$$

where N^+ and N^- are the number of nuclei in spin-up and spin-down states. Then a net field rises from the different numbers of these two states.

Classical mechanics NMR

Excitation

While those quantum mechanics concepts describe the properties of a single nucleus in microscopic systems, semi-classical mechanics can explain the NMR experiments in macroscopic systems. The summed magnetization of the ensemble of spins is called magnetization vector M (introduced by Bloch in 1946). For a single nucleus, M will precess around the axis of the external magnetic field at the Larmor frequency. We usually define the axis of the external magnetic field as the z-axis in a Cartesian coordinate system and the perpendicular plane as the transverse x-y plane. Since B_0 is much larger than M, along the axis of B_0, it is impossible to detect M. For this reason, a process called excitation is used to move M into the transverse x-y plane by applying a radio frequency pulse at the same frequency as the Larmor frequency to interact with M. This excitation is achieved with a field oscillating magnetic field B_1 in the transverse plane. In a magnetic field, the time evolution of M is expressed as:

$$\frac{dM}{dt} = \gamma M \times B \tag{2.11}$$

By taking B_0 and B_1 into account, B can be described in a Cartesian coordinate system with unit vectors:

$$B = B_1 cos(\omega_1 t)\boldsymbol{i} - B_1 sin(\omega_1 t)\boldsymbol{j} + B_0\boldsymbol{k} \tag{2.12}$$

By combining Equation (2.11), (2.12) and the initial condition $M(0) = M_0 k$, the evolution of M in the laboratory- frame with the external magnetic field and oscillating magnetic field in each Cartesian coordinate axes can be solved:

$$\begin{aligned} M_x &= M_0 sin(\omega_1 t) sin(\omega_0 t) \\ M_y &= M_0 sin\,(\omega_1 t)\, cos(\omega_0 t) \\ M_z &= M_0 cos(\omega_1 t) \end{aligned} \tag{2.13}$$

where $\omega_1 = \gamma B_1$. With the influence of B_0 and B_1, the magnetization vector M precesses with both ω_0 and ω_1 while B_1 is applied. And during this process, the magnetization vector M is moved to the transverse plane after a 90^o tip.

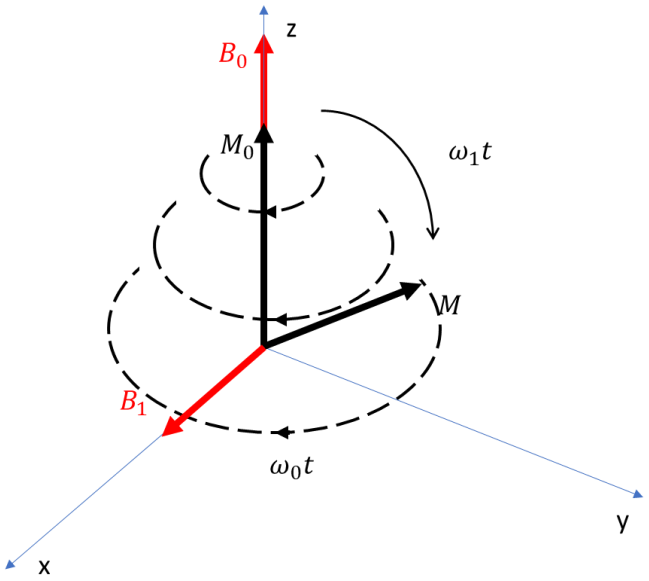

Figure 2.2 M moved to the transverse plane while B_1 is applied. During this process, M precesses about B_0 at ω_0 and around B_1 at ω_1.

To streamline the understanding of the evolution of M, a new coordinate system called a rotating frame is used. By setting the B_1 to oscillate at the Larmor frequency ω_0, and the system is also rotating along the z-axes at the same frequency ω_0, the new equation for M in the rotating frame is:

$$M_x = 0$$

$$M_y = M_0 sin(\omega_1 t)$$

$$M_z = M_0 cos(\omega_1 t) \qquad (2.14)$$

And the process of applying a 90^o pulse in the x-direction to tip M into the transverse plane in the rotating frame is shown in Figure2.3.

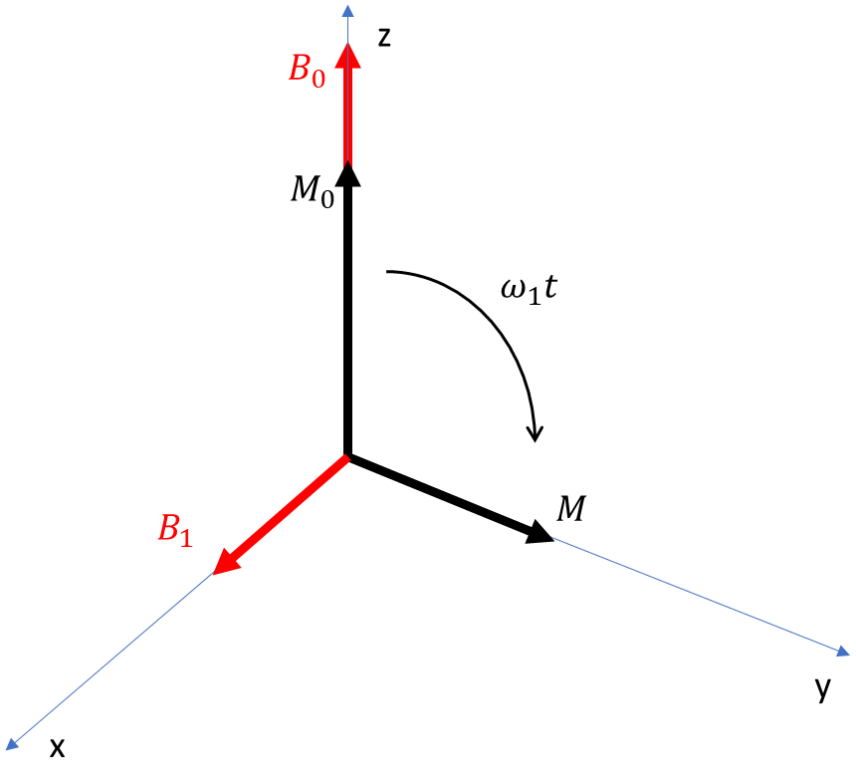

Figure 2.3 M moves to the transverse plane while B_1 is applied in the rotating frame.

Signal detection

After tipping M into the transverse plane, it is possible to detect the precession of M in the RF coil. During this process, net magnetization M returns from a non-equilibrium state to equilibrium. In the transverse plane, it is a decay caused by Transverse Relaxation Spin-Spin T_2, which will be introduced in a later section. The signal arising after the radio-frequency excitation is called the free induction decay (FID). In FID, T_2^* is used instead of T_2 due to the influence of an inhomogeneous magnetic field.

As discussed above, M in the transverse plane can be described as:

$$M(t) = [M_0 cos(\omega_0 t)\boldsymbol{i} + M_0 sin(\omega_0 t)\boldsymbol{j}]\exp\left(\frac{-t}{T_2}\right) \quad (2.15)$$

And by introducing complex notation, M can be rewritten as:

$$M(t) = M_0 \exp(i\omega_0 t)\exp\left(\frac{-t}{T_2}\right) \quad (2.16)$$

And the signal detected from the RF coil during the relaxation is:

$$S(t) = S_0 \exp(i\phi) exp(i\Delta\omega t)\exp\left(\frac{-t}{T_2}\right) \quad (2.17)$$

where S_0 is the initial signal after excitation, ϕ is the receiver phase, and $\Delta\omega$ is the offset frequency between the Larmor frequency and the reference frequency.

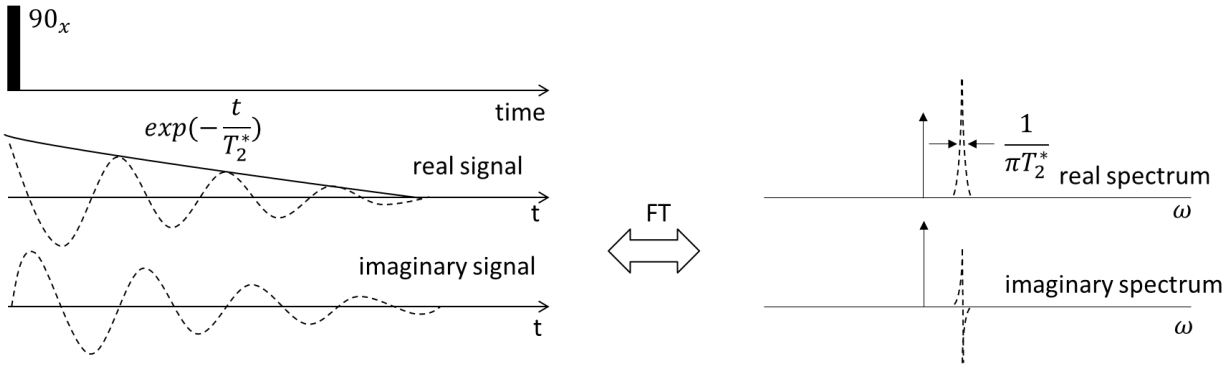

Figure 2.4 The signal from a free induction decay (FID) following a 90º radio frequency pulse has real and imaginary parts in time domain. The real absorption and imaginary dispersion spectra in the frequency domain can be generated after the Fourier transform.

To extract the frequency information from the signal, the mathematic method Fourier transformation is used to transfer the signal from the time domain to frequency domain:

$$\mathcal{F}\{S(t)\} = s(\omega) = \int_{-\infty}^{\infty} S(t)\exp(i\omega t)dt \tag{2.18}$$

The generated spectra are called the absorption and dispersion spectra, respectively. Due to the exponential format of the signal decay in a liquid, the signal's shape in the frequency spectrum is in the shape of Lorentzian. The width of the line shape is associated with the decay rate of the signal. For example, a rapidly decayed signal of FID, which indicates a fast relaxation, generates a broad peak in the frequency spectrum. The full-width-at-half-maximum (FWHM) describes the relationship: $FWHM = {}^{1}/_{\pi T_2^*}$ as shown in Figure 2.4.

Relaxation

Relaxation is the process of the net magnetization M returning from a non-equilibrium state to equilibrium following the RF pulse. The two mechanisms of relaxation are Longitudinal Relaxation Spin-lattice T_1 and Transverse Relaxation Spin-Spin T_2. T_1 relaxation is the process where the net magnetization M returns to its initial maximum value (M_0) parallel to B_0.
T_1 quantifies the rate of transfer of energy from the nuclear spin system to the environment (the lattice). It is the time needed from 0 to 63% of its final value, and notable that the total time needed to fully recover to the equilibrium state is greater than five times that of T_1. The time evolution of M_z in terms of T_1 is

$$M_z(t) = M_z(0) + M_0\left(1 - \exp\left(-\frac{t}{T_1}\right)\right) \tag{2.19}$$

T_2 relaxation is the process where the transverse components of magnetization ($M_{x,y}$) decay or dephase. T_2 quantifies the rate of the decay of the magnetization in the transverse plane. The time evolution of $M_{x,y}$ in terms of T_2 is

$$M_{x,y}(t) = M_{x,y}(0)\exp\left(-\frac{t}{T_2}\right), \tag{2.20}$$

where $M_{x,y}(0)$ is the initial coherent magnetization signal just after applying the RF excitation pulse.

There also exists T_2^* , which is usually shorter than T_2, it is caused by T_2 and any inhomogeneities in the magnetic field, and the dephasing in this situation is quicker.

In the rotating frame, these relationships can be described by the Bloch equations (Bloch, 1946):

$$\frac{dM_x}{dt} = \gamma M_y \left(B_0 - \frac{\omega}{\gamma}\right) - \frac{M_x}{T_2}$$

$$\frac{dM_y}{dt} = \gamma B_1 - \gamma M_y \left(B_0 - \frac{\omega}{\gamma}\right) - \frac{M_y}{T_2} \quad (2.21)$$

$$\frac{dM_z}{dt} = -\gamma M_y B_1 - \frac{M_z - M_0}{T_1}$$

The dominant mechanism for hydrogen T_1 and T_2 relaxation is the dipole-dipole interaction. The spin of the nucleus creates a magnetic moment; therefore, the nucleus can be thought of as a bar magnet, and the magnetic field interaction of two spin nuclei can be called a dipole-dipole interaction. The major factors for the strength of the dipole-dipole interaction are types of spins, the distance between them, the angle between them, and their relative motion (Elster and Burdette, 1994). Types of spins can be proton-proton or proton-electron interactions; the proton-electron dipole interaction is more powerful due to the larger gyromagnetic ratio of the electron; the sixth power of distance has an inversely proportional relationship to the strength, and the quantity $(3\cos^2\theta - 1)$ relates to angle between spins is proportional to the strength. For the last major factors, there are several kinds of relative motions for a couple of spins (change of spin states) as shown in Figure 2.5: $[u - d] \leftrightarrow [d - u]$; $[u - d] \leftrightarrow [u - u]$;$[u - d] \leftrightarrow [d - d]$;$[d - u] \leftrightarrow [d - d]$;$[d - u] \leftrightarrow [u - u]$;$[u - u] \leftrightarrow [d - d]$, where $u =$ up and $d =$ down. Furthermore, the term correlation time τ_c is used to qualify the timeframe associated with the molecular motion of the dipole-dipole interaction. The spectral density

function $J(\omega)$ can be produced by Fourier transforming the correlation function. As shown in Figure 2.5, different types of relative motions lead to different spectral density functions $J(\omega)$.

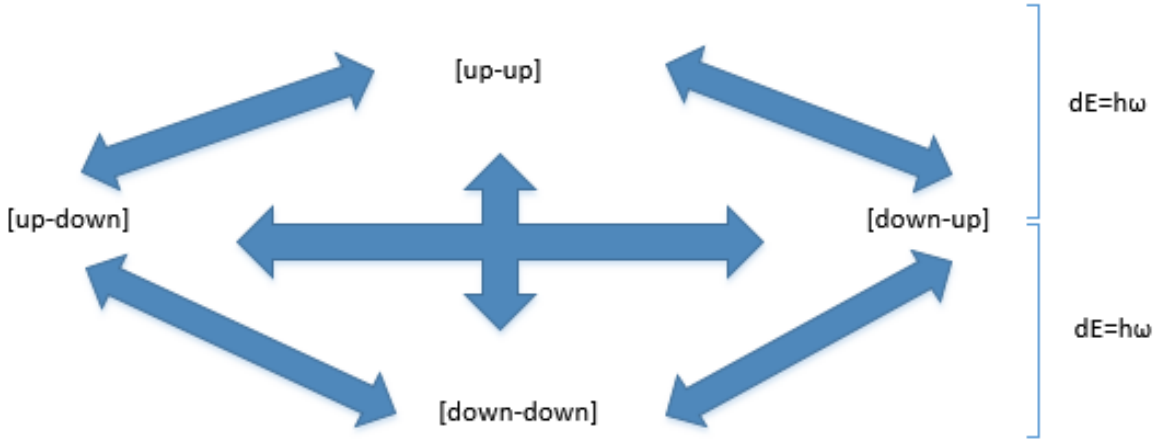

Figure 2.5 The change of spin states for two spin particles.

For the zero-quantum transition, the $J^{(0)}(\omega)$ represents the change of spin states without energy exchange, which is $[u - d] \leftrightarrow [d - u]$, and the molecular rotation frequency ω is zero since the spin state of the coupled spins does not change during this process. This kind of interaction only happens between spin and spin, without any energy release to the surrounding environment, so it is the term that only influences T_2 relaxation. For the single-quantum transition, the $J^{(1)}(\omega)$ represent the change of spin states with energy exchange $\Delta E = \hbar\omega_0$, which is $[u - d] \leftrightarrow [u - u]$, $[u - d] \leftrightarrow [d - d]$, $[d - u] \leftrightarrow [d - d]$ and $[d - u] \leftrightarrow [u - u]$. Moreover, the molecular rotation frequency ω is Larmor frequency ω_0 due to the one spin flip in the coupled spins during this process. For the double-quantum transition, the spectral density

term $J^{(2)}(\omega)$ represents the change of spin states with energy exchange $\Delta E = h(2\omega_0)$, which is $[\mathrm{u}-\mathrm{u}] \leftrightarrow [\mathrm{d}-\mathrm{d}]$. Moreover, the molecular rotation frequency ω is double that of the Larmor frequency ω_0 due to both spins flipping during this process. The spectral density function in these three situations can be described as

$$J^{(0)}(\omega) = \frac{24}{15r_{ij}^6}\frac{\tau_c}{1+\omega^2\tau_c^2}$$

$$J^{(1)}(\omega) = \frac{4}{15r_{ij}^6}\frac{\tau_c}{1+\omega^2\tau_c^2} \qquad (2.22)$$

$$J^{(2)}(\omega) = \frac{16}{15r_{ij}^6}\frac{\tau_c}{1+\omega^2\tau_c^2}$$

where r_{ij} is the distance between the coupled spins i and j.

The functions of T_1 and T_2 relaxation associated with spectral density function $J(\omega)$ are

$$\frac{1}{T_1} = \left(\frac{\mu_0}{4\pi}\right)^2 \gamma^4 \hbar^2 \frac{3}{2} I(I+1)\left[J^{(1)}(\omega_0) + J^{(2)}(2\omega_0)\right] \qquad (2.23)$$

$$\frac{1}{T_2} = \left(\frac{\mu_0}{4\pi}\right)^2 \gamma^4 \hbar^2 \frac{3}{2} I(I+1)\left[\frac{1}{4}J^{(0)}(0) + \frac{2}{5}J^{(1)}(\omega_0) + \frac{1}{4}J^{(2)}(2\omega_0)\right] \qquad (2.24)$$

As shown in Figure 2.6, according to the T_1 and T_2 equations, when the molecular tumbling rate or the inverse of the correlation time equals the Larmor frequency, T_1 is minimized (Callaghan, 2011). For liquids, the molecular tumbling rate is fast as the molecules are more mobile and this leads to a large T_1 and T_2; for solids, the molecular tumbling rate is small due to the fixed molecular lattices, leading to a long T_1 and a very small T_2.

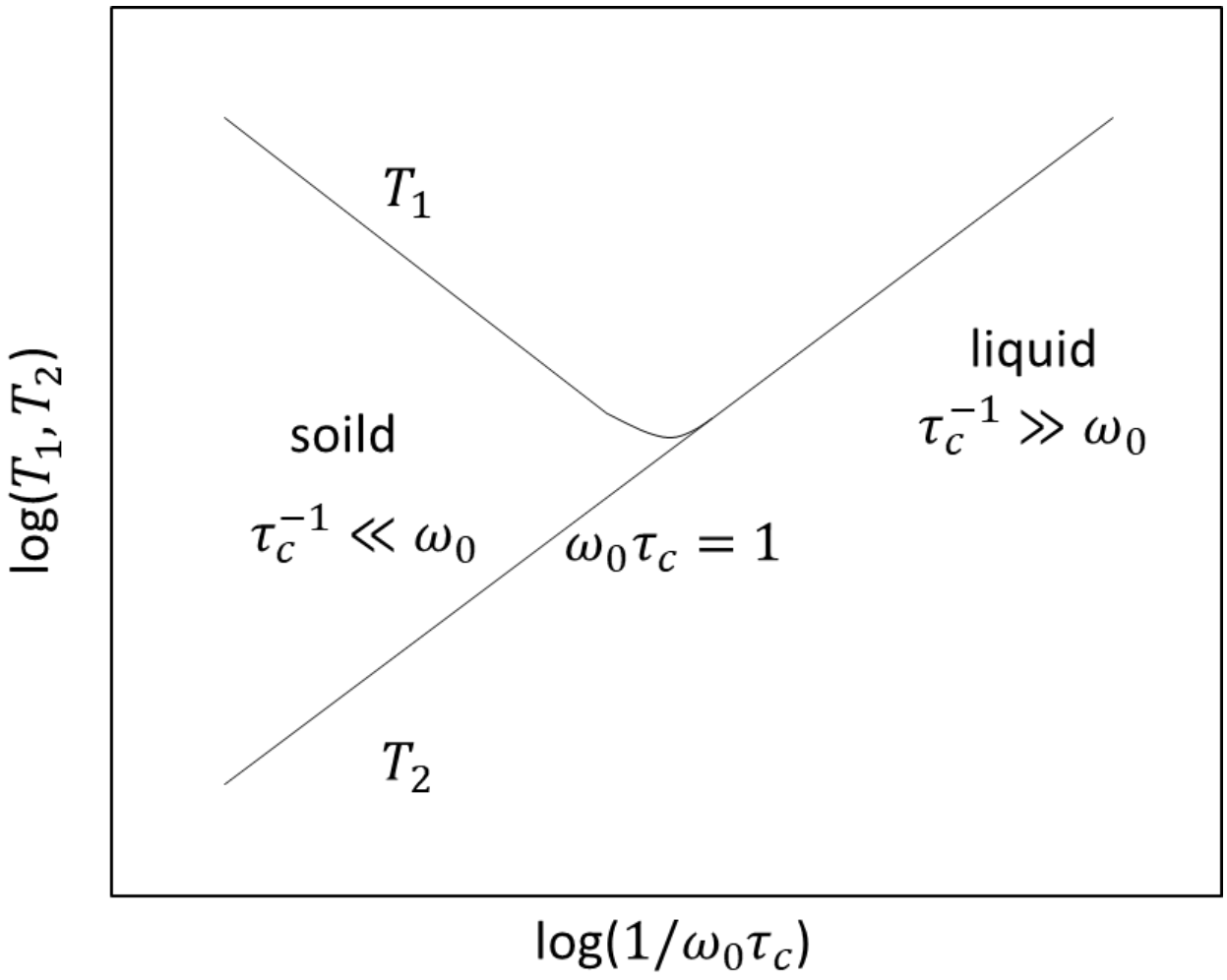

Figure 2.6 T_1 and T_2 relaxation time as a function of correlation time τ_c., The value of T_1 and T_2 varies depending on the mobility of the molecules.

Basic Pulse Sequences

In the signal detection section, it was described how M is tipped to the transverse plane in order to detect it with the RF coil. The FID signal in this situation is a function of T_2^*. When we are interested in other properties, we design different pulse sequences by applying a sequence of RF pulses and magnetic field gradients. In this way, T_1, T_2, diffusion coefficients, and the

internal imaging can be extracted. This is accomplished through magnetization vector rotation with RF pulses and position and motion encoding with magnetic field gradients. In the following sections, the basic pulse sequences are introduced, including the inversion recovery, which is used to measure T_1, the spin echo used as the basis for imaging and diffusion measurements, and the Carr-Purcell-Meiboom-Gill (CPMG) sequence used to measure T_2.

Inversion recovery

T_1 relaxation times are measured by the inversion recovery sequence, as shown in Figure 2.7A. First, a 180^o rf pulse in the x-direction rotates the magnetization vector M from the z-axis to the -z-axis. After this inversion, M begins to decrease due to the spin-lattice relaxation towards equilibrium. Recall that only the signal in the transverse plane can be detected. So, after a variable recovery time (τ), the remaining M is rotated by another 90^o rf pulse in the x-direction into the -y axis and is recorded. During this process, the time evolution of M is described as (Callaghan, 1993):

$$M_z(t) = M_0\left(1 - 2\exp\left(-\frac{t}{T_1}\right)\right) \tag{2.25}$$

As shown in Figure 2.7B, the signal has a crossover from $-M$ to $+M$ at time $\tau = 0.6931T_1$. In this way, the T_1 can be obtained from the inversion recovery measurement.

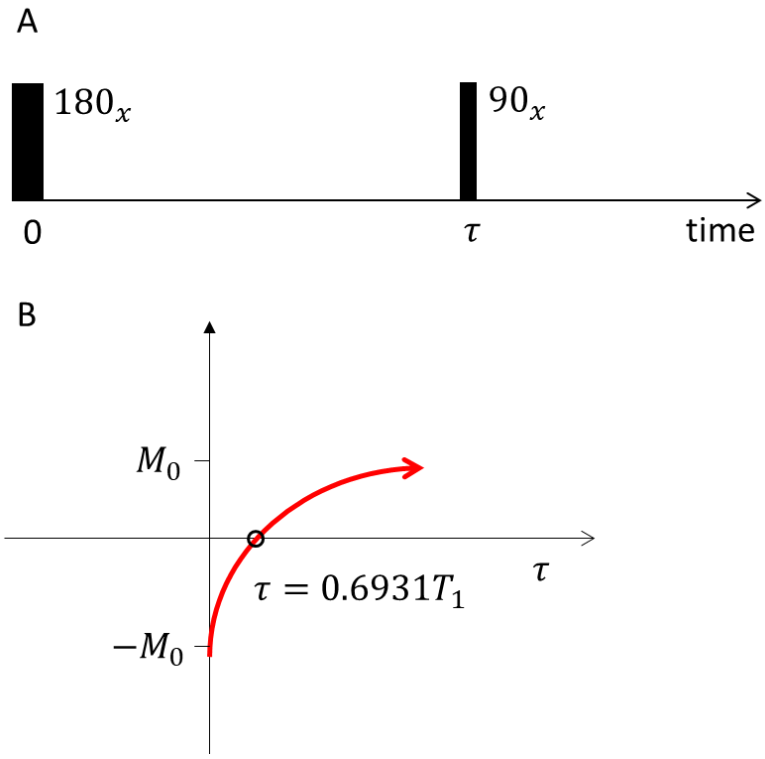

Figure 2.7 A) The inversion recovery sequence. B) Magnetization as a function of the inversion time, τ, in sequence.

Spin Echo

While the M in the transverse plane dephases due to T_2 relaxation and this is non-recoverable, the inhomogeneities of the magnetic field may also cause the dephase of spins and this is partially recoverable with the spin echo. As the magnetic field is not perfectly uniform due to local field variations, the spins in these local fields have different frequencies compared distributed about the Larmor frequency. This enhances the dephasing process. Even with significant improvement of the NMR equipment over the several decades, a uniform magnetic field is still not possible due to structural variations within the sample itself. In 1950, Erwin

Hahn overcame this issue by discovering the phase coherence loss due to inhomogeneous magnetic fields is reversible with a 180° pulse (Hahn, 1950). As shown in Figure 2.8, this technique is called spin echo or Hahn echo, which is widely used today. A 180° rf pulse in the x-direction is applied following the 90° rf pulse after a variable time τ. In this case, much of the dephasing caused by the local field variation is reversed, and most spins converge back to form an echo at 2τ.

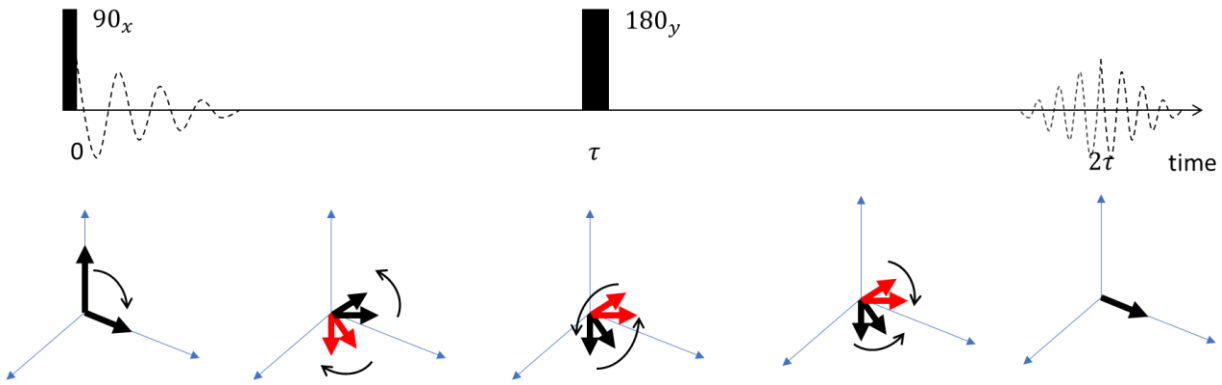

Figure 2.8 The spin-echo pulse sequence. The 180° rf pulse at time τ reverses the dephase and makes the magnetization refocus at time 2τ.

Carr-Purcell-Meiboom-Gill sequence

By using the spin echo, the influence of the inhomogeneous magnetic field can be reduced or even eliminated. With a chain of repeating 180° rf pulses separated by 2τ, a series of spin echoes forms, and the magnetization amplitude at the center of each echo decays by spin-spin relaxation only.

$$M_{x,y}(t) = M_{x,y}(0)\exp\left(-\frac{t}{T_2}\right), \tag{2.26}$$

As shown in Figure 2.9, the sequence developed by Carr and Purcell and modified by Meiboom and Gill is called CPMG sequence and used to measure T_2 (Carr and Purcell, 1954; Meiboom and Gill, 1958).

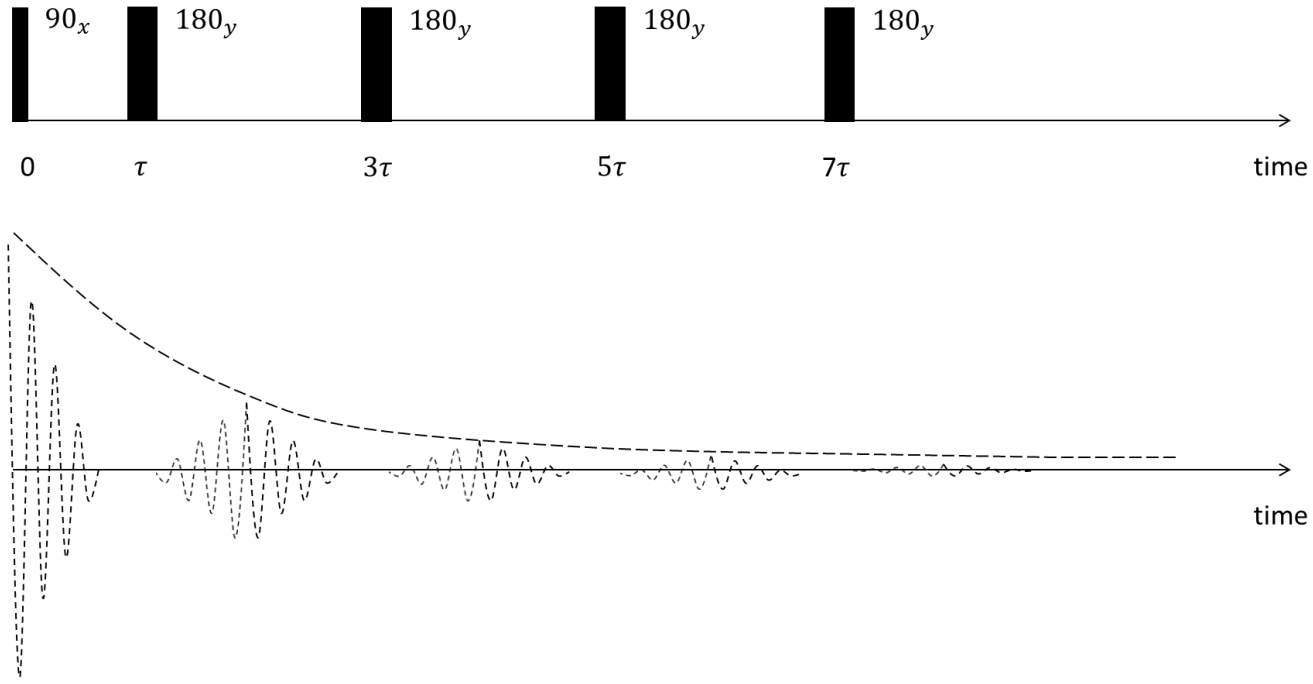

Figure 2.9 Carr-Purcell-Meiboom-Gill sequence employs a series of 180^o rf pulse to generate a chain of echoes.

References

Bloch, F., 1946. Nuclear induction. Physical review, 70(7-8): 460.

Callaghan, P.T., 1993. Principles of nuclear magnetic resonance microscopy. Oxford University Press on Demand.

Callaghan, P.T., 2011. Translational dynamics and magnetic resonance: principles of pulsed gradient spin echo NMR. Oxford University Press.

Carr, H.Y. and Purcell, E.M., 1954. Effects of diffusion on free precession in nuclear magnetic resonance experiments. Physical review, 94(3): 630.

Elster, A.D. and Burdette, J., 1994. Questions and Answers in Magnetic Resonance Imaging, Mosby, St. Louis, MI.

Hahn, E.L., 1950. Spin echoes. Physical review, 80(4): 580.

Meiboom, S. and Gill, D., 1958. Modified spin‐echo method for measuring nuclear relaxation times. Review of scientific instruments, 29(8): 688-691.

CHAPTER THREE

ADVANCED NMR TOPICS

Magnetic Resonance Imaging

When a gradient field $\mathrm{G} = \nabla B$ is applied in a uniform field B_0, the entire field B_{tot} will be changed due to the existence of the gradient field. The absolute value of B_{tot} can be expressed as:

$$B_{\mathrm{tot}} = (r \cdot \nabla B_{\mathrm{x}})i + \big(r \cdot \nabla B_{\mathrm{y}}\big)j + (B_0 + r \cdot \nabla B_{\mathrm{z}})k \tag{3.1}$$

where r is the position. When B_0 is much larger than the gradient field, the gradient in the x-y dimension can be ignored since it only very slightly tilts the direction of B_0 while B_0 is orthogonal to the transverse plane. As shown in Figure 3.1, the Equation 3.1 can be simplified as:

$$|B_{\mathrm{tot}}| \approx B_0 + r \cdot \nabla B_{\mathrm{z}} \tag{3.2}$$

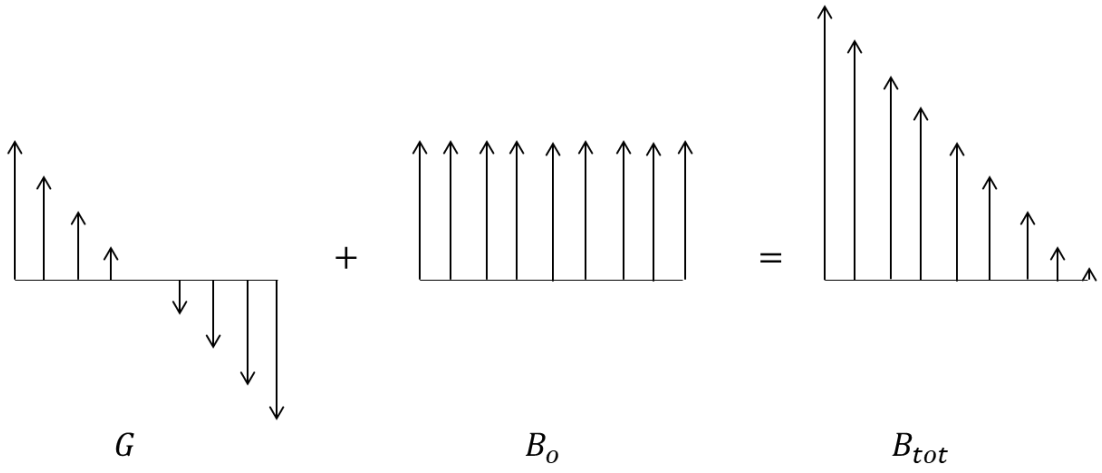

Figure 3.1 When B_0 is much larger than the gradient field, the combination of B_0 and gradient field varies linearly with position.

According to the Larmor equation $\omega_0 = \gamma B_0$, the variation of the magnetic field will also influence the frequency of the precession protons, which can be written as:

$$\omega_0(r) = \gamma B_0 + r \cdot G \tag{3.3}$$

In this case, after applying a gradient field, the Larmor frequency will depend on position. Furthermore, the local magnetization density $M_+(r,t)$ at location r is:

$$M_+(r,t) = M_+(r,0)\, exp(-i\gamma r \cdot Gt) \tag{3.4}$$

By defining a reciprocal space vector k (Callaghan, 2011):

$$k = \gamma Gt/2\pi \tag{3.5}$$

where t is the duration time of the gradient. The phase evolution of any isochromat at position r can be written as:

$$M_+(r,t) = M_+(r,0)\exp(ikr) \tag{3.6}$$

By defining the normalized spin density as $\rho(r)$, which equals to $\frac{M_+(r,t)}{M_+(r,0)}$, then the total normalized signal S_N can be expressed as:

$$S_N(k) = \int \rho(r)\exp(ikr)dr \tag{3.7}$$

Furthermore, the normalized spin density $\rho(r)$ can be solved by Fourier transform of the normalized signal S_N:

$$\rho(r) = \int S_N(k)\exp(-i2\pi kr)dk \tag{3.8}$$

In this case, the nuclear spins are spatially labeled by applying a gradient field. Moreover, the spin density function can be solved for, and the amount of signal at different positions r can be extracted to generate an MR image.

Translational motion encoding

When measuring translational motion, multiple gradients are used. The first gradient is applied with the duration time δ, and then after an observation time Δ , the same gradient is applied again to label the final position; a 180 pulse is applied between the two gradients so that the accumulation of the effective gradients $g^*(t')$ is zero. In this case, the phase shift caused by the first gradient will be reversed by the second one, and an echo will form with the condition:

$$\int_0^t g^*(t')dt' = 0 \tag{3.9}$$

The phase shift for nuclear spin j at time t with a path $r_{\mathrm{j}}(t')$ in the effective gradient $g^*(t')$ is:

$$\varphi_{\mathrm{j}}(\mathrm{t}) = \gamma \int_0^t g^*(t') * r_{\mathrm{j}}(t')dt' \tag{3.10}$$

Furthermore, the path can be expanded by the Taylor series:

$$r_{\mathrm{j}}(t') = r_0 + vt' + \frac{1}{2}at'^2 + H.O.T \tag{3.11}$$

The higher-order terms (H.O.T) are neglected since we are usually interested in location, velocity, and acceleration.

To focus on the phase shift, which is caused by the spin's translational motion in the applied gradient, and to get rid of the relaxation effect, the normalized echo signal is introduced as the ratio of the magnetization with an effective gradient to that without an effective gradient:

$$E(t) = \frac{M_+(t)_{g^*(t')\neq 0}}{M_+(t)_{g^*(t')=0}} = \exp\left(i\varphi_{\mathrm{j}}(t)\right) \tag{3.12}$$

By combining the phase shift equation and the Taylor series expansion of the path into the Equation 3.12, the normalized echo signal can be expressed as:

$$E(t) = \exp\left(i\gamma \boldsymbol{v} \cdot \int_0^t t' g^*(t')dt' + i\gamma \boldsymbol{a} \cdot \int_0^t t'^2 g^*(t')dt'\right) \tag{3.13}$$

Notice that this equation is independent of r_0 as the echo condition requires the accumulation of the effective gradient equals zero. The other two terms are dependent on the velocity and acceleration. In other words, for the zeroth moment:

$$m_0 = \int_0^t g^*(t')dt' = 0 \tag{3.14}$$

The first moment is:

$$m_1 = \int_0^t g^*(t') * t' dt' = g\delta\Delta \tag{3.15}$$

where g is the gradient, δ is the gradient duration time, Δ is the observation time between two gradients.

The second moment is:

$$m_2 = \int_0^t g^*(t') * t'^2 dt' = g\delta^2\Delta \tag{3.16}$$

In this way, by carefully designing the pulse sequence, velocity or acceleration can be measured by making the other moment equal to zero.

Bloch-Torrey equation

Another general approach to identify the spin phase evolution under any time-dependent gradient was made by Torrey (Torrey, 1956). In the Bloch-Torrey equation, the magnetization is treated as a fluid, and a new term representing diffusive replenishment was introduced to modify the Bloch equation:

$$\frac{dM_{\mathrm{x}}}{dt} = \gamma M_{\mathrm{y}}\left(B_0 - {}^{\omega}/_{\gamma}\right) - \frac{M_{\mathrm{x}}}{T_2} + \nabla \cdot \underline{\underline{D}} \cdot \nabla M_{\mathrm{x}} \tag{3.17}$$

where the left-hand side term indicates the rate of change of magnetization over time, and the terms on the right-hand side indicate the rate of change due to precession, transverse relaxation, and diffusive replenishment separately.

By assuming the diffusion coefficient is a scalar and rewriting the equation in the rotating frame, the equation can be simplified as:

$$\frac{\partial M_+}{\partial t} = -i\gamma \mathbf{r} \cdot g^*(t) M_+ - \frac{M_+}{T_2} + D\nabla^2 M_+ - (\mathbf{v} \cdot \nabla) M_+ \tag{3.18}$$

where $M_+ = M_{\mathrm{x}} + iM_{\mathrm{y}}$. Moreover, by introducing a modulation factor $A(t)$, the solution can be expressed as:

$$M_+(r,t) = A(t) \exp\left(-i\gamma \mathbf{r} \cdot \int_0^t g^*(t')dt'\right) \exp\left({}^{-t}/_{T_2}\right) \tag{3.19}$$

It is notable that at the echo center, the echo condition $\int_0^t g^*(t')dt' = 0$ which makes the phase factor term equal to 1 and making $M_+(r,t) = A(t) \exp\left({}^{-t}/_{T_2}\right)$ in the echo center.

Combining the equation of $\frac{\partial M_+}{\partial t}$ and $M_+(r,t)$, the modulation factor $A(t)$ can be expressed as:

$$A(t) = \exp\left(-D\gamma^2 \int_0^t \left(\int_0^{t'} g^*(t'')dt''\right)^2 dt'\right) \exp\left(i\gamma \mathbf{v} \cdot \int_0^t \int_0^{t'} g^*(t'')dt''dt'\right) \tag{3.20}$$

At the echo center where the echo condition applies, $A(t)$ is the same as the normalized echo attenuation $E(t)$. The Bloch-Torrey equation will only be used to evaluate the signal at the echo center.

The Stejskal-Tanner experiment

Stejskal and Tanner (1965)first demonstrated the pulsed gradient spin-echo (PGSE). As shown in Figure 3.2, after the spins are excited with a 90-degree pulse, a gradient with strength g is applied for a period δ to encode the initial position. Then a 180-degree pulse and the same gradient are applied after an observation time Δ so that the gradient encodes the final position, and the 180-degree makes the accumulation of the effective gradients $g^*(t')$zero at the echo center at time 2τ.

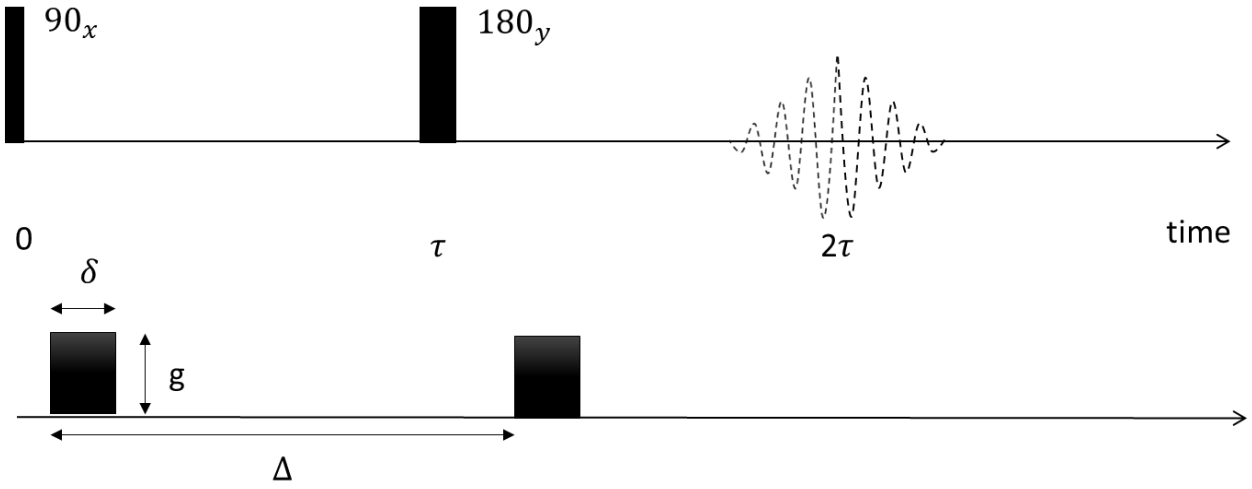

Figure 3.2 PGSE sequence. The spin has a displacement which due to the Brownian motion during the observation time Δ has been recorded in the phase.

While the PGSE sequence meets the echo condition, the flow term and diffusion term of the modulation factor $A(t)$ which is the normalized echo attenuation $E(t)$ can be solved as:

$$\int_0^t \int_0^{t'} g^*(t'')dt''dt' = -g\delta\Delta \tag{3.21}$$

$$\int_0^t \left(\int_0^{t'} g^*(t'')dt'' \right)^2 dt' = g^2\delta^2(\Delta - \delta/3) \tag{3.22}$$

The solution of $A(t)$ generates the Stejskal-Tanner relationship, the normalized echo attenuation, which is the ratio of the echo amplitude at gradient g to that at zero gradient and can be expressed as:

$$E(g) = \frac{S(g)}{S(0)} = \exp(-\gamma^2 g^2 \delta^2 D(\Delta - \delta/3)) \tag{3.23}$$

which means the PGSE can be used to measure the diffusion coefficient D.

The self-diffusion coefficient D is for unrestricted diffusion. For restricted diffusion, the effective diffusion coefficient D_{eff} takes the place of self-diffusion which will be discussed later. To remove the relaxation effects on $E(g)$, the experiment times are fixed while the gradient field amplitude is varied to measure the diffusion coefficient. If the diffusion coefficient is dependent on time, for example, in restricted diffusion, the observation time Δ can be varied.

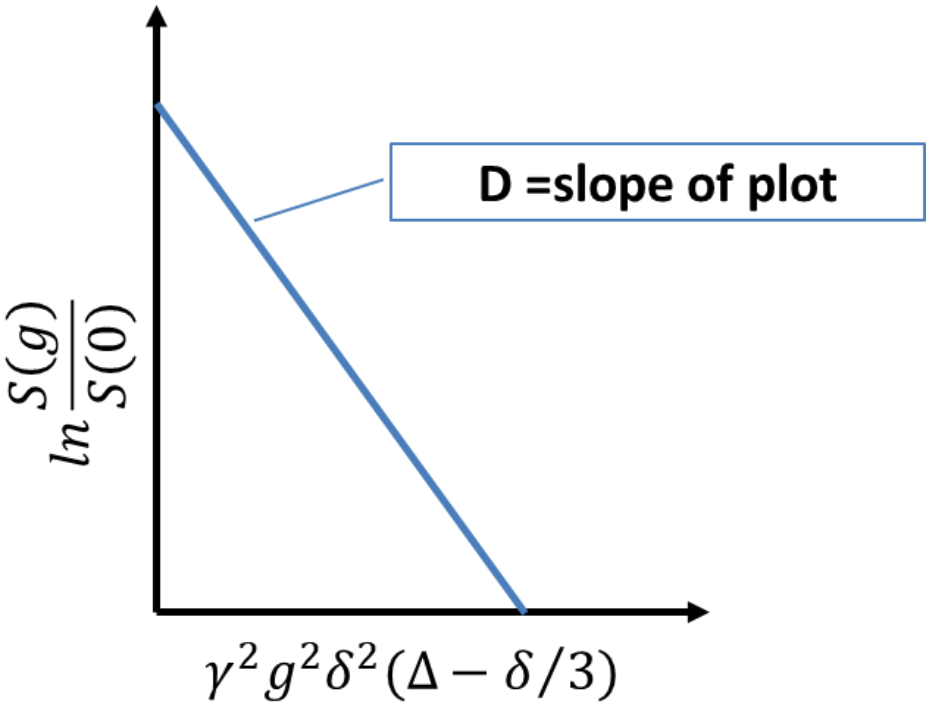

Figure 3.3 Stejskal Tanner Plot with varied gradient field amplitude.

As shown in figure 3.3, while keeping the experiment times constants and varying gradient amplitude, plotting the natural log of the normalized echo attenuation versus $\gamma^2 g^2 \delta^2 D(\Delta - \delta/3)$ allows the diffusion coefficient to be calculated from the Stejskal Tanner Plot.

Bloch-Torrey's approach can describe the equation response for diffusion and flow very well but cannot obtain a closed form expression for more general motions. However, the propagator formalism can be used when the narrow gradient pulse approximation applies. This

approximation requires the duration time δ of the gradient to be approaching zero so that the gradient pulse is narrow enough for us to ignore the motion during the duration time δ. For unrestricted diffusion, the condition can be simplified as $\delta \ll \Delta$.

By defining a reciprocal space variable q:

$$q = \gamma \delta g \tag{3.24}$$

And defining the molecular density function as $\rho(r)$, so that the probability for the spin to move from r to r'during the observation time Δ, the normalized echo attenuation can be expressed as:

$$E(q,\Delta) = \int \rho(r) \int P\,(r|r',t) \exp\big(iq * (r' - r)\big) dr' dr \tag{3.25}$$

By defining the dynamic displacement $R = r' - r$, the averaged propagator is defined as

$$\overline{\mathrm{P}}(R,\Delta) = \int \rho(r) \int P\,(r|r',t) dr \tag{3.26}$$

In one dimension, using $R = Z$, the normalized echo attenuation equation can be rewritten as:

$$E(q,\Delta) = \int \overline{\mathrm{P}}(Z,\Delta) \exp(iqZ) dZ \tag{3.27}$$

In the low q limit, the equation can be expanded in a Taylor Series:

$$E(q,\Delta) \approx 1 + iq \int \overline{P}\,(Z,\Delta) Z dZ - \frac{1}{2} q^2 \int \overline{P}\,(Z,\Delta) Z^2 dZ + \ldots \tag{3.28}$$

When no net flow exists, the molecules only undergo Brownian motion and this equation can be simplified as:

$$E(q,\Delta) \approx 1 - \frac{1}{2} q^2 \langle Z^2(\Delta) \rangle \tag{3.29}$$

Restricted diffusion

The effective diffusion coefficient D_{eff} is a powerful tool to describe restricted diffusion. Using the Sutherland-Einstein definition, the effective diffusion coefficient in one dimension is:

$$D_{\text{eff}}(t) = \frac{\left\langle \left(r(t) - r(0)\right)^2 \right\rangle}{2t} \tag{3.30}$$

which is directly dependent on the mean displacement and the time between two observations.

When there is no boundary, the effective diffusion coefficient D_{eff} is the same as the free diffusion coefficient D_0. However, in porous media, the pore boundary will restrict the diffusion of the molecules.

For example, in a closed pore, the diffusion length $\sqrt{D_0 \Delta}$, is the maximum length a molecule can diffuse during any time Δ.

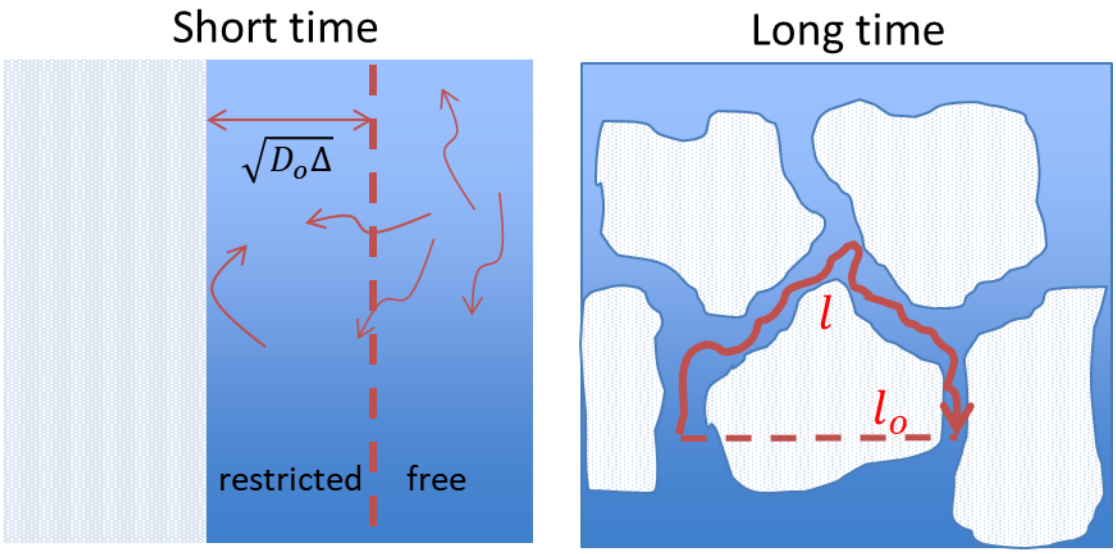

Figure 3.4 Restricted diffusion over short and long time scales in a porous media saturated with water.

Over a short time scale ($\Delta \ll a^2/D_0$, where a is the pore size), the diffusion of the nuclei obeys random Brownian motion except for those molecules near the pore boundary. If the boundary is assumed as a flat wall, for a molecule in the region where the distance to the wall is more than the diffusion length $\sqrt{D_0\Delta}$, it can diffuse freely, and the diffusion coefficient is the same as the free diffusion coefficient D_0. For a molecule in the restricted region where the distance to the wall is within the diffusion length $\sqrt{D_0\Delta}$, it is possible to hit the boundary and reflect during the observation time Δ, as shown in Figure 3.4. In this case, the diffusion coefficient in the restricted region decreases due to the boundary's influence. Furthermore, the slight shift of the effective diffusion coefficient D_{eff} from the free diffusion coefficient D_0 can be used to calculate the fraction of these molecules in different region while it is dependent on the

surface area to volume ratio S/V of the pore and diffusion length $\sqrt{D_0\Delta}$. In other words, S/V and $\sqrt{D_0\Delta}$ have a linear relationship to the D_{eff}. The mean squared displacement measured by PGSE can calculate the effective diffusion coefficients. The relationship between the effective diffusion coefficient D_{eff}, the surface area to volume ratio S/V, and the diffusion length $\sqrt{D_0\Delta}$ in the short-time regime can be expressed as (Latour et al., 1993; Mitra et al., 1993; Mitra et al., 1992):

$$\frac{D(\Delta\rightarrow 0)}{D_0} = 1 - \frac{4}{9\sqrt{\pi}}\frac{S}{V_{\text{p}}}\sqrt{D_0\Delta} \tag{3.31}$$

where D_0 is the constant molecular self-diffusion coefficient, Δ is the observation time.

Over long-time scales, the diffusion of all molecules is limited by the surface of the pores, which means all water molecules have a restricted motion. In this case, the effective diffusion coefficient directly reflects geometric properties of the porous media system (Bear, 1988):

$$\frac{D(\Delta\rightarrow \infty)}{D_o} = \frac{1}{\alpha} = \frac{l_0}{l} \tag{3.32}$$

where α is the tortuosity, the ratio of the path length a molecular travel in the vein l to the geometric path l_0.

When the pore is isolated, the mean squared displacement of nuclei in the pore will be restricted and approach a constant, determined by the pore's size. Due to the definition of the effective diffusion coefficient, while the mean squared displacement remains as a constant, the

effective diffusion coefficient will approach zero in the isolated pore, with the increasing observation time Δ.

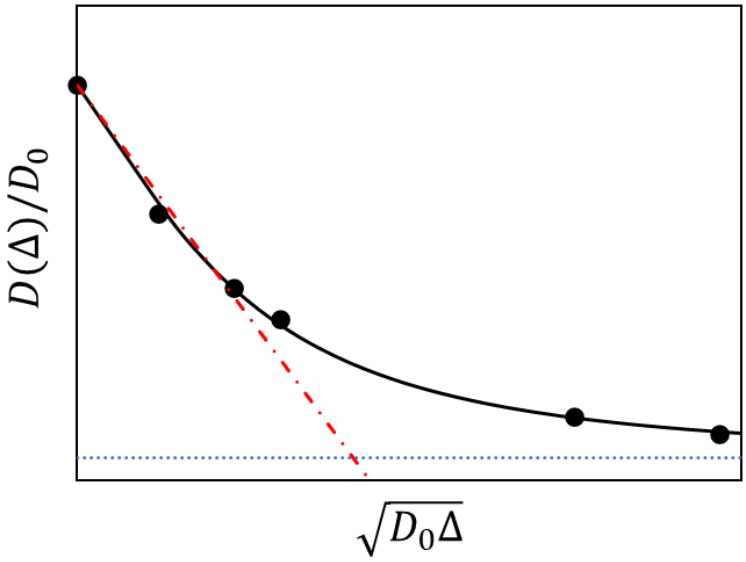

Figure 3.5 Pade approximation. The redline is the approximation line in short time scale to calculate surface area to volume ratio S/V, and the blue line is the approximation line to simulate the long time scale to calculate tortuosity in the porous media.

The observation time Δ cannot extend to infinity for NMR measurement due to relaxation decay. Hence a Pade approximation is used to describe short and long-time scale behavior as shown in Figure 3.5:

$$\frac{D(\Delta)}{D_0} = 1 - \left(1 - \frac{1}{\alpha}\right)\left(\frac{\frac{4}{9\sqrt{\pi}}\frac{S}{V_p}\sqrt{D_0\Delta} + \left(1 - \frac{1}{\alpha}\right)\frac{D_0\Delta}{D_0\theta}}{\left(1 - \frac{1}{\alpha}\right) + \frac{4}{9\sqrt{\pi}}\frac{S}{V_p}\sqrt{D_0\Delta} + \left(1 - \frac{1}{\alpha}\right)\frac{D_0\Delta}{D_0\theta}}\right. \tag{3.33}$$

where a fitting parameter θ is introduced with dimensions of time which varies by the complex structure of different porous media.

Brownstein-Tarr relations

In porous media, the structure and geometry of the sample will also affect spin relaxation. Brownstein and Tarr (1979)solve this problem by treating the magnetization density $M(r,t)$ as a conserved quantity that obeys Fick's Law:

$$D\nabla^2 M(r,t) = \frac{\partial M(r,t)}{\partial t} \tag{3.34}$$

By assuming the boundary condition as that the relaxation will be partially relaxed at the surface of the pore (partially absorbing walls), and the initial condition as that the magnetization density has a uniform initial distribution $M(\boldsymbol{r},0) = M(0)/V$, then the general solution can be written as (Callaghan, 2011):

$$M(t) = M(0)\sum_{n=0}^{\infty} I_n \exp\left(-t/T_n\right) \tag{3.35}$$

Where I_n is the relative contribution, $I_n = a_n \int dr\, u_n$, u_n and T_n are eigenfunctions and eigenvalues. I_n and T_n are dependent on the self-diffusion coefficient D, the pore size a, and the average surface relaxivity ρ over the pore surface. $\frac{\rho a}{D}$ is a dimensionless parameter which is the ratio of the surface relaxation rate to the diffusion rate. When $\frac{\rho a}{D} \ll 1$, the system is in the fast diffusion regime in which the relaxation rate is limited by the surface relaxation on the surface.

In other words, the fast exchange limit is when $\frac{\rho a}{D} \ll 1$, the spins have single exponential decay and the relaxation is dominated by the slowest relaxation rate $\frac{1}{T_0} \sim \rho \frac{S}{V_\mathrm{p}}$ where $\frac{S}{V_\mathrm{p}}$ is the surface to volume ratio of the pore. This regime is mainly used for relaxation in small pores (small a value), or weak surface relaxivity compared to the diffusion coefficient. When $1 < \frac{\rho a}{D} < 10$, it is described as the intermediate regime where the relaxation rate and diffusion rate are of the same magnitude. In this regime, the spins have multi-exponential decay. When $\frac{\rho a}{D} \gg 10$, the system is in the slow diffusion regime where the relaxation rate is limited by the diffusion process to the surface. In this case, the spins have multi-exponential decay, and the relaxation is dominated by the slowest relaxation rate $\frac{1}{T_0} \sim \frac{D}{a^2}$; in other words, the relaxation time corresponds to the time for the protons to move across the pore. These results also satisfy the magnetization density equation: when switching from the fast diffusion regime to slow diffusion regime, the decay switches from a single exponential to multi-exponential, which indicates the change of the I_n value during this process, and the slowest relaxation rate becomes independent of ρ during this process which indicates the change of $\frac{1}{T_\mathrm{n}}$ which is of order $a^2/n^2\pi^2 D$ in the slow diffusion regime. While the longest relaxation time is the most important in PGSE, T_0 is the term of interest. Although it is hard to get an accurate surface relaxivity ρ, the Brownstein-Tarr model is widely used to extract pore-size distributions from multi-exponential relaxation data.

Diffraction

While restricted diffusion is caused by the collision of molecules at the surface of the porous media, with the existence of the reflecting wall, the boundary collisions imprint in $E(\mathrm{g}, \Delta)$, and the phenomena caused by the reflection of the molecules by the wall is called diffusive diffraction.

First, consider the diffusive diffraction in an enclosed pore. When the observation time Δ is great enough, which means, $\Delta \gg \frac{l_s^2}{D_0}$, where D_0 is the free diffusion coefficient, $l_s$is the length scale determined by the pore size, the molecules diffuse inside the enclosed pore many times and will lose 'memory' of their initial position. In this case, the conditional probability can be independent of the initial position r, simply related to the pore geometry, so that the conditional probability can be expressed as: $P(r|r', \Delta \rightarrow \infty) = \rho(r')$

The average propagator with an infinite observation time Δ can be rewritten as:

$$\overline{\mathrm{P}}(Z, \Delta) = \int \rho(r) \int P\,(r|r', t)dr = \int \rho(r) \int \rho\,(r')dr \tag{3.36}$$

And the normalized echo attenuation equation can be rewritten as

$$E(q, \Delta) = \int \rho(r) \exp(-iq * r)\, dr \int \rho\,(r') \exp(-iq * r')dr' = |S(q)|^2 \tag{3.37}$$

where $S(q)$ is the structure factor and is the Fourier transform of the density function $\rho(r)$.

Assuming the pore is a rectangular box with length a, the $\rho(r)$ has a uniform distribution over the length a which is a hat function, which makes $S(q)$ a sinc function and the $E(q,\Delta)$ can be written as:

$$E(q,\Delta) = \frac{2 * (1 - cos(qa))}{(qa)^2} \tag{3.38}$$

Which proves $E(q,\Delta)$ is influenced by the geometry of the pore. It is notable that $E(q,\Delta)$ is independent of D_0 and Δ while Δ is approaching infinity.

In the real world, it is hard to guarantee Δ is large enough to assume it is infinite, especially when the size of the pore is large, or the pores are interconnected and the surface of the pore also cannot be assumed to be a perfectly reflecting wall. However, the diffraction phenomenon can just be observed while Δ is finite. By introducing the absorbing ratio of the wall $\bar{\rho}$ and using the different initial conditions and boundary condition for different pore models, the $E(q,\Delta)$ can be solved.

References

Bear, J., 1988. Dynamics of fluids in porous media. Courier Corporation.

Brownstein, K.R. and Tarr, C., 1979. Importance of classical diffusion in NMR studies of water in biological cells. Physical review A, 19(6): 2446.

Callaghan, P.T., 2011. Translational dynamics and magnetic resonance: principles of pulsed gradient spin echo NMR. Oxford University Press.

Latour, L.L., Mitra, P.P., Kleinberg, R.L. and Sotak, C.H., 1993. Time-Dependent Diffusion Coefficient of Fluids in Porous Media as a Probe of Surface-to-Volume Ratio. Journal of Magnetic Resonance, Series A, 101(3): 342-346.

Mitra, P.P., Sen, P.N. and Schwartz, L.M., 1993. Short-time behavior of the diffusion coefficient as a geometrical probe of porous media. Physical review. B, Condensed matter, 47(14): 8565.

Mitra, P.P., Sen, P.N., Schwartz, L.M. and Le Doussal, P., 1992. Diffusion propagator as a probe of the structure of porous media. Physical review letters, 68(24): 3555.

Stejskal, E.O. and Tanner, J.E., 1965. Spin diffusion measurements: spin echoes in the presence of a time‐dependent field gradient. The journal of chemical physics, 42(1): 288-292.

Torrey, H.C., 1956. Bloch equations with diffusion terms. Physical review, 104(3): 563.

CHAPTER FOUR

INTRODUCTION TO ICE PARTICLE MIXTURE

A porous medium saturated by water below its bulk freezing point is a complex system in terms of interacting physical processes. It is composed of solid particles that form the porous medium, ice, and residual water. For a pure system, the ice can be treated as a porous medium with water in the veins formed by the edge of the ice crystals. Many porous media saturated by liquid in cold temperatures can be found in the real world. For example, the formation of an ice lens in the regolith. During the winter, the regolith (soil layer) can be divided into three layers: the dry layer without any ice/water on top, the ice/water-saturated layer on bottom, and the interfacial layer ice table (Bramson et al., 2015).

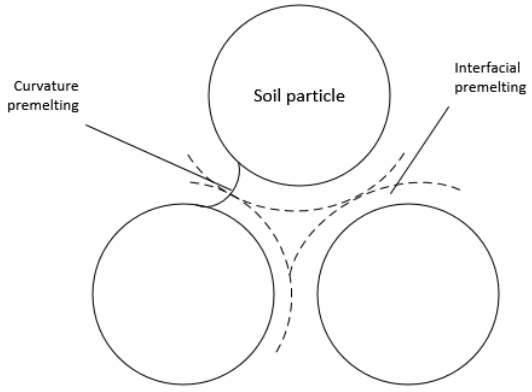

Figure 4.1 Interfacial premelting and curvature premelting around soil particles.

At equilibrium Thermodynamics requires the minimization of the Gibbs free energy. To minimize the Gibbs free energy in the ice table and ice/water-saturated layer, an unfrozen layer between ice and soil particles must exist when the interfacial or surface energy $\gamma_{\text{ice-soil}} > \gamma_{\text{ice-water}} + \gamma_{\text{water-soil}}$ (Rempel, 2012; Sizemore et al., 2015). An additional effect, the Gibbs-Thomson effect, is due to the presence of small particles whose curvature require higher energy due to the positive interfacial energy increasing the chemical potential energy, which means smaller crystals melt at lower temperatures than larger crystals (Defay et al., 1966; Gregg et al., 1967). As shown in Figure 4.1, these phenomena are known as premelting, as the generate melting below the liquid freezing point (Dash, 1989; Rempel, 2012). Although the pressure and temperature in soil during the winter make conditions for which liquid water should not be present, the premelting water still exists and is mobile. A primary mechanism of ice lens formation is called cryosuction, which occurs due to the existence of temperature gradients which breaks the equilibrium state of the system consisting of ice, regolith, and unfrozen brines. This leads to the rise of a net force, which leads to the migration of premelting water in the network and the formation of an ice lens which causes frost heave as shown in Figure 4.2 (Sizemore et al., 2015).

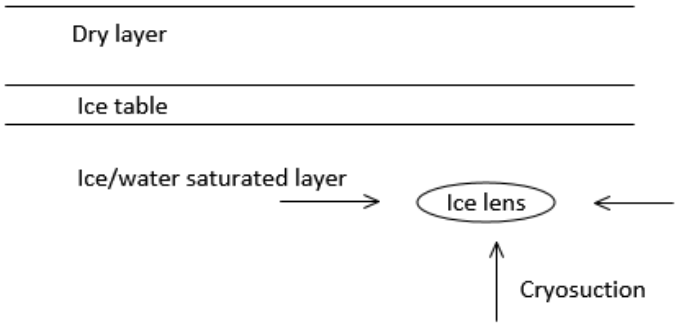

Figure 4.2 Water migrates through soil pores by capillary action.

Laplace Pressure

Due to the repulsion and attraction of molecules to each other, molecules at an interface or surface are pulled outwards or inwards, which leads to a pressure difference between the two sides of the surface, called the Laplace pressure. Laplace pressure can be calculated from the derivative of Helmholtz free energy A:

$$dA = -\Delta P dV - SdT + \gamma dA_{\mathrm{s}} \tag{4.1}$$

where ΔP is pressure difference, V volume, s entropy, T temperature, γ surface tension, and A_{s} the interfacial surface area. At equilibrium, dA and dT are both zero and Equation 4.1 can be rearranged as

$$\Delta P = \frac{\gamma dA_{\mathrm{s}}}{dV} \tag{4.2}$$

where ΔP is the Laplace pressure.

Considering a geometric model for the ice-regolith mixture, the regolith particles can be modelled as spherical. For a thin layer of water around the ice crystal, by modelling the ice crystal as a sphere with radius R and the thickness of the water layer as d, Equation 4.2 can be written as (De Gennes et al., 2004):

$$\Delta P = \gamma \left(\frac{1}{R} + \frac{1}{R + d} \right) \tag{4.3}$$

Gibbs-Thomson effect

In the liquid-solid system, more energy is required to form small crystals due to the high curvature so that small crystals melt at a higher temperature than big crystals. This effect is called the Gibbs-Thomson effect and is described by the mechanism of supercooling. Without pre-existing solids to freeze on, the freezing temperature is lower than the melting point due to the high chemical potential of tiny crystals. To calculate the melting point depression due to the Gibbs-Thomson effect, two systems can be considered: system A with pure liquid and a layer of the flat solid inside (so that no melting point depression is caused by curvatures) at melting point T_m, and system B with the same conditions except solids exist inside the liquid. Comparing these two systems, the melting point of system B $T_m{}'$ will be lower than that of system A, T_m.

At T_m, for system A, the solids and liquid are in equilibrium, which means they have the same chemical potential:

$$\mu_\mathrm{l}(T_\mathrm{m}) = \mu_\mathrm{s}(T_\mathrm{m}) \tag{4.4}$$

At $T_\mathrm{m}{}'$, for system B, the solids and liquid are also in equilibrium:

$$\mu_\mathrm{l}(T_\mathrm{m}{}') = \mu_\mathrm{s}(T_\mathrm{m}{}', P) \tag{4.5}$$

From the Gibbs-Duhem equation

$$d\mu = -sdT + VdP \tag{4.6}$$

Defining the melting point difference as $\Delta T_0 = T_\mathrm{m} - T_\mathrm{m}'$, and assuming the pressure difference at the liquid-solid boundary ΔP is the disjoining pressure $\Pi(d)$, by combining Equations 4.4 to 4.6 the Gibbs-Thomson Equation can be written as (Rempel, 2012):

$$\Delta T_0 = \frac{T_\mathrm{m}\Pi(d)}{\rho_\mathrm{s}\Delta H} \tag{4.7}$$

where d is the thickness of the interface film, ρ_s is the solid density, ΔH is the enthalpy of fusion.

In the situation where a thin layer of water covers the ice crystal, the melting point difference can be described by combining Equation 4.7 and Equation 4.3:

$$\Delta T_0 = \frac{V_\mathrm{s}\Delta P}{\Delta_\mathrm{fus}S} = \frac{T_\mathrm{m}}{\rho_\mathrm{s}\Delta H}\gamma\left(\frac{1}{R} + \frac{1}{R+d}\right) \tag{4.8}$$

In reality, multiple ice crystals and soil particles coexist, and the shape and size of the particle and ice may vary. In this case, the relationship between the melting point depression, the size of ice crystals and soil particles, the surface tension of the interface, and the thickness of the premelting layer is much more complicated.

Curvature

Equation 4.7 comes from the comparison of systems with or without a flat layer of solid and can only be used to describe the planar liquid-solid interface; to describe more general cases

with different shapes and sizes of the solid, the term mean-curvature k of the liquid-solid interface is introduced (Rempel et al., 2001):

$$\rho_{\mathrm{s}}\Delta H\frac{\Delta T}{T_{\mathrm{m}}}=\gamma_{\mathrm{ls}}k+\Pi(d) \tag{4.9}$$

where ΔT is the temperature below the melting point $\Delta T=T_{\mathrm{m}}-T$. This equation describes the relationship between ΔT, mean-curvature k, and layer thickness d. For example, when d is large (small $\Pi(d)$), and k is large enough (high curvature) that $\Pi(d)\ll\ \gamma_{ls}k$, the melting point depression caused by the disjoining pressure is much lower than that caused by curvature (Rempel, 2012).

Impurities

Equation 4.9 is relevant for the ice-liquid system, and assumes all the ice or liquid is pure water. However, in most systems there are always some impurities such as salts dissolved in the water for ice-particle mixtures. The impurities will cause a further melting point depression, the well-known colligative effect, and the relationship can be written as

$$T_{\mathrm{m}}=T_{\mathrm{m0}}-\Gamma C \tag{4.10}$$

where T_{m0} is the bulk melting point for the pure system, Γ is the liquidus slope and C is the impurity concentration in the vein water (Rempel, 2012). Since the ice lattice will reject the impurities, most of the impurities exist in the water instead of the ice lattice, the bulk concentration of impurities in the water and ice C_{B}, *i.e.* the concentration in the solution if all ice

is melted, is much lower than C, and is approximated as $C_{\mathrm{B}} \approx S_{\mathrm{l}} C$ where S_{l} is the liquid saturation which is defined as the ratio of the total volume of the liquid over the pore volume (Andersland and Ladanyi, 2013). In this case, by defining $\Delta T_{\mathrm{f}} = T_{\mathrm{m0}} - T$, Equation 4.9 can be rearranged as (Rempel, 2012):

$$\Delta T_{\mathrm{f}} \approx \frac{T_{\mathrm{m}}}{\rho_{\mathrm{s}} \Delta H}\left(\gamma_{\mathrm{ls}} k + \Pi(d)\right) + \Gamma \frac{C_{\mathrm{B}}}{S_{\mathrm{l}}} \tag{4.11}$$

Thermodynamic Buoyancy Force

Equation 4.11 describes the relationship between temperature, curvature, disjoining force, impurity concentration, and liquid saturation. Rearranging it and integrating the disjoining pressure over the ice-liquid interface dS, the net disjoining force caused by melting temperature variation can be written as (Rempel, 2012):

$$F_{\mathrm{T}} = -\int \Pi(d)\, dS \approx -\int [\frac{\rho_{\mathrm{s}} \Delta H}{T_{\mathrm{m}}}\left(\Delta T_0 - \Gamma \frac{C_{\mathrm{B}}}{S_{\mathrm{l}}}\right) - \gamma_{\mathrm{ls}} k] dS \tag{4.12}$$

For the flat ice-liquid interface, k is zero, and Equation 4.12 can be simplified as (Rempel, 2012):

$$F_{\mathrm{T}} = -\frac{\rho_{\mathrm{s}} \Delta H A_S}{T_{\mathrm{m}}} \vec{n}\left(\Delta T_0 - \Gamma \frac{C_{\mathrm{B}}}{S_{\mathrm{l}}}\right) \approx -\frac{\rho_{\mathrm{s}} \Delta H A_S}{T_{\mathrm{m0}}} \vec{n}(T_{\mathrm{m}} - T) \tag{4.13}$$

where A_S is the interface area, $\vec{n}$ is the unit outward normal to the ice surface, and approximating $\frac{\rho_{\mathrm{s}} \Delta H}{T_{\mathrm{m}}} \approx \frac{\rho_{\mathrm{s}} \Delta H}{T_{\mathrm{m0}}}$. For the closed ice-liquid interface (liquid water present in an isolated pore), the

integration of k vanishes, and assuming γ_{ls} a constant, Equation 4.12 can be transformed to the integration over the enclosed volume V (Rempel, 2012):

$$F_{\mathrm{T}} = -\int \nabla[\frac{\rho_{\mathrm{s}}\Delta H}{T_{\mathrm{m}}}(T_{\mathrm{m}} - T)]dV \approx \frac{\rho_{\mathrm{s}}\Delta H}{T_{\mathrm{m0}}}\int GdV \tag{4.14}$$

where $G = \nabla(T - T_{\mathrm{m}})$ and again approximating $\frac{\rho_{\mathrm{s}}\Delta H}{T_{\mathrm{m}}} \approx \frac{\rho_{\mathrm{s}}\Delta H}{T_{\mathrm{m0}}}$.

Equations 4.12, 4.13, and 4.14 express the relationship between the temperature and thermodynamic buoyancy force by integrating the disjoining force over the ice-liquid interface and disjoining pressure is expressed by rearranging Equation 4.11. Notably, the interactive force between the ice, water, and solid particles can also represent the disjoining pressure. Equation 4.3 gives a simple example by assuming the disjoining force is only from the Laplace pressure. Equation 4.8 shows the relationship between crystal size, water film thickness, and melting point depression. With Equation 4.3, it's clear that with a smaller grain size R and water layer thickness d, the disjoining pressure has a larger value, increasing the chemical potential. Therefore, the value of the thermodynamic buoyancy force is more significant when the particle size is smaller. With Equation 4.7, it's clear that a higher disjoining pressure will lead to higher melting point depression, which means the total water content should be greater with a smaller particle size. In summary, during the ice recrystallization process, the smallest ice crystals melt, and water migrates due to the net force through the vein network. In the end, a larger crystal grows through the consumption of the tiny ice crystals, the classical coarsening problem of physics. In the real world, the disjoining pressure more complicated, and the Laplace pressure is only a part of it. For example, when there are mineral particles, the interface may be charged, which introduces a double layer force caused by an electrical potential, which will make the

system interfacial molecular interaction more complicated (Rempel, 2012). In this case, we usually do not describe the disjoining pressure directly but express it by rearranging Equation 4.11.

Unfrozen Brine Vein Distribution and Structure in Model Packed Beds

To study the structure of the ice-particle mixture with unfrozen brine inside as a function of temperature, three variables were measured in packed beds frozen with different concentration brine solutions to describe the structure and distribution of the unfrozen brine vein network:

(1) Unfrozen water content ϕ_{w};

(2) Surface to volume ratio S/V;

(3) tortuosity α.

The vein size can be calculated from the measured S/V. Due to the existence of particles and ice crystals in the packed beds, we assume a three-grain junction model can describe the vein network well and the vein size can be described as a cylinder (Price, 2000):

$$d_{\mathrm{vein}} = \frac{4}{S/V} \tag{4.15}$$

With known vein size d_{vein} and unfrozen water content ϕ_{w}, the ice crystal size D can be estimated by several models as (Grimm et al., 2008):

$$\begin{aligned} d_2 &= 0.2987 D\sqrt{\phi_{\mathrm{w}}} \\ d_3 &= 0.3874 D\sqrt{\phi_{\mathrm{w}}} \\ d_{\mathrm{m}} &= 0.34 D {\phi_{\mathrm{w}}}^{3/4} \end{aligned} \tag{4.16}$$

where d_2 is the vein size between two parallel ice crystal interfaces, d_3 is the vein size of triple junction interfaces and d_{m} is the geometric mean of the vein sizes from parallel and triple junction models.

This research uses nuclear magnetic resonance (NMR) techniques to complete a laboratory study of unfrozen water content ϕ_{w}, S/V and tortuosity α with model packed beds at variable temperatures, and these data are used to determine the micro-structure of the ice-particle system. The unfrozen water content to be obtained from the amplitude of the NMR signal, which comes only from liquid water protons, S/V the surface-to-volume ratio which can be calculated from the CPMG measurement and the PGSE diffusion coefficient measurement over a short displacement time scale Δ and α the tortuosity for the porous media which can be obtained from the diffusion coefficient measurement over a long displacement time scale Δ. Finally, the ice crystal size D can be calculated with the measurement of the unfrozen water content and S/V at different temperatures.

Besides temperature and particle grain size, unfrozen water content and S/V are also impacted by other variables, such as salt composition. A higher salt concentration will cause a larger melting point depression, which leads to a higher unfrozen water content. In this research, magnesium chloride is used as it causes a significant melting point depression (Gibbard and Gossmann, 1974). 0.4, 9.9, and 102.2 micron PMMA particles were used to study influence of the particle size on unfrozen water content and microstructure.

Ice-Binding Protein

Ice recrystallization leads to the coarsening of ice crystals and results in a structural change of the surroundings of ice crystals, which causes the problems of frost heaving, and impacts cell and frozen food preservation (Zhu et al., 2019). Many micro-organisms that live in cold regions have developed ways to survive in a subzero environment (Ewart et al., 1999). In many cases, the ability to survive is due to the generation of ice-interacting proteins (Brown et al., 2014; Ewart et al., 1999; Wang et al., 2016; Zachariassen and Kristiansen, 2000). Bacterium V3519-10 was been isolated from the Vostok ice core, using ice from a depth of 3519m, and it produces an extracellular ice-binding protein (IBP) (Christner et al., 2001; Raymond et al., 2008). The IBP inhibits the recrystallization process by selectively binding to the prism facet of ice, preventing water molecules from joining along the a-axis (Figure 4.3) (Raymond et al., 2008). In this research, NMR techniques are used to investigate the unfrozen brine vein distribution and structure of ice due to the influence of IBP.

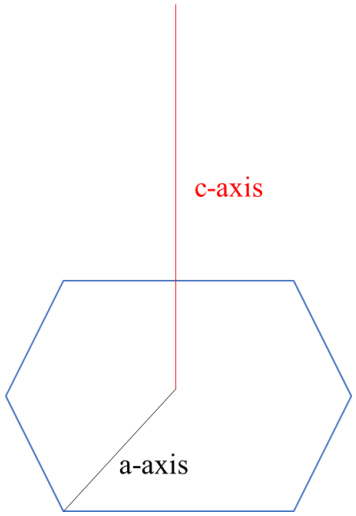

Figure 4.3 The a-axis and c-axis of hexagonal ice.

NMR Techniques to Investigate Porous Media Ice System Structure

Unfrozen water usually exists at the surface of the ice grain and solid particles. Due to the small pore size formed by the ice grain and solid particles, the dominant NMR relaxation mechanism is grain-surface magnetic spin relaxation, where the rate-limiting step is relaxation at the surface rather than the magnetic relaxation that induced by molecular diffusion in susceptibility gradients during conductive transport to the surface (Kleinberg et al., 1994a). Consequently, the surface to volume ratio S/V can be obtained by measuring the NMR relaxation process. Both T_1 relaxation and T_2 relaxation can be used to detect the S/V of the pores composed of the liquid vein network inside brine, ice and ice-particle systems. T_2 relaxation can be detected accurately with the CPMG sequence, which uses the spin echo to eliminate influences from inhomogeneous magnetic fields. Spin-spin magnetic relaxation time T_2 measurement are commonly used to characterize porous media structure (Callaghan, 2011; Song et al., 2008). The grain-surface relaxation $T_{2\mathrm{G}}$ can be expressed as $1/T_{2\mathrm{G}} = \rho\, S/V$ where ρ is the surface relaxivity determined by the material (Kleinberg et al., 1994a). Due to the complex composition of the surface where the relaxation occurs, the surface relaxivity is unknown, and S/V cannot be extracted directly. However, recent research has indicated a direct linear relationship between $1/T_2$ and S/V (Zielinski, 2004). PGSE can measure the mean squared displacement of nuclei resulting from random Brownian motion, and allows determination of the S/V from the short time scale data (Callaghan, 1993; Caprihan and Fukushima, 1990). With the results from the PGSE, T_2 can be scaled to calculate S/V and then used to calculate ice grain size.

The mean-squared displacement of the nuclei in a pore is time-dependent and also influenced by the geometry of the pore (Mitra et al., 1992). Over a short time scale, the diffusion of nuclei undergoes the random Brownian motion except for those molecules near the ice grain and solid particles' surface. Therefore, only the molecules that are a distance less than the diffusion length $\sqrt{D_0\Delta}$ away from the surface during displacement time Δ are affected by the surface and do not undergo random Brownian motion. Due to this, the decrease of the effective diffusion coefficient with increasing displacement time Δ from the self-diffusion coefficient value can be used to calculate the fraction of these molecules that are dependent on the surface area to volume ratio S/V of the pore and diffusion length $\sqrt{D_0\Delta}$. Solution of the Green's function for diffusion indicates S/V and $\sqrt{D_0\Delta}$ have a linear relationship to the effective diffusion coefficient in the short displacement time limit (Mitra et al., 1993). PGSE NMR directly measures the displacement time dependent diffusion coefficients $D(\Delta)$. The relationship between the diffusion coefficient, the surface area to volume ratio and the diffusion length in the short-time regime is described as (Latour et al., 1993; Mitra et al., 1993; Mitra et al., 1992):

$$\frac{D(\Delta\rightarrow 0)}{D_0} = 1 - \frac{4}{9\sqrt{\pi}}\frac{S}{V_\mathrm{p}}\sqrt{D_0\Delta} \tag{4.17}$$

where D_0 is the molecular self-diffusion coefficient, Δ is the displacement observation time.

Over a long timescale, the diffusion of all the molecules is limited by the ice-ice grain and ice-particle grain surface. This means all water molecules in the ice-particle mixture experience restricted motion. In this case, for an isolated pore which is not connected with other pores, the effective diffusion coefficient approaches zero as the mean squared displacement

approaches the squared constant of the pore dimension due to restricted diffusion length in the isolated pore. For interconnected pores, the effective diffusion coefficient directly reflects geometric interconnectivity properties of the ice-brine-particle mixture system (Bear, 1988):

$$\frac{D(\Delta\rightarrow\infty)}{D_0}=\frac{1}{\alpha} \tag{4.18}$$

where α is the tortuosity, the ratio of the path length a molecule travels in the vein to the geometric path (Sen, 2004). The displacement observation time Δ cannot be extended to infinity for NMR measurements due to relaxation time signal decay limiting $\Delta< T_1$ in a stimulated echo experiment. Hence a Pade approximation is used to combine the short and long time scale behavior (Latour et al., 1993):

$$\frac{D(\Delta)}{D_0}=1-\left(1-\frac{1}{\alpha}\right)\left(\frac{\frac{4}{9\sqrt{\pi}}\frac{S}{V_\mathrm{p}}\sqrt{D_0\Delta}+\left(1-\frac{1}{\alpha}\right)\frac{D_0\Delta}{D_0\theta}}{\left(1-\frac{1}{\alpha}\right)+\frac{4}{9\sqrt{\pi}}\frac{S}{V_\mathrm{p}}\sqrt{D_0\Delta}+\left(1-\frac{1}{\alpha}\right)\frac{D_0\Delta}{D_0\theta}}\right. \tag{4.19}$$

where the fitting parameter θ is introduced as the time needed for molecules to diffuse to reach the tortuosity limit. In summary, T_2 relaxometry and PGSE diffusiometry magnetic resonance techniques are used to investigate the ice-particle structure:

Spin-spin magnetic relaxation time (T_2) measurement: (1) the signal extrapolated to zero time is proportional to the unfrozen water content so that it is used to measure unfrozen water content of the ice-particle mixture sample at different temperatures; the CPMG sequence is used to eliminate the undesired influence from the inhomogeneous magnetic field; (2) T_2 is used to detect the surface area to volume ratio of the liquid network at different temperatures since pore

size changes with temperature, which affects the T_2 value by changing the water interaction with the ice and particles.

Diffusion coefficient measurement: Water molecules in the ice-particle mixture are restricted by the solid matrix, which leads to a time-dependent diffusion coefficient. The diffusion coefficient measured by PGSE over different displacement observation time ranges Δ, reflects the geometric properties S/V and α of the ice-particle mixture.

Variables	MR measurement	Equation
water content ϕ_{w}	CPMG - amplitude	$M_{\mathrm{x,y}}(t) = M_{\mathrm{x,y}}(0)\sum_{\mathrm{i}}\exp\left(-\frac{t}{T_{\mathrm{i}}}\right)$
Surface to volume ratio (1/pore length scale) S/V	CPMG - T_2 measurement PGSE - $D(\Delta)$ short times	$T_{2G} = \rho\, {}^{S}/_{V}$ $\frac{D(\Delta\rightarrow 0)}{D_0} = 1 - \frac{4}{9\sqrt{\pi}}\frac{S}{V_{\mathrm{p}}}\sqrt{D_0\Delta}$
Tortuosity α	PGSE - Pade Fitting	$\frac{D(\Delta\rightarrow\infty)}{D_0} = \frac{1}{\alpha}$

Table 4.1: MR measurement with variables.

Table 4.1 summarizes how to use magnetic resonance measurement data is used to obtain the variables that related to the ice porous media structure.

Magnetic resonance techniques have three limitations when studying ice structure. First, the measurements are restricted to the limited size of the sample due to the size of the rf probe used. In this research, 5mm NMR tubes are used to make ice samples which sets a maximum limit for the ice crystals that can be formed. Second, NMR results have shown a systematically

lower water content than thermodynamic models, due to the fastest relaxing water in the smallest pores not being detectable with NMR when T_2 is much less than the CPMG echo time 2τ. Surface relaxation such that $T_2 \ll 2\tau$ causes signal to decay too fast to be detected and in the case of ice includes water molecules exchanging between the liquid water and solid ice phase. Finally, the temperature control of the NMR device is not perfect. The Bruker variable temperature unit controls temperature is with the use of liquid nitrogen flow over a heating element through the inside of the NMR probe from bottom to top. This introduces a temperature gradient from bottom to top for around 1.5℃. The way to reduce the temperature gradient is by decreasing the size of the sample and increasing the amount of nitrogen gas flow to make the temperature more uniform. However, a reduced size of the sample sets a limitation on the maximum size of the ice crystal. Nevertheless, magnetic resonance techniques are unique, valuable and non-destructive tools that can characterize the unfrozen brine vein distribution and structure and investigate the microstructure evolution in ice-related mixtures (Brown et al., 2012; Mitchell et al., 2008; Petrov and Furó, 2009).

References

Andersland, O.B. and Ladanyi, B., 2013. An introduction to frozen ground engineering. Springer Science & Business Media.

Bear, J., 1988. Dynamics of fluids in porous media. Courier Corporation.

Bramson, A.M., Byrne, S., Putzig, N.E., Sutton, S., Plaut, J.J., Brothers, T.C. and Holt, J.W., 2015. Widespread excess ice in Arcadia Planitia, Mars. Geophysical Research Letters, 42(16): 6566-6574.

Brown, J.R., Brox, T.I., Vogt, S.J., Seymour, J.D., Skidmore, M.L. and Codd, S.L., 2012. Magnetic resonance diffusion and relaxation characterization of water in the unfrozen vein network in polycrystalline ice and its response to microbial metabolic products. Journal of Magnetic Resonance, 225: 17-24.

Brown, J.R., Seymour, J.D., Brox, T.I., Skidmore, M.L., Wang, C., Christner, B.C., Luo, B.-H. and Codd, S.L., 2014. Recrystallization inhibition in ice due to ice binding protein activity detected by nuclear magnetic resonance. Biotechnology Reports, 3: 60-64.

Callaghan, P.T., 1993. Principles of nuclear magnetic resonance microscopy. Oxford University Press on Demand.

Callaghan, P.T., 2011. Translational dynamics and magnetic resonance: principles of pulsed gradient spin echo NMR. Oxford University Press.

Caprihan, A. and Fukushima, E., 1990. Flow measurements by NMR. Physics Reports, 198(4): 195-235.

Christner, B.C., Mosley‐Thompson, E., Thompson, L.G. and Reeve, J.N., 2001. Isolation of bacteria and 16S rDNAs from Lake Vostok accretion ice. Environmental Microbiology, 3(9): 570-577.

Dash, J., 1989. Thermomolecular pressure in surface melting: motivation for frost heave. Science, 246(4937): 1591-1593.

De Gennes, P.-G., Brochard-Wyart, F. and Quéré, D., 2004. Capillarity and wetting phenomena: drops, bubbles, pearls, waves, 315. Springer.

Defay, R., Bellemans, A. and Prigogine, I., 1966. Surface tension and adsorption. Wiley.

Ewart, K., Lin, Q. and Hew, C., 1999. Structure, function and evolution of antifreeze proteins. Cellular and Molecular Life Sciences CMLS, 55(2): 271-283.

Gibbard, H.F. and Gossmann, A.F., 1974. Freezing points of electrolyte mixtures. I. Mixtures of sodium chloride and magnesium chloride in water. Journal of Solution Chemistry, 3(5): 385-393.

Gregg, S.J., Sing, K.S.W. and Salzberg, H., 1967. Adsorption surface area and porosity. Journal of The Electrochemical Society, 114(11): 279C-279C.

Grimm, R.E., Stillman, D.E., Dec, S.F. and Bullock, M.A., 2008. Low-frequency electrical properties of polycrystalline saline ice and salt hydrates. The Journal of Physical Chemistry B, 112(48): 15382-15390.

Kleinberg, R., Kenyon, W. and Mitra, P., 1994a. Mechanism of NMR relaxation of fluids in rock. Journal of Magnetic Resonance, Series A, 108(2): 206-214.

Latour, L.L., Mitra, P.P., Kleinberg, R.L. and Sotak, C.H., 1993. Time-Dependent Diffusion Coefficient of Fluids in Porous Media as a Probe of Surface-to-Volume Ratio. Journal of Magnetic Resonance, Series A, 101(3): 342-346.

Mitchell, J., Webber, J.B.W. and Strange, J.H., 2008. Nuclear magnetic resonance cryoporometry. Physics Reports, 461(1): 1-36.

Mitra, P.P., Sen, P.N. and Schwartz, L.M., 1993. Short-time behavior of the diffusion coefficient as a geometrical probe of porous media. Physical review. B, Condensed matter, 47(14): 8565.

Mitra, P.P., Sen, P.N., Schwartz, L.M. and Le Doussal, P., 1992. Diffusion propagator as a probe of the structure of porous media. Physical review letters, 68(24): 3555.

Petrov, O.V. and Furó, I., 2009. NMR cryoporometry: Principles, applications and potential. Progress in Nuclear Magnetic Resonance Spectroscopy, 2(54): 97-122.

Price, P.B., 2000. A habitat for psychrophiles in deep Antarctic ice. Proceedings of the National Academy of Sciences, 97(3): 1247-1251.

Raymond, J.A., Christner, B.C. and Schuster, S.C., 2008. A bacterial ice-binding protein from the Vostok ice core. Extremophiles, 12(5): 713-717.

Rempel, A., 2012. Hydromechanical Processes in Freezing Soils, Vadose Zone J.

Rempel, A., Wettlaufer, J. and Worster, M., 2001. Interfacial premelting and the thermomolecular force: thermodynamic buoyancy. Physical review letters, 87(8): 088501.

Sen, P.N., 2004. Time ‐ dependent diffusion coefficient as a probe of geometry. Concepts in Magnetic Resonance Part A, 23(1): 1-21.

Sizemore, H.G., Zent, A.P. and Rempel, A.W., 2015. Initiation and growth of martian ice lenses. Icarus, 251: 191-210.

Song, Y.-Q., Cho, H., Hopper, T., Pomerantz, A.E. and Sun, P.Z., 2008. Magnetic resonance in porous media: Recent progress. The Journal of Chemical Physics, 128(5): 052212.

Wang, C., Oliver, E.E., Christner, B.C. and Luo, B.-H., 2016. Functional Analysis of a bacterial antifreeze protein indicates a cooperative effect between its two ice-binding domains. Biochemistry, 55(28): 3975-3983.

Zachariassen, K.E. and Kristiansen, E., 2000. Ice nucleation and antinucleation in nature. Cryobiology, 41(4): 257-279.

Zhu, Z., Zhou, Q. and Sun, D.-W., 2019. Measuring and controlling ice crystallization in frozen foods: A review of recent developments. Trends in Food Science & Technology, 90: 13-25.

Zielinski, L.J., 2004. Effect of internal gradients in the nuclear magnetic resonance measurement of the surface-to-volume ratio. The Journal of Chemical Physics, 121(1): 352-361.

CHAPTER FIVE

NMR CHARACTERIZATION OF UNFROZEN BRINE VEIN DISTRIBUTION AND STRUCTURE IN MODEL PACKED BEDS

Contributions of Authors and Co-Authors

Manuscript in Chapter Five

Author: Peng Lei

Contributions: Methodology, Investigation, Formal analysis, Data Curation, Visualization, Writing Original Draft.

Co-Author: Mark W. Young

Contributions: Investigation, Data Curation, Formal analysis Writing - Review & Editing.

Co-Author: Joseph D. Seymour

Contributions: Methodology, Supervision, Project administration, Writing - Review & Editing.

Co-Author: David E. Stillman

Contributions: Methodology, Data Curation, Supervision, Funding acquisition, Writing - Review & Editing.

Co-Author: Katie Primm

Contributions: Data Curation, Writing - Review & Editing.

Co-Author: Hanna G. Sizemore

Contributions: Supervision, Writing - Review & Editing.

Co-Author: Alan W. Rempel

Contributions: Data Curation, Supervision, Writing - Review & Editing.

Co-Author: Sarah L. Codd

Contributions: Methodology, Supervision, Project administration, Funding acquisition, Writing - Review & Editing.

Manuscript Information Page

Peng Lei, Mark W. Young, Joseph D. Seymour, David E. Stillman, Katie Primm, Hanna G. Sizemore, Alan W. Rempel and Sarah L. Codd

Cold Regions Science and Technology

Status of Manuscript:

____ Prepared for submission to a peer-reviewed journal

____ Officially submitted to a peer-review journal

__X_ Accepted by a peer-reviewed journal

____ Published in a peer-reviewed journal

Elsevier, Inc.

NMR CHARACTERIZATION OF UNFROZEN BRINE VEIN DISTRIBUTION AND STRUCTURE IN MODEL PACKED BEDS

Abstract

When a brine mixed with particles is frozen, some liquid water persists due to the freezing point depression caused by the solute impurity, surface energy, and disjoining pressure (wetting forces). This unfrozen water forms a complex "liquid vein network" (LVN). However, details of the freezing process are still not fully understood, including the permeability/tortuosity of the LVN, and the unfrozen water content at a given temperature. Here, we have applied nuclear magnetic resonance (NMR) relaxation, self-diffusion measurements and magnetic resonance imaging (MRI) to investigate the distribution and structure of LVNs. Magnesium chloride ($MgCl_2$) salt concentrations of 15, 30, and 60 mM were investigated with and without poly-methyl methacrylate (PMMA) particles of diameter 0.4, 9.9, and 102.2 μm, allowing us to quantify unfrozen water content and the structure of the LVN as a function of temperature, $MgCl_2$ concentration, and PMMA particle size. The results of magnetic resonance imaging (MRI) and self-diffusion confirm that the inhibition of ice recrystallization is a function of particle size. To gain information on LVN structure, we compared NMR results to Monte Carlo simulations of freezing in brine-particle systems. Comparisons between laboratory and simulation data suggest that, for our experimental range of temperature (-17.4℃ to -0.9℃ ± 0.5℃), solutes make the dominant contribution to the unfrozen liquid fraction for particle sizes larger than a few microns, whereas in the finest grained porous media we tested, the unfrozen liquid fraction is controlled primarily by the films that wet particle-ice interfaces.

Introduction

A water-saturated porous medium that is cooled below its bulk melting temperature can retain some residual liquid that is in equilibrium with ice. This phase behavior finds application in a range of geophysical and industrial settings (Dedovets et al., 2018; Deville, 2017). In pure systems, perhaps the most familiar source of unfrozen liquid stems from the effects of surface energy along curved interfaces, as described by the Gibbs-Thomson equation, which provides a theoretical basis for modeling systems with multiple phases and complex geometries (Kaptay, 2012). More generally, the effects of wetting interactions along particle surfaces (*i.e.* interfacial premelting, which generates thin "quasi-liquid" or "liquid-like" layers) and the melting point depression caused by solutes combine with surface energy to increase the number of parameters that are necessary to describe the relationship between temperature and liquid content (Sizemore et al., 2015). The controls on liquid content are a fundamental constitutive ingredient in predictive models for the behavior of numerous physical systems. Natural examples of phenomena resulting from ice-liquid coexistence in porous media are ubiquitous and include: drainage through brine channels in polycrystalline sea ice, formation and growth of ice lenses in soil causing frost heave (Eide and Martin, 1975; Rempel, 2007; Sizemore et al., 2015; Weeks, 2010; Weeks and Ackley, 1986), and ice-liquid-particle interactions modulating sliding resistance at the beds of terrestrial and interplanetary glaciers (Dash et al., 2006; Deville, 2017). The effects of solid particulates on the phase equilibria of frozen samples also impacts technological development in such fields as ceramics processing, bio-cryopreservation, and food engineering, to name a few (Deville, 2017).

Laboratory studies are needed to expand our understanding of the complex freezing behavior that takes place in porous geophysical and technological systems; this need is particularly acute for planetary applications (Sizemore et al., 2015; Stillman et al., 2014). As solid crystals grow, particles can become partitioned into regions with distinct macro and microstructural porosities and characteristics. In the case of ceramics processing, the properties of porous structures can be controlled by the freezing process (Dedovets et al., 2018; Deville, 2017; Sofie and Dogan, 2001). Recent work by Dedovets et al. (Dedovets et al., 2018) used confocal Raman microscopy to image the particle response to freezing fronts in colloidal emulsions and provided insight into premelting dynamics and solute disbursement and entrapment during freezing (Dedovets et al., 2018). A complementary technique, nuclear magnetic resonance (NMR), can be used to noninvasively provide measurements of critical properties such as liquid solvent content, pore inter-connectivity, tortuosity and pore size (Callaghan, 2011; Mitra et al., 1992; Petrov and Furó, 2009; Song, 2013). In the experimental investigation presented here, we use NMR to probe the freezing behavior of brine-saturated porous media comprised of model spheres.

In the background section, we outline the current state of knowledge concerning LVN in ice and porous media, ice recrystallization at warm temperatures, and the theory of NMR and MRI techniques. The methods section details our sample preparation methods, as well as NMR and MRI procedures. In the experimental data analysis and the results and discussion sections we present our laboratory results, make comparisons to theoretical models, and discuss geophysical and industrial applications.

Background

Ice and LVNs

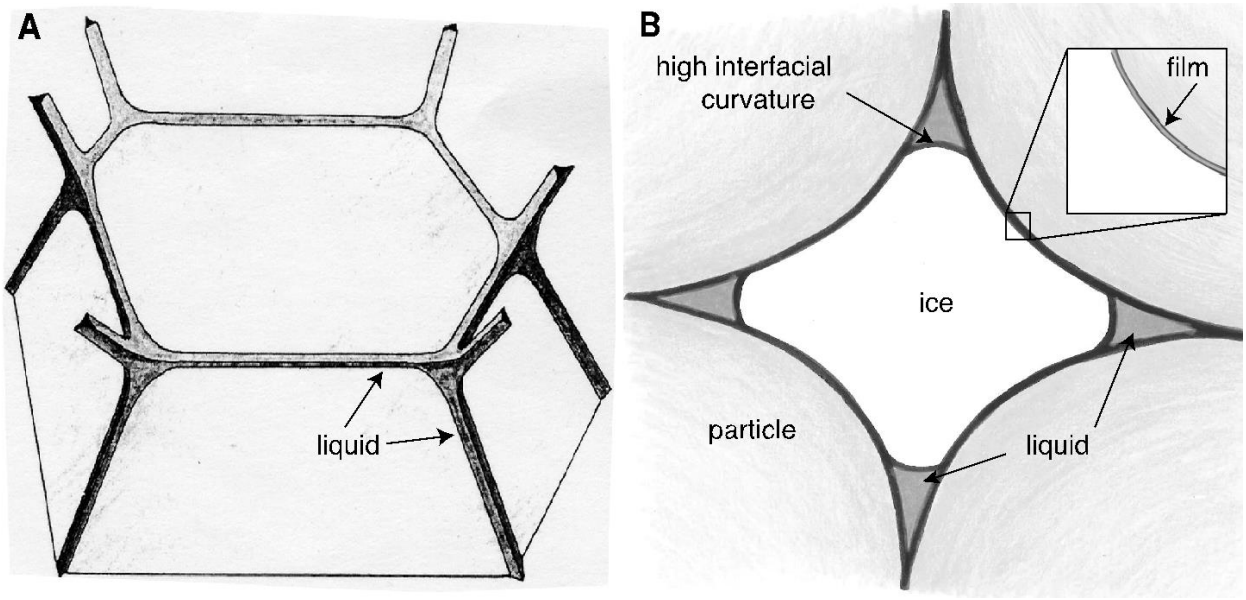

Figure 5.1: Schematics of unfrozen liquid locations at subfreezing temperatures. A) Vein-node network of liquid lining the 3-grain boundaries of polycrystalline ice (modified from (Nye, 1989)). B) Wetting films and high curvature liquid reservoirs near particle contacts in an ice-infiltrated porous medium (modified from (Rempel and Rempel, 2016)). Note that the majority of soluble impurities are concentrated in the unfrozen liquid until the temperature drops below the eutectic temperature.

In polycrystalline ice, liquid water persists due to the presence of impurities such as salt and the high curvatures that characterize the surfaces of veins marking the boundaries where three or more crystals meet (see Fig. 1A). By modeling the vein as an ideal cylinder and ice crystal as truncated semiregular octahedra (Price, 2000), the physical properties of the freezing porous systems can be quantified. At the interface where two parallel octahedra meet, the thickness of the interface can be described as $d_2 = 0.2987D\sqrt{\phi_w}$, where D is the diameter of ice

crystal and ϕ_w is water content in the freezing porous system. At the ice crystal edges where 3 ice crystals meet, the diameter of the cylindrical triple junctions is $d_3 = 0.3874D\sqrt{\phi_w}$, and the geometric mean of these two models gives the diameter of the vein: $d = 0.34D{\phi_w}^{3/4}$ (Grimm et al., 2008).

Further complications are imposed by foreign solid particulates, as wetting interactions cause liquid films to separate ice from particle surfaces and high curvature reservoirs form near constrictions between adjacent particle walls (see Fig. 5.1B). Thus, a general description of equilibrium between ice and liquid must account for: a) the effects of surface energy $\gamma_{il} \approx 0.029\ J/m^2$ (Hardy, 1977) on an interface with curvature κ (sum of the inverse of the two principal radii of curvature); b) the effects of ice–liquid–particle interactions, characterized by a film thickness d dependent disjoining pressure $P_T(d)$; and c) the melting point depression associated with solutes, which is a function $\Gamma(m)$ of the solute concentration m dissolved in the residual liquid, such that $m \approx m_b/S_l$, where m_b is bulk concentration (*i.e.* total quantity of solute divided by pore volume) and S_l is liquid saturation, *i.e.* fraction of the pore space containing liquid. At a local temperature T that is below the bulk melting temperature T_m, these terms can be combined to write (Chen et al., 2020):

$$T_m - T \approx \frac{T_m}{\rho_i L}[\gamma_{il}\kappa + P_T(d)] + \Gamma\left(\frac{m_b}{S_l}\right), \tag{5.1}$$

where ρ_i is the ice density and L is the latent heat of fusion.

In many circumstances, most of the residual liquid in a sub-freezing system can be described with simplified forms of Eq. (5.1) that neglect one or more of the terms on the right

side. In polycrystalline ice, for example, interaction with particles can be excluded so that $P_T(d) \rightarrow 0$, the remaining two terms on the right side of Eq. (5.1) are all that is needed to describe the temperature dependence of changes in vein-wall curvature κ and the function that describes the melting point depression associated with solutes in a liquid network similar to that shown in Fig. 5.1A. As such a system ages, recrystallization takes place with larger ice crystals growing at the expense of smaller ones so that the total interfacial energy of two-grain boundaries is reduced (Bray, 2002; Brox et al., 2015). Progressive crystal enlargement reduces the total length of veins so that vein cross-sectional areas must increase (causing vein curvature and the surface energy term in Eq. (5.1) to decrease) to keep the solute volume fraction from changing dramatically. During isothermal coarsening, since $T_m - T$ is constant, the residual liquid fraction must, in fact, decrease slightly to enable the dominant, final term on the right side of Eq. (5.1) to increase and compensate for the ongoing reduction in the surface energy term as the vein curvature drops.

When foreign solid particles are present, the controls on the residual liquid network can be dramatically more complicated. The wetting films that separate particle and ice surfaces, subsumed in the function $P_T(d)$, tend to be volumetrically more important in systems with smaller particles and correspondingly larger specific surface areas, but high-curvature reservoirs still dominate at warm temperatures near where ice first reaches equilibrium within the confined pore space. With non-zero m_b a transition to solute-dominated liquid contents takes place at sufficiently cold temperatures. In the experimental study described here, we probe the properties of residual water networks and document the physical properties of the freezing porous system as a function of temperature, impurity content, and particle composition.

Nuclear Magnetic Resonance (NMR)

NMR is the energy absorption and emission of nuclei or electrons in a specific magnetic field at a specific frequency. An applied magnetic field generates a net magnetic moment. By measuring the magnetic moment with radio-frequency (RF) excitation and an applied magnetic field gradient, information about magnetic relaxation rates, position and translational motion can be extracted (Callaghan, 2011).

NMR can be used to measure the liquid water content and other structural properties in ice, by modeling it as a porous medium (Brown et al., 2012; Brox et al., 2015). NMR cryoporometry is a well-established technique to determine unfrozen liquid pore volume and surface area in solid porous media (Mitchell et al., 2008; Petrov and Furó, 2009; Strange et al., 1993; Valiullin and Furó, 2002).

Water Content: Since the NMR signal is taken directly from the ^{1}H proton in the liquid phase, the percent of unfrozen water can be directly measured by scaling the signal to the unfrozen sample measurement. This is typically achieved by extrapolating the signal obtained from a Carr-Purcell-Meiboom-Gill (CPMG) multiple spin echo method (Carr and Purcell, 1954; Meiboom and Gill, 1958) back to time zero to obtain a signal amplitude free of NMR relaxation effects.

Relaxation: After excitation of a nonequilibrium magnetization, relaxation is the process of the net magnetic moment returning to its equilibrium state. This occurs through two mechanisms, spin-lattice T_1 relaxation through which the spins return to thermal equilibrium with the surroundings and spin-spin T_2 relaxation, whereby the spins coherent magnetization dephases due to dipolar interactions. In this work, T_2 relaxation of ice and ice-particle systems are measured using a CPMG method. The CPMG pulse sequence allows for the measurement of

T_2 relaxation whilst eliminating the undesired influence from inhomogeneous magnetic fields caused by existence of different magnetic susceptibilities within the sample. T_2 relaxation is described by:

$$M_{x,y}(t) = M_{x,y}(0)\, exp\left(-\frac{t}{T_2}\right), \tag{5.2}$$

where $M_{x,y}(0)$ is the initial coherent magnetization signal just after application of the RF excitation pulse. It is well established that in porous media systems the interactions between the liquid state spins and the pore boundaries increase the relaxation rate over the bulk (Callaghan, 2011). This mechanism is called grain-surface relaxation, and can be described as: $1/T_{2s} = \rho_2\, S/V$ where ρ_2 is the surface relaxivity for T_2 relaxation at the liquid-solid interface and S/V is the surface to volume ratio of the liquid element; it is the liquid-filled portion which we refer to here as the pore. In this case, due to the direct linear relationship between the inverse of T_{2s} value and surface to volume ratio, the change of T_{2s} indicates the change of the pore size. The complex structure of porous media gives rise to multiple mechanisms for spin relaxation. In the small pores, the rate-limiting step is relaxation, which happens at the surface, while in larger pores, the rate-limiting step is the transport process to the surface of the pores (Kleinberg et al., 1994b). For T_2 relaxation the sum of these mechanisms is given by:

$$\frac{1}{T_2} = \frac{1}{T_{2,bulk}} + \rho_2 \frac{S}{V} + \frac{\gamma^2 \langle G_0^2 \rangle D_0 (2\tau)^2}{12}, \tag{5.3}$$

where the first term $\frac{1}{T_{2,bulk}}$ is the bulk fluid relaxation rate and the second term indicates the relaxation rate at the liquid-solid interface (Callaghan, 2011). The last term represents signal

attenuation due to diffusion in the inhomogeneous magnetic fields $\langle G_0^2 \rangle$ generated by interfaces inside the sample. This diffusion attenuation can be controlled by limiting the echo time 2τ for the experiment. For porous systems with small pores, such as those studied here, by minimizing the influence from diffusion and measuring the constant bulk fluid relaxation rate, the S/V can be extracted if the surface relaxivity ρ_2 is known.

Diffusion: Due to the complex composition of the surface where the relaxation occurs, the surface relaxivity in the frozen porous system is unknown and needs to be determined. Methods utilizing pulsed gradient spin echo (PGSE) sequences allows determination of S/V and tortuosity (Callaghan, 2011; Hürlimann et al., 1994; Mitra et al., 1993; Mitra et al., 1992). The use of PGSE NMR allows for the measurement of structure dependent diffusion in porous media. PGSE NMR is based on the use of dephasing and rephasing magnetic field gradient pulses, separated by displacement observation time Δ. By varying the displacement observation time, short and long time diffusion limits can be analyzed, each of which reveal structural information (Sen, 2004).

Over short time scales, the diffusion of nuclei follows random Brownian Motion, with the exception of those molecules nearest the liquid-solid surface. Therefore, the proportion of molecules that will experience surface interactions are those within the diffusion length scale ($\sqrt{D_0\Delta}$)) of the pore wall surface area (S). It follows then that this proportion can be related to the volume of those molecules ($S\sqrt{D_0\Delta}$) divided by the pore volume (V). A formal derivation of this short time limit $\Delta \ll a^2/D_0$ using a Green's function solution of the restricted diffusion is provided by Mitra et al.(Mitra et al., 1993)), and their result is given as:

$$\frac{D_{eff}(\Delta)}{D_0} = 1 - \frac{4\sqrt{D_o \Delta}}{9\sqrt{\pi}} \frac{S}{V}. \tag{5.4}$$

Here D_0 is the constant molecular self-diffusion coefficient and S/V is inversely proportional to pore length a. Equation 5.4 provides a method to measure the pore surface area to volume ratio of samples based on the initial slope of the normalized effective diffusion plotted against the diffusion length scale.

Over long-time scales, the diffusion of all molecules is limited by liquid-solid surfaces. In this regime, the effective diffusion coefficient directly reflects geometric properties of the porous system. This relation is given formally as:

$$\frac{D_{eff}(\infty)}{D_0} = \frac{1}{\alpha} \tag{5.5}$$

where α is the tortuosity, the ratio of the path length a molecule travels in the vein network to the geometric path. The long times needed to asymptotically approach the tortuosity limit are typically outside of those experimentally accessible due to relaxation of the spins in the stimulated echo PGSE experiment (Hürlimann et al., 1994). Thus, an approximation given by the Pade approximant is used to calculate the long-time limit as:

$$\frac{D_{eff}(t)}{D_0} = 1 - \left(1 - \frac{1}{\alpha}\right) \frac{\frac{4}{9\sqrt{\pi}} \frac{S}{V_p} \sqrt{D_0 t} + \left(1 - \frac{1}{\alpha}\right) \frac{t}{\theta}}{\left(1 - \frac{1}{\alpha}\right) + \frac{4}{9\sqrt{\pi}} \frac{S}{V_p} \sqrt{D_0 t} + \left(1 - \frac{1}{\alpha}\right) \frac{t}{\theta}}, \tag{5.6}$$

where θ is a time fitting parameter representative of the time required for a particle to reach the tortuosity limit by diffusion (Callaghan, 2011; Hürlimann et al., 1994).

The T_2 relaxation and PGSE experiments allow use of NMR to monitor changes in liquid water content, pore size, and connectivity of model regolith-ice samples with variation in temperature and salt concentration.

Images: Three dimensional gradients can be used to obtain spatially resolved NMR data and compiled to represent water density in a plane of the sample creating a nuclear Magnetic Resonance Image (MRI). If ice veins are thick enough and sparse enough, they can be visualized. If they are too thin and closer together, they will average on the resolution of the MRI and lead to a background signal across the entire sample plane (image).

Methods

Sample Preparation

Packed bead samples were constructed using polymethyl methacrylate (PMMA) particles of diameter 102.2, 9.9, and 0.4 µm. PMMA was chosen to minimize magnetic susceptibility differences between liquid water and the solid particle phase. Samples of dry 9.9 ± 1.4 and 102.2 (range 90 – 125) µm PMMA particles and a 0.4 µm PMMA particle suspension in water at a concentration of 10% solids (w/w) were obtained from Bangs Laboratories (Fishers, Indiana). Solutions of the dry 9.9 and 102.2 µm particles dispersed in an $MgCl_2$ (Sigma Aldrich) solution of 15, 30, and 60 mM were prepared using demineralized (DI) water. In the case of the 0.4 µm particle sample, $MgCl_2$ was added to the particle containing suspension to obtain 15, 30, and 60 mM solutions. Particle containing solutions were loaded into 5 mm NMR tubes using a pipette. The 102.2 µm particles settled freely under normal gravity, however centrifugation was needed to sediment the 9.9 and 0.4 µm particles. Samples were centrifuged at 800 g's and a temperature

of 4℃ until packed bed height stability was observed. Following centrifugation, the supernatant water was discarded and more particle containing solution was added to the NMR tube before subsequent centrifugation. This process was repeated to build a packed bed of PMMA particles within the NMR tubes with an approximate height of 3.5 cm to fill the RF coil sensitive region while not exceeding the nitrogen gas cooling region. Following the final centrifugation determined by packed bed height stability, the excess supernatant solution was removed, and the samples frozen at −20 ℃.

Particle morphology following centrifugation and freezing was investigated with field emission electron spectroscopy (fig. 5.2). Figure 5.2 shows that following centrifugation the PMMA particles retained their spherical shape, did not show aggregation, and the particles' monodisperse size distribution is evident. The void fraction of each sample particle pack was determined after extended drying of the samples. Samples were dried under a vacuum of 0.2 bar and 165°F over the course of 10 days. Sample mass was monitored daily, and when the mass remained constant for a week, it was assumed that all water had left the system. Values for void fraction were then calculated based on the initial and final mass of the system converted to sample volume.

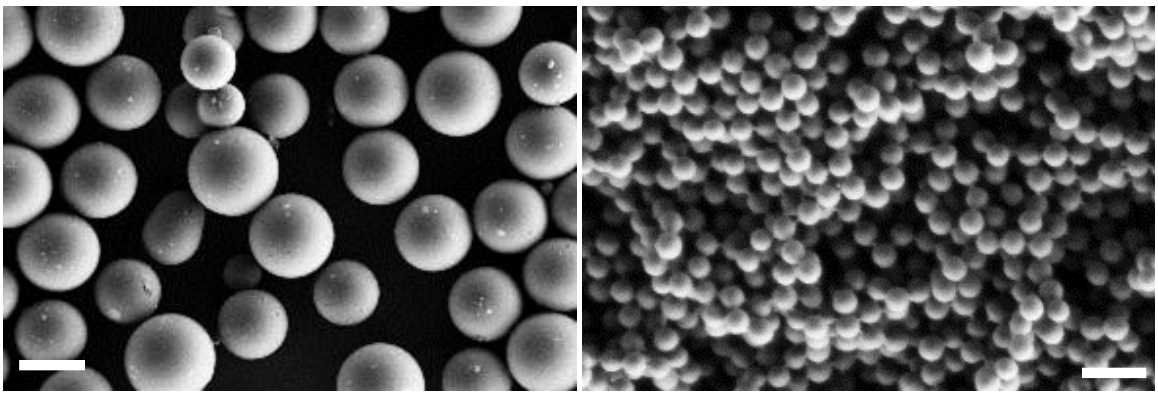

Figure 5.2: SEM images of dried (A) 102.2 µm and (B) 0.4 µm PMMA particles following centrifugation and freezing. Scale bars are (A) 100 µm and (B) 1 µm.

NMR Experiments

NMR experiments were conducted on an Avance III Bruker 250 MHZ spectrometer using a purpose-built NMR probe capable of ~1 µs excitation pulses at 100 W with a 5 mm RF coil for CPMG measurements and with a standard Micro5 NMR probe capable of ~10 µs excitation pulses at 50 W with a 8 mm RF coil for CPMG and PGSE measurements. The purpose-built probe allows measurement of short T_2's on the order of ~10 µs and higher. Temperature inside the spectrometer was controlled using the Bruker VTU temperature control unit.

CPMG Experiments: T_2 relaxation and water content was measured with a CPMG spin echo train using the two different NMR probes with: 90º RF pulse time of 3.4-4.0 µs or 6.0-8.0 µs depending on the sample, temperature and probe, constant RF pulse power of 100 W or 50W depending on the probe, echo times (2τ) of 24 µs for the 0.4 µm samples, and 400 µs for the 102.2 µm, 9.9 µm and no particle samples. The total number of echoes acquired were 200 for 0.4

μm samples and 1600 for 102.2 μm, 9.9 μm and ice only samples in order to measure longer T_2's of the order of 100's ms in the larger particle samples. The temperature range for the CPMG experiments varied from $-17.4℃$ to 3.6℃. Unfrozen water content was obtained through the analysis of the initial amplitude of the echo decay signal. Distributions of T_2 relaxation times were obtained through a 1D Laplace inverse analysis of the CPMG data that was performed in MATLAB (Callaghan, 2011).

PGSE Experiments: Of the systems studied here, brine and samples containing 102.2 μm and 9.9 μm particles were accessible with this measurement. The small pore size of the samples made from 0.4 μm particles and associated short relaxation times prohibited analysis in those samples. A pulsed gradient stimulated echo sequence was used to measure diffusion with a Bruker Diff30 gradient coil providing 17.8 T/m at 60 A. PGSE NMR was performed using a gradient duration time (δ) of 2 ms, an echo time (2τ) of 8.36 ms, and displacement observation times (Δ) that ranged from 10 to 1000 ms. The gradient amplitude was incremented in 4 steps from a minimum gradient of 0.0649 T/m to a maximum gradient value ranging from 2.50 to 0.25 T/m depending on the sample and diffusion observation time used. Only 4 steps were used here to reduce the experiment time and minimize the impact of ice recrystallization during the experiment process at $-7.7℃$.

NMR Imaging Experiments: To visualize the ice recrystallization process, a standard multi-spin-multi-echo sequence was used with a Micro5 gradient coil providing 3 T/m gradients at 60 A in all 3 coordinate directions to generate axial transverse cross-section images with a spatial resolution of 43 × 43 μm (128 × 128 matrix size and 5.5 × 5.5 mm field of view) over three 0.5 mm thick slices located around the center of the RF coil; and sagittal longitudinal axis

images with a spatial resolution of 43 × 43 μm (256 × 128 matrix size and 11 × 5.5mm field of view) over a 0.5 mm thick slice located in the center of the RF coil. The MRI scan was acquired after two hours freezing at $-17.4℃$ in the spectrometer and then 30 mins post temperature change to reach thermal equilibrium for the device at $-7.7℃$.

Experimental Protocols

Protocol 1: Unfrozen water content & T_2 vs. temperature

The samples were thawed then frozen overnight at $-20℃$ in the freezer before measurement. The CPMG data was acquired at 17 specific temperatures between $-17.4℃$ and $3.6℃$ over three days. During the night, the samples were stored in the freezer at $-20℃$. Temperature increases were equilibrated for 10-30 minutes based on CPMG tests performed in duplicate to test for thermal equilibrium.

Protocol 2: Ice recrystallization

The ice recrystallization process was monitored over a three day period. For the first day, the samples were frozen in the freezer at $-20 \pm 2℃$ for two hours, then CPMG data was acquired at $-17.4℃$, $-13.9℃$, $-10.3℃$ and $-7.7℃$ from low to high temperature. Temperature increases were equilibrated for 10-30 minutes and CPMG tests were repeated twice to test for thermal equilibrium. For the second day the temperature was held at $-7.7℃$ whilst CPMG and PGSE data were acquired in turn periodically until the morning of third day. After that, the temperature was set back to $-17.4℃$ and the CPMG data was acquired again at the same 4 temperatures from $-17.4℃$ to $-7.7℃$ and PGSE data was acquired at $-7.7℃$.

Protocol 3: CPMG with different τ, calculate ρ

The CPMG and PGSE data were acquired in turn at the temperature of $-17.4℃$ and $-7.7℃$ to compare with each other and calculate the surface relaxivity ρ_2. Then the ρ_2 was used to scale the relaxation behavior of the CPMG data acquired previously. Additionally, to investigate the influence of diffusion on T_2 values, two sets of CPMG data were also acquired with a range of echo times from 40 to 480 μs for 102.2 μm and ice only samples with 60 mM $MgCl_2$ to track the influence of echo time on the T_2 distribution. During the measurement, the sample temperature was set to $-15.3℃$, $-4.4℃$ and to a fully melted condition of $3.6℃$.

Numerical simulations of water content

We followed the methodology described by Chen and Rempel (2020) to approximate the ice—liquid interface geometry and solute content and evaluate Eq. (5.1) at a sequence of randomly chosen points, enabling us to use Monte Carlo integration to predict changes in liquid saturation with temperature. This involved first constructing a close-packed monodispersed particle pack (50,000 particles, constrained to fill a box with a square horizontal cross-section 100 particle radii on a side) using codes downloaded from Chen and Rempel (2019b). Next, we sampled this synthetic porous medium at 10,000 points in a cross-section located 14 particle radii above its base (tests confirmed that negligible differences were obtained with results from a cross-section sampled at 21 particle radii above the base). We used the codes downloaded from Chen and Rempel (2019a) to perform this sampling and evaluate Eq. (5.1) to identify the coldest temperature at which liquid remains in equilibrium with ice at each distinct point, enabling us to determine the liquid saturation as a function of temperature. The 102.2 and 9.9 μm diameter experimental bead packs had void fractions consistent with close-packing (43 ± 2% and 45 ± 5%,

respectively), which are well-approximated by the sampled void fraction of the synthetic porous medium (42%). The 0.4 μm diameter bead pack was much less dense (61 ± 2% void fraction), however, so for comparison against that case the synthetic porous medium was adjusted by scaling all particle coordinates by a uniform factor of $\alpha = [(1-\phi_{close})/(1-\phi_{loose})]^{1/3} \approx 1.14$ (while leaving particle radii unchanged), to arrive at a sampled void fraction of approximately 64%.

The descriptions of the effects of surface energy and solute in Eq. (5.1) are well-constrained and have no adjustable parameters. The surface physical chemistry that controls wetting behavior is more uncertain. A rich variety of intermolecular forces can contribute towards the dependence of disjoining pressure on film thickness $P_T(d)$. Here, we used a power-law, such as expected to result from non-retarded van der Waals interactions (with exponent $\beta = 3$) and often used to approximate other microphysical processes (e.g. Langmuir-type electrostatic interactions with exponent $\beta = 2$), so that:

$$P_T(d) \approx P_0 \left(\frac{\lambda_0}{d}\right)^{\beta} \tag{5.7}$$

where λ_0 is the film thickness that produces $P_T = P_0$ along a flat surface (i.e. $\kappa = 0$) with no solutes (i.e. $m_b = 0$). Recognizing that $\rho_i L/T_m \approx 1.1\ MPa/K$, adopting $P_0 = 10^5 Pa$ and substituting into (1) makes $d = \lambda_0$ when $T \approx -0.1$℃. This allowed us to perform simulations of liquid content in synthetic porous media while describing the film contribution using two parameters: we treated λ_0 as an adjustable parameter, and held $\beta = 3$.

Experimental Data Analysis

Experimental Water Content

Unfrozen water content of each sample was determined by extrapolating a value of $M_{xy}(0)$ from each CPMG experiment and then normalizing the value of $M_{xy}(0)$ at each temperature to the value when all water in the sample is liquid. To determine values of $M_{xy}(0)$, regression analysis was used to regress a 2nd order polynomial to the initial CPMG T_2 decay; this was to ensure appropriate fitting of the function to the data, and $R^2 > 0.98$ was observed for all regressions.

T_2 Distributions

T_2 relaxation time distributions for the CPMG echo decays were obtained using a 1D Laplace Inverse analysis of the signal decay in MATLAB (Venkataramanan et al., 2002).

Diffusion Coefficients

Diffusion coefficients $D(\triangle)$ were obtained from the PGSE experimental data using Stejskal-Tanner plots for each observation time $\triangle$ (Stejskal and Tanner, 1965) for 102.2 and 9.9 μm beads. From the plots of $D(\triangle)$ the free diffusion coefficient D_0 was then extrapolated from the effective diffusion coefficient at short observation times and the surface area to volume (S/V) ratio was then determined using equation 5.4 in the short observation time limit with a regression analysis which performs a linear fitting between diffusion coefficients and diffusion lengths to obtain the slope with 95% confidence level in Excel. The non-dimensional diffusion coefficient $D(\triangle)/D_0$ was then fit with the Pade approximation in order to obtain values for the tortuosity.

Calculation of S/V from CPMG data

In the 102.2 μm samples, the S/V obtained from PGSE experiments was used to calculate the surface relaxivity (ρ_2) using equation 5.3. The 102.2 μm sample was chosen as it was possible to run these CPMG experiments with different τ times and therefore account for the diffusion mechanism in the third term when fitting equation 5.3 to obtain the surface relaxivity.

This surface relaxivity determined from PGSE experiments in the 102.2 μm samples were then used to scale the T_2 data to obtain the S/V in the 0.4 and 9.9 μm samples. Inherent in this approach is the assumption that the surface relaxivity is constant between samples with 102.2 μm particles and those with 0.4 and 9.9 μm particles, and the use of identical solid particles in each sample composition supports this assumption. It is important to note that the exact mechanism of surface relaxation at the solid ice – liquid water interface is not established. Additional details on the implementation of the determination of S/V in all the samples can be found in the results and discussion section.

Monitoring the ice recrystallization process

To track the ice recrystallization process in the early stage, all the samples were thawed and then frozen in a freezer at $-20 \pm 2℃$ for two hours before measurement. CPMG data was acquired as the sample temperature increased from $-17.4℃$ to $-7.7℃$ at 4 different evenly distributed temperatures throughout the range. Then the CPMG and PGSE data were acquired at around 6.5, 25, 36 and 48 hrs. The temperature was then set back to $-17.4℃$ and CPMG measurements from $-17.4℃$ to $-7.7℃$ were repeated.

Results and Discussion

Void Fraction: The void fraction of the particle porous media systems was determined by weighing saturated packs before and after drying the samples under a vacuum of 0.2 to 0.4 bar and a temperature of 165 °F. Calculated sample void fractions were 0.61 ± 0.02, 0.45 ± 0.05 and 0.43 ± 0.02 for the 0.4, 9.9 and 102.2 μm particles, respectively. Specific surface areas were calculated using the mean diameter of the PMMA particles in each sample, yielding values of 12.7, 0.51 and 0.05 m^2g^{-1} for the 0.4, 9.9 and 102.2 μm particles, respectively.

Water Content: Liquid water content versus temperature results are shown in Figure 5.3. The water content of all ice samples increased with temperature and higher salt concentration. Most significantly, water content for the 0.4 μm PMMA-ice sample was much higher than that in the 9.9 and 102.2 μm PMMA-ice samples at the same brine concentration, and the ice samples without particles had the lowest water content. These expected results are explained easily by equation 5.1, which indicates a higher interfacial curvature will lead to a higher melting point depression due to higher surface energy. The higher curvature of voids between 0.4 μm particles compared with 9.9 and 102.2 μm particles introduces more surface area and also increases the volume of surface liquid films, producing higher water contents.

At lower temperatures, no significant difference in percentage of liquid water between samples containing no particles and 9.9 or 102.2 μm PMMA particles was observed. The changes in $MgCl_2$ molarity play a more significant role compared with surface curvature effects present between the particles and the ice grains in the pore space in the measured temperature range. A notable difference occurs when 0.4 μm PMMA particles are used to form the sample packed bed matrix. Liquid water percent values at −15.4℃ were 0.16 ± 0.02, 0.16 ± 0.02, and

0.17 ± 0.02 for 15 mM, 30 mM, and 60 mM for the 0.4 μm samples, respectively. The lack of variation indicates the solute concentration effects on the melting point depression are negligible compared to the large vein-wall curvature κ. In Figure 5.3B, the percentage of liquid water in brine samples are shown to be lower but have a reasonable correlation with simulations of freezing in brine systems (Grimm et al., 2008). Previous NMR results have shown a systematically lower water content than thermodynamic models with the difference between NMR data and models decreasing with increasing τ, due to the small volumes at liquid water present at colder temperature and lower solute concentrations (Brown et al., 2012). It is important to note that the amount of water in the frozen sample for 15mM $MgCl_2$ sample containing no particles at $-17.4℃$, is around 0.45 μL. In such small volumes errors associated with the regression to zero echo time as a percentage of total water are significant. In order to avoid too much RF power deposition, which can melt the sample, the time of CPMG was fixed at 400 μs. Liquid water in the smallest pores with high enhanced surface relaxation such that $T_2 < 400$ μs are not detected and regression to $M_{xy}(0)$ is systematically lower than predictions of the thermodynamic model.

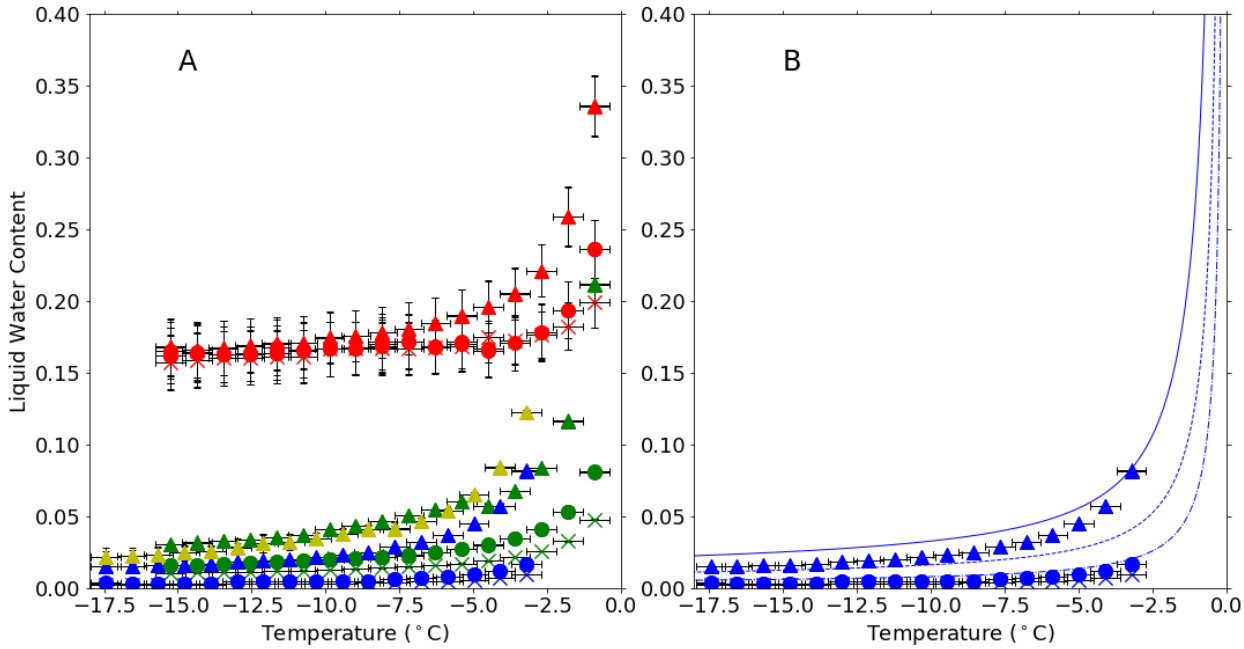

Figure 5.3: Liquid water content as a function of temperature. (A) Samples containing no particles (Blue), 102.2 μm PMMA (Green), 9.9 μm PMMA(Yellow) and 0.4 μm PMMA (Red) with $MgCl_2$ concentration of 15 mM (X), 30 mM (●) and 60 mM (▲). (B) Samples containing no particles (Blue) with $MgCl_2$ concentration of 15 mM (X), 30 mM (●) and 60 mM (▲) and simulated data with $MgCl_2$ concentration of 15 mM (— ▪ — ▪ —), 30 mM (- - -) and 60 mM (——).

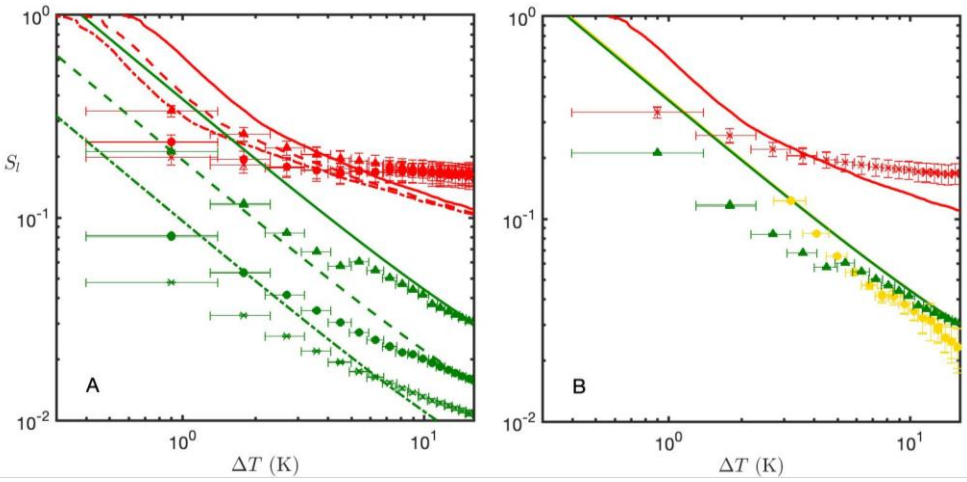

Figure 5.4: Measured liquid water content S_l (symbols) compared with numerical predictions (lines) following Eq. (5.1), shown as a function of $\Delta T = T_m - T$ using a log scale. In all cases, films are described by equation (5.7) using $\beta = 3$, P_0 = 1.1 MPa, and λ_0 = 30 nm. A) Variations in experimental data and model predictions with $MgCl_2$ concentration of 15 mM (X), 30 mM (●) and 60 mM (▲) for the 0.4 (red) and 102.2 μm (green) particles; dot-dashed lines and crosses are at $MgCl_2$ concentration $m_b = 15$ mM, with dashed lines and circles 30 mM, and solid lines and triangles 60 mM. B) Results at a uniform $MgCl_2$ concentration of $m_b = 60$ mM in bead packs made from particles with diameters of 0.4 μm (red), 9.9 μm (yellow) and 102.2 μm (green).

Figure 5.4 compares the results of the simulations discussed above (lines) with the experimental data (symbols), plotted as a function of $\Delta T = T_m - T$ using logarithmic axes. In Figure 4A, green lines and symbols show the liquid water content in the void space between 102.2 μm diameter particles, displaying regular offsets between the three different m_b cases and the same power-law slope of -1, which characterizes the colligative effects of solutes. The data have an offset from model predictions, as seen in Figure 3B, but show similar scaling trends. In contrast, the red lines and symbols depict water content hosted in the void space between 0.4 μm particles, exhibit larger sensitivity to solute concentration at smaller values of ΔT, whereas the

experimentally determined water contents are nearly independent of $MgCl_2$ concentration at the coldest temperatures. The modeled water contents (lines) share these general features, showing reasonable agreement with the data when the liquid films are treated using Equation (5.7), with the λ_0 parameter set to produce films of 30 nm thickness against a flat substrate at -1℃. However, the power-law description of film thickness chosen to produce the model results predicts an ongoing gradual decrease in water content with increased ΔT even after the three different line types (i.e. representing the three different values of m_b) converge. The experimental data appears to reach a nearly constant plateau at the coldest temperature, which is suggestive of a limiting "irreducible" liquid content that has an even lower sensitivity to further cooling than achieved with the $\beta = 3$ exponent used in Equation (5.7).

Figure 5.4B compares the simulation results (lines) to data (symbols) for three different particle sizes, at a bulk $MgCl_2$ concentration of m_b = 60 mM. Of note here are the nearly identical predictions for the 102.2 and 9.9 μm cases, which are dominated by solute effects. In contrast, the higher interfacial curvatures and total surface areas within the 0.4 μm particle pack lead to substantially higher predicted and observed water contents over the entire range of ΔT.

T_2 Distributions: Figure 5.5 shows T_2 distributions for the frozen porous samples at different temperatures (−17.4℃ to −0.90 ℃). It is evident that as temperature increases, the T_2 distributions shift to longer periods and increase in amplitude. Larger overall areas under the distribution curves indicate water content increases with temperature as expected. The shift of the distributions to longer periods indicates an increase in the S/V. Figure 5.5D shows the different dominant T_2 peak values for all the samples. In general, the samples with higher salt concentration have higher T_2 values indicating the influence of increasing salt composition is to

increase vein size and decrease S/V. However, there is one anomaly in that the 102.2 μm and samples containing no particles for the 15 mM concentration indicate larger vein size than the same samples with 30 mM concentration at higher temperatures. This anomaly may be due to the competing effect of recrystallization, which also impacts ice vein size, and is inhibited by higher salt concentrations. The influence of solid PMMA particle size on liquid water S/V is also evident with decreasing particle sizes leading to decreasing T_2 times. In Figure 5.5C the maximum amplitude of each temperature's T_2 distribution in the 0.4 μm sample remains relatively constant until a temperature of around -3℃. This suggests that the amount of liquid water contributing to the T_2 signal remains relatively constant throughout the warming from -15℃ to -3℃. Additionally, the corresponding T_2 relaxation time of the distribution's maximum amplitude in the 0.4 μm particle sample remained relatively constant throughout the temperature ranges explored (Fig 5.5D). This appears to suggest that the S/V of the pores in which liquid resides in the 0.4 μm particle sample remains constant over the investigated temperature range. Due to uncertainty surrounding the calculation of the surface relaxivity of the particle system, the exact S/V ratio values of the liquid water pores or veins requires some approximations to be made as discussed below.

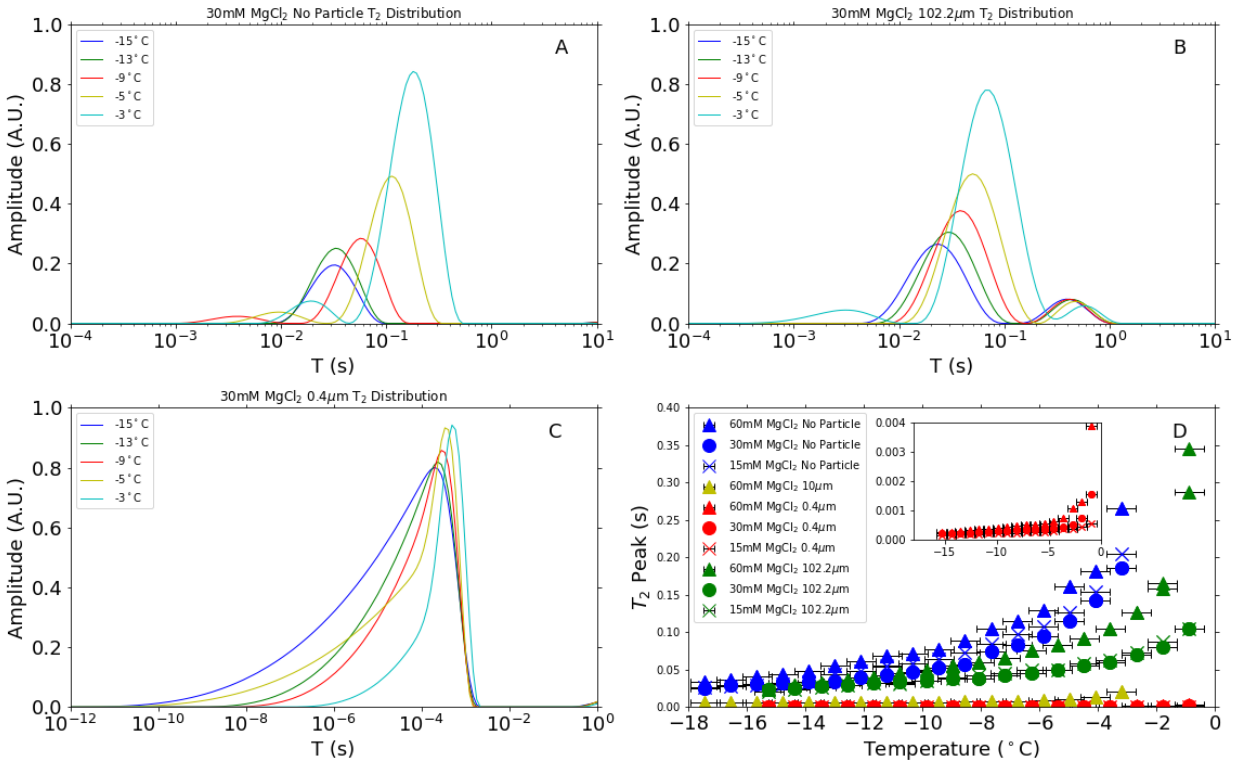

Figure 5.5: Representative T_2 relaxation time distributions as a function of changing temperature for, (A) 30 mM no particle (B) 30 mM 102.2 µm PMMA particles, and (C) 30 mM for the 0.4 µm PMMA particles at a temperature of −15℃ (Blue), −13℃ (Green), −9℃ (Red), −5℃ (Yellow) and −3℃ (Cyan). (D) Changes in the T_2 relaxation time corresponding to the maximum signal at each temperature plotted for all samples. The samples in (D) are: no particles (Blue), 102.2 µm PMMA particles (Green), 9.9 µm PMMA (Yellow) and 0.4 µm PMMA particles (Red) in $MgCl_2$ concentrations of 15 mM (X), 30 mM (●), and 60 mM (▲). Note the no particle and 102.2 µm data for 15 mM are higher than the 30 mM, however they should be lower, an effect attributable to greater ice grain growth as discussed in the text

Correcting τ in CPMG: In Equation 5.3, the diffusion term can be minimized by choosing a short τ time. Figure 5.6 shows the influence of τ variation on the dominant T_2 peak value from 40 µs to 480 µs. $1/T_2$ increases with increasing τ time as the influence of local inhomogeneous fields during the diffusion process is enhanced. As the temperature increases, the liquid water pore size increases. In the fully melted 3.6 ℃ sample, the dominant mechanism

becomes bulk relaxation even in the 102.2 μm sample due to its large pore size and low magnetic susceptibility effect, and τ no longer has a significant influence on the T_2 time. It may appear that a shorter τ would be best, however, too many echoes add enough RF energy to the sample to melt it during the CPMG acquisition. Thus, during the measurement, the τ time was fixed at 400 μs for the samples containing no particles and samples containing 102.2 μm and 9.9 μm particles, and fixed at 12 μs for the 0.4 μm particle sample in order to acquire the short T_2 signal of that sample. To account for the influence from diffusion, the difference between τ values of 40 and 400 μs for one sample at different temperatures was calculated and assumed to be a constant. Accounting for the influence from the diffusion during the longer τ time it is possible to neglect the third term in equation 5.3.

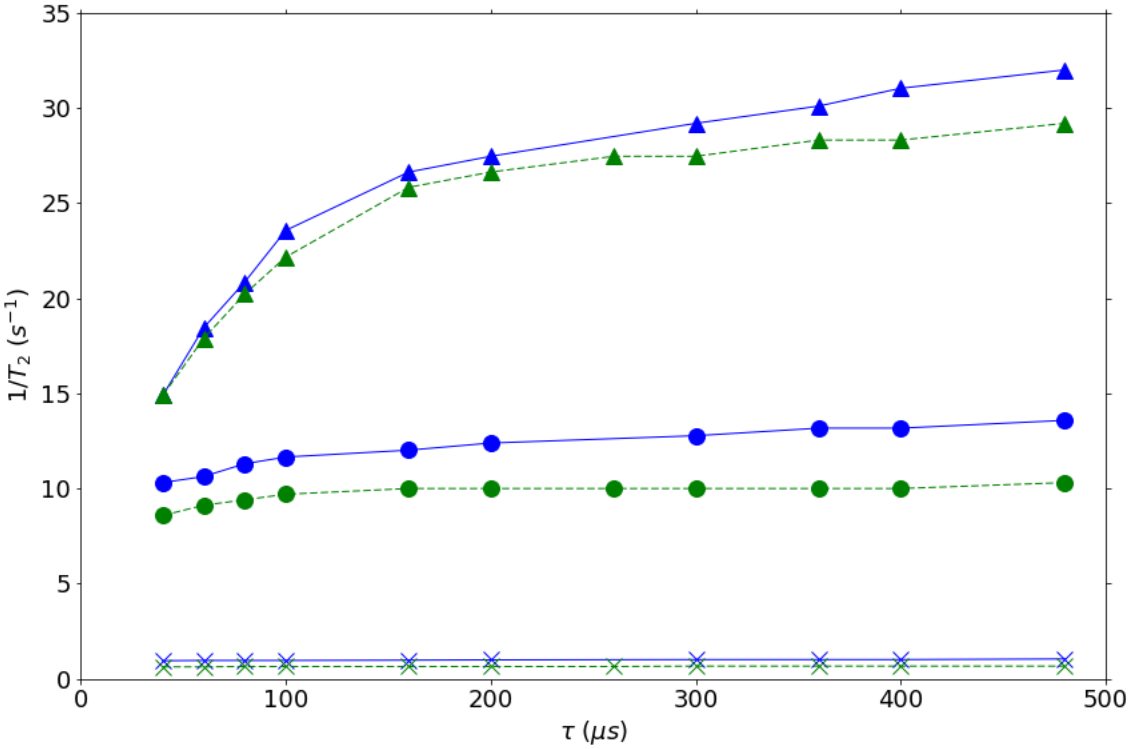

Figure 5.6: $1/T_2$ as a function of τ and temperature. Samples containing 102.2 µm PMMA 60 mM (blue solid line) and no particle 60 mM (green dash line) with temperature −15.3℃ (▲), −4.4℃ (●) and 3.6℃ (X).

Relaxivity Estimation: S/V can be calculated from CPMG data using equation 5.3, and from a Pade approximation fits to PGSE data. By equating the S/V as measured from the two methods, an estimation of relaxivity was obtained for the 102.2 µm sample at 60 mM. By then assuming the surface relaxivity is the same in the 102.2, 9.9 and 0.4 µm particle samples at all other salt concentrations, the S/V of all other samples could also be estimated. The surface relaxivity was estimated as: $\rho_{102\mu m@60mM}$ = 12.60 µm/s. The surface relaxivity for the no particle samples was estimated as $\rho_{\text{no particles @60mM}}$ = 18.62 µm/s. Both values of relaxivity are well within the expected parameter space for relaxivity (Kleinberg et al., 1994b). The higher surface

relaxivity of the no particle sample reflects the greater surface interaction of the liquid state protons with the ice surface than the polymer surface.

Vein Size estimation: Using the estimation of surface relaxivity calculated from the comparison of the S/V from the CPMG and PGSE experiments, and accounting for the influence from the diffusion term as described previously, T_2 can be converted into S/V distributions using equation 5.3. The bulk relaxation rate was determined to be 0.985 s as measured for the melted pure 60 mM $MgCl_2$ sample at 3.6℃. With resulting estimates of S/V, the vein size was then calculated using several models. Since the frozen porous sample contains many particles and ice grains, the network of veins was assumed to be well described by the three-grain junction model, which fits the cylinder model and the size of the vein can be defined as: $d_{vein} = \frac{4}{S/V}$ (Price, 2000). The results are shown in Figure 5.7B.

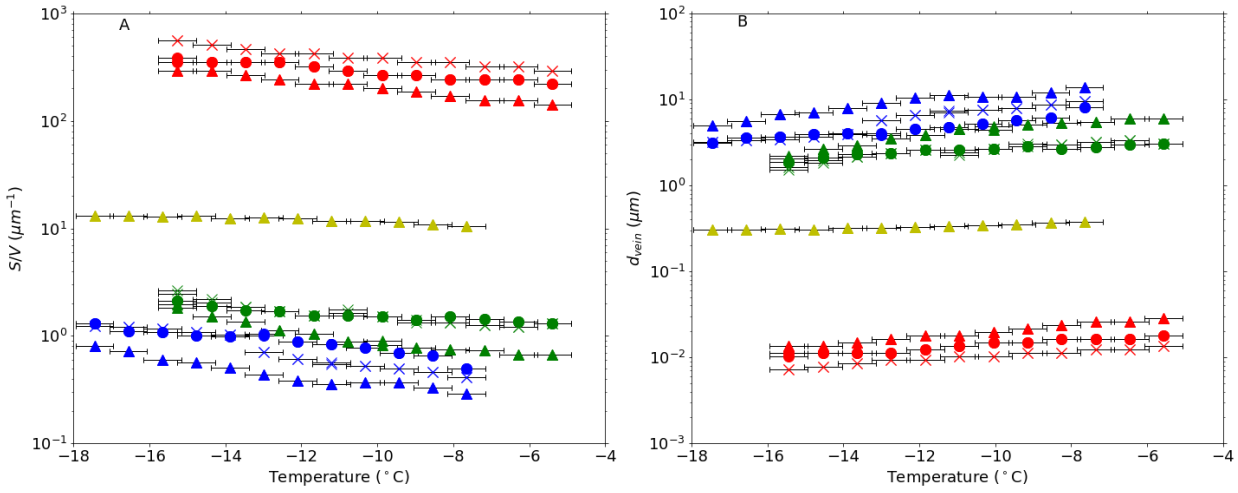

Figure 5.7: (A) S/V calculated from CPMG as a function of temperature. (B) Size of the vein calculated from S/V. Samples containing no particles (blue), 102.2 µm PMMA (green), 9.9 µm PMMA(yellow) and 0.4 µm PMMA (red) with $MgCl_2$ concentration of 15 mM (X), 30 mM (●) and 60 mM (▲).

Ice Grain Size Estimation for no particle sample: For the ice samples with no particles, ice grain size can also be estimated with the relationship $d_m = 0.34\delta\omega^{3/4}$ where d_m is the mean diameter of the veins, δ is the ice grain size, ω is the water content (Grimm et al., 2008; Price, 2000). In order to fit this relationship for vein size to the experimental data, the recrystallization going on as time progresses was allowed as a fitting parameter, as the experimental data was acquired over several days. The fit in Figure 5.8 was accomplished by letting the ice grain size δ increase 60 μm for the 15 mM, 40 μm for 30 mM sample; and 20 μm for 60mM sample for every hour of the measurement, indicating the ice grain growth is inhibited by the higher salt concentrations. The fit to the experimental data is shown in Figure 5.8 as solid lines. Over the duration of the experimental run for each sample (20 hours) this fit indicates samples containing no particles and 15 mM $MgCl_2$ have an ice grain size that grows from 900 to 1560 μm, whereas the ice grain size grows from 550 to 990 μm for the sample with 30 mM $MgCl_2$ and 350 to 570 μm for the sample with 60 mM $MgCl_2$. This result supports the fact that the T_2 peak value of no particle and 102.2 μm for 30 mM became lower than the 15 mM during the measurement, as the ice grains grow slower at the higher salt concentrations, and larger ice grains result in larger veins and commensurate T_2(Brown et al., 2012).

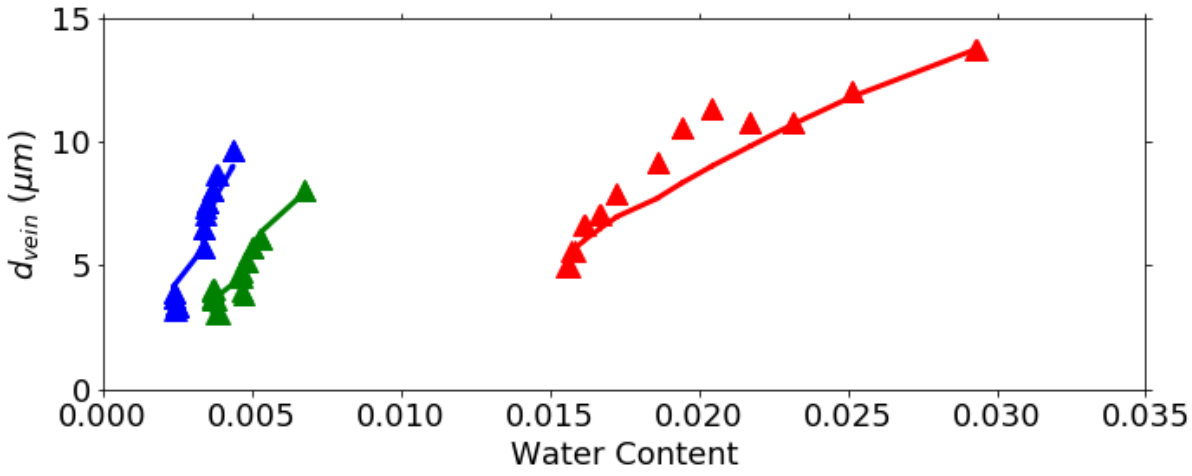

Figure 5.8: Fitting of vein diameter and water content (solid line) allowing for growth of the ice grain size as a function of experimental time due to ice recrystallization. Samples containing no particles with $MgCl_2$ concentration of 15 mM (blue), 30 mM (green) and 60 mM (red).

Monitoring Ice Recrystallization: PGSE measurements were carried out on the 60 mM $MgCl_2$ samples containing 102.2 µm particles, 9.9 µm particles, and no particles. The measurements were made according to protocol 2 described previously. As shown in Figure 5.9A, the dominant T_2 peak value measured as a function of temperature during day 1 is lower than that measured at day 3 due to crystal growth processes occurring during day 2 for the no particle sample. For the sample containing 102.2 µm particle, the growth of the ice crystals was inhibited by the surrounding particles, however, due to the large size of the particles, the ice crystals can still grow inside the vein formed by 102.2 µm particles as evidenced by the small variation in the data (Figure 5.9B). For the sample containing 9.9 µm particles, the growth of the ice crystals was totally inhibited by the small surrounding particles and the T_2 peak didn't change during the 3 day period (Figure 5.9C).

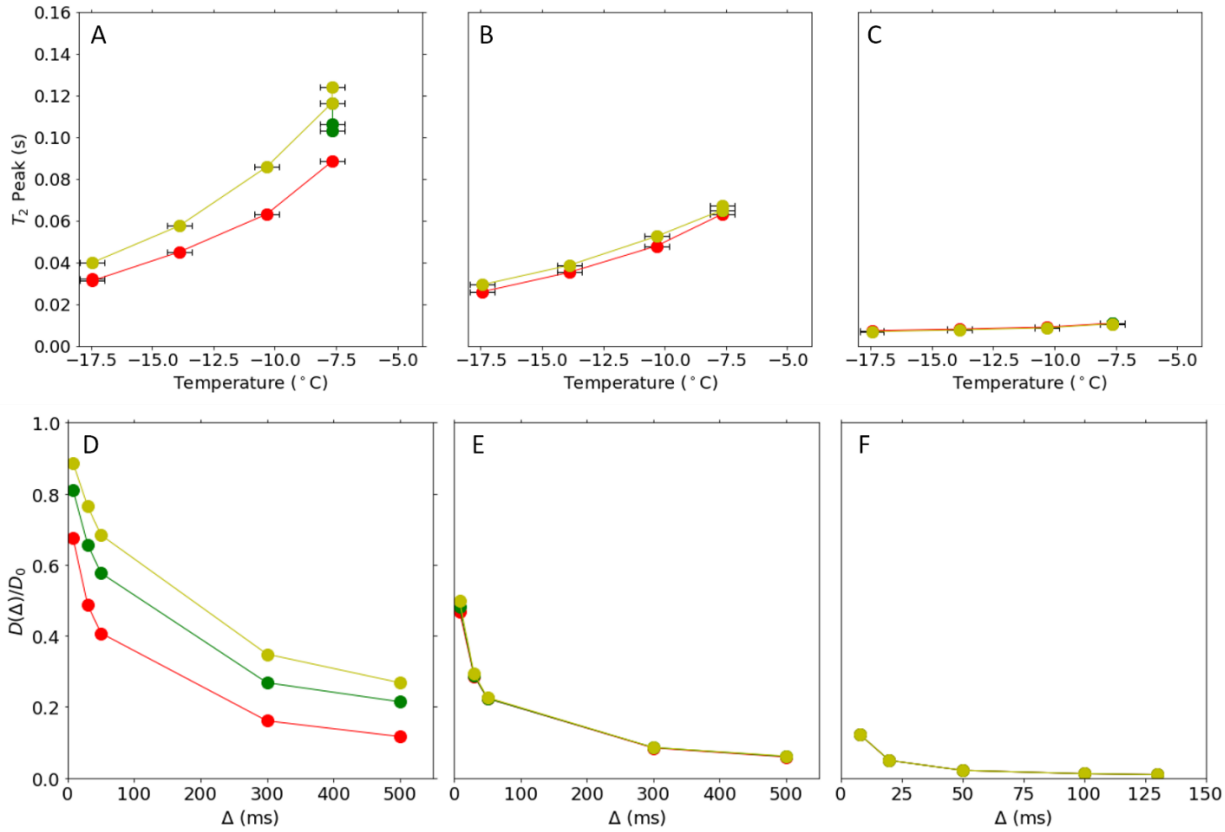

Figure 5.9: T_2 peak value at four different temperatures ramped from low to high in day 1 (Red) and day 3 (Yellow); fixed temperature in day 2 (Green) for (A) no particles, (B) 102.2 µm PMMA, (C) 9.9 µm PMMA with 60 mM $MgCl_2$ concentration. Normalized diffusion coefficient versus Δ at different total experiment times: around 7 hrs (Red), 48 hrs (Green), 70 hrs (Yellow) for (D) no particles, (E) 102.2 µm PMMA, (F) 9.9 µm PMMA with 60 mM $MgCl_2$concentration.

Figure 5.9D-F confirm the same patterns in ice recrystallization, with the diffusion coefficient increasing for the samples containing no particles due to the size of veins increasing during the recrystallization process; increasing less in the presence of 102.2 µm particles; and not increasing at all in the presence of 9.9 µm particles. This indicates that the particles pin the ice crystal size to the size of their pores.

As described by Equation 5.4 and 5.6, the short and long-time limits of the displacement time dependent diffusion behavior of Fig. 5.9D-F provide access to the structural parameters of the porous media (Mitra et al., 1993; Sen, 2004). The short-time limit $D(\Delta)$ data gives the pore surface area to volume ratios (S/V) shown in Figure 5.10A. The tortuosity values found through the Pade approximation are shown in Figure 5.10B for the sample containing 102.2 μm particles and no particles. In the sample containing 9.9 μm particles tortuosity values were divergent indicating isolated pores (Callaghan, 2011). Recrystallization through a ripening process is known to occur in ice and samples will recrystallize as large ice grains grow at the expense of the smaller grains dissolving to reduce interfacial energy (Bray, 2002; Brox et al., 2015). The relatively high temperature $-7.7℃$ in day 2 enhances this process, making it measurable during day 3. Recrystallization leads to changes that occur in an ice samples S/V and tortuosity as a function of ice aging and thus the change of S/V corresponding to larger liquid veins, and tortuosity slightly decreases with grain growth, which indicate the change of ice grain size in the sample.

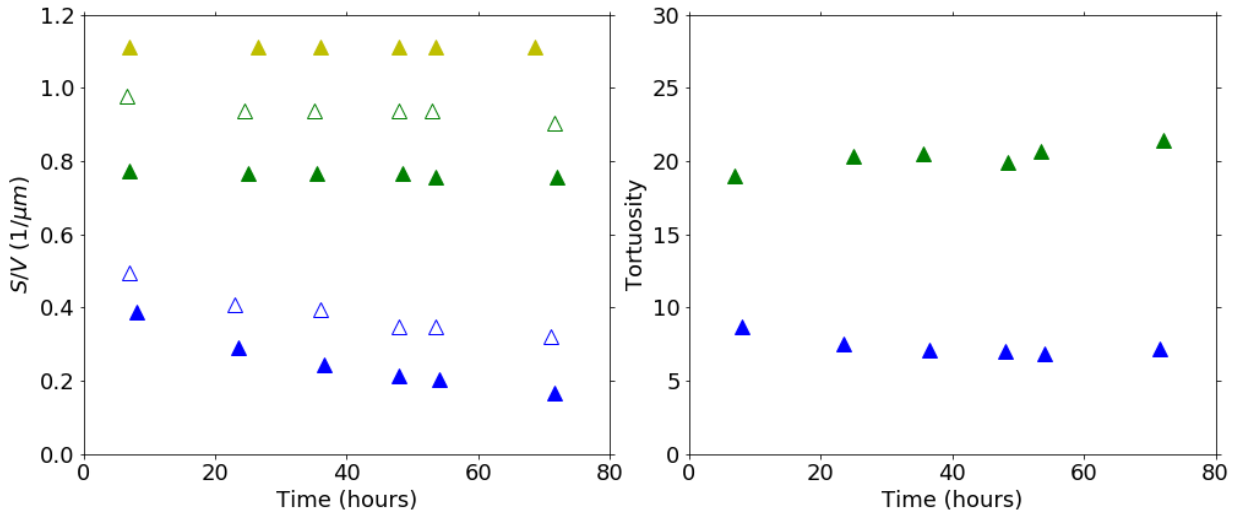

Figure 5.10: S/V ratio and tortuosity determined from displacement time dependent PGSE (A) S/V as a function of time at $-7.7℃$. 60 mM $MgCl_2$ concentration containing no particles (blue), 102.2 µm PMMA (Green) and 9.9 µm PMMA (Yellow) and S/V from CPMG (Δ) and from PGSE (▲). (B) Tortuosity calculated from PGSE as a function of time at $-5.6℃$.

Additionally, the faster change rate of ice grain size of the no particle sample compared with the sample containing 102.2 µm particles was confirmed in MRI experiments, which are shown in Figure 5.11. The faster changing rate of S/V ratio and tortuosity in the no particle sample than the 102.2 µm sample manifest the possibility that the existence of PMMA particles prohibit the process of ice recrystallization. In previous work, NMR was used to investigate this recrystallization through the use of PGSE NMR and our calculated tortuosity lies in the range of what they observed as a function of ice aging (Brown et al., 2012; Brown et al., 2014).

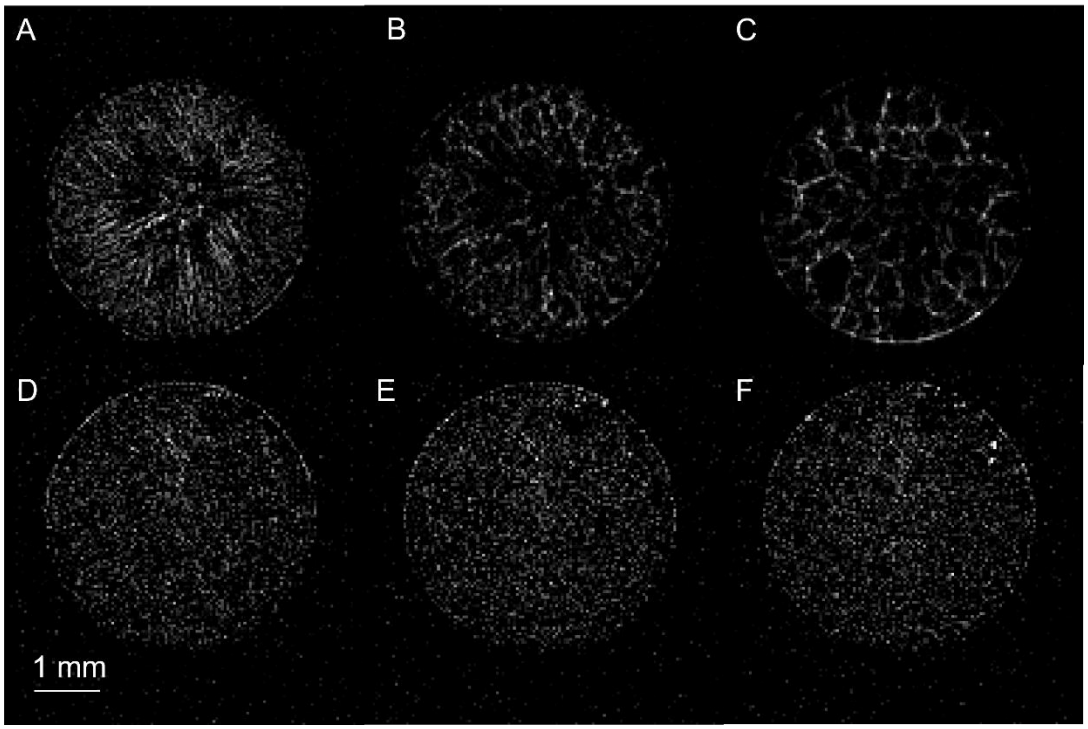

Figure 5.11: Cross-sectional MR images of vein network in 60mM $MgCl_2$ concentration ice samples at −5.6℃. Top: no particles. Bottom: 102.2 μm PMMA. Left to right: the aging time after initial freezing t = 2.5, 21.5, 59.5 h for A, B, C (top) and D, E, F (bottom) respectively. The veins in the 9.9 and 0.4 μm PMMA samples were not able to be resolved with MRI.

Conclusions

Using non-invasive NMR methods, the unfrozen vein network structure in porous media has been studied with respect to temperature, particle size and salt concentration. With larger particle sizes, the water content is dominated by the solute effect, whereas the high curvature introduced by the small particles leads to a higher water content and less dependence on solute concentration. The S/V, which reflects the pore size structure of the vein network has been

probed with both CPMG and PGSE NMR measurement techniques and used to calculate the surface relaxivity. Vein size and ice grain size have been estimated based on the water content and S/V data. PGSE and MRI experiments were used to monitor the ice recrystallization process for selected samples and show the unfrozen vein network structure changes over time when no particles are present. However, ice veins do not grow when the ice grains are pinned by the particles. These findings provide unique data from unfrozen vein networks in frozen porous media and provide a basis for future studies of ice structures in complex porous systems.

Acknowledgements

This work was supported by Solar System Workings Grant NNX15AH99G. H.G.S and A.W.R. acknowledge support from NASA grant 80NSSC18K0012. J.D.S. and S.L.C. thank the M.J. Murdoch Charitable Trust and NSF MRI program for equipment funding. P.L. thanks Jennifer Brown for valuable discussions.

References

Bray, A.J., 2002. Theory of phase-ordering kinetics. Advances in Physics, 51(2): 481-587.

Brown, J.R., Brox, T.I., Vogt, S.J., Seymour, J.D., Skidmore, M.L. and Codd, S.L., 2012. Magnetic resonance diffusion and relaxation characterization of water in the unfrozen vein network in polycrystalline ice and its response to microbial metabolic products. Journal of Magnetic Resonance, 225: 17-24.

Brown, J.R., Seymour, J.D., Brox, T.I., Skidmore, M.L., Wang, C., Christner, B.C., Luo, B.-H. and Codd, S.L., 2014. Recrystallization inhibition in ice due to ice binding protein activity detected by nuclear magnetic resonance. Biotechnology Reports, 3: 60-64.

Brox, T.I., Skidmore, M.L. and Brown, J.R., 2015. Characterizing the internal structure of laboratory ice samples with nuclear magnetic resonance. Journal of Glaciology, 61(225): 55-64.

Callaghan, P.T., 2011. Translational dynamics and magnetic resonance: principles of pulsed gradient spin echo NMR. Oxford University Press.

Carr, H.Y. and Purcell, E.M., 1954. Effects of diffusion on free precession in nuclear magnetic resonance experiments. Physical review, 94(3): 630.

Chen, J., Mei, S., Irizarry, J.T. and Rempel, A.W., 2020. A Monte Carlo approach to approximating the effects of pore geometry on the phase behavior of soil freezing. Journal of Advances in Modeling Earth Systems, 12(10): e2020MS002117.

Chen, J. and Rempel, A.W., 2019a. Ice in granular media, https://gitlab.com/jzchenjz/ice-in-granular-media.

Chen, J. and Rempel, A.W., 2019b. Packing of spherical particles, https://gitlab.com/jzchenjz/packing-of-spherical-particles.

Dash, J., Rempel, A. and Wettlaufer, J., 2006. The physics of premelted ice and its geophysical consequences. Reviews of modern physics, 78(3): 695.

Dedovets, D., Monteux, C. and Deville, S., 2018. Five-dimensional imaging of freezing emulsions with solute effects. Science, 360(6386): 303-306.

Deville, S., 2017. Freezing colloids: observations, principles, control, and use: applications in materials science, life science, earth science, food science, and engineering. Springer.

Eide, L.I. and Martin, S., 1975. The Formation of Brine Drainage Features in Young Sea Ice∗. Journal of Glaciology, 14(70): 137-154.

Grimm, R.E., Stillman, D.E., Dec, S.F. and Bullock, M.A., 2008. Low-frequency electrical properties of polycrystalline saline ice and salt hydrates. The Journal of Physical Chemistry B, 112(48): 15382-15390.

Hardy, S., 1977. A grain boundary groove measurement of the surface tension between ice and water. Philosophical Magazine, 35(2): 471-484.

Hürlimann, M.D., Latour, L.L. and Sotak, C.H., 1994. Diffusion measurement in sandstone core: NMR determination of surface-to-volume ratio and surface relaxivity. Magnetic resonance imaging, 12(2): 325-327.

Kaptay, G., 2012. The Gibbs equation versus the Kelvin and the Gibbs-Thomson equations to describe nucleation and equilibrium of nano-materials. Journal of Nanoscience and Nanotechnology, 12(3): 2625-2633.

Kleinberg, R.L., Kenyon, W.E. and Mitra, P.P., 1994b. Mechanism of Nmr Relaxation of Fluids in Rock. Journal of Magnetic Resonance Series A, 108(2): 206-214.

Meiboom, S. and Gill, D., 1958. Modified spin‐echo method for measuring nuclear relaxation times. Review of scientific instruments, 29(8): 688-691.

Mitchell, J., Webber, J.B.W. and Strange, J.H., 2008. Nuclear magnetic resonance cryoporometry. Physics Reports, 461(1): 1-36.

Mitra, P.P., Sen, P.N. and Schwartz, L.M., 1993. Short-time behavior of the diffusion coefficient as a geometrical probe of porous media. Physical review. B, Condensed matter, 47(14): 8565.

Mitra, P.P., Sen, P.N., Schwartz, L.M. and Le Doussal, P., 1992. Diffusion propagator as a probe of the structure of porous media. Physical review letters, 68(24): 3555.

Nye, J., 1989. The geometry of water veins and nodes in polycrystalline ice. Journal of Glaciology, 35(119): 17-22.

Petrov, O.V. and Furó, I., 2009. NMR cryoporometry: Principles, applications and potential. Progress in Nuclear Magnetic Resonance Spectroscopy, 2(54): 97-122.

Price, P.B., 2000. A habitat for psychrophiles in deep Antarctic ice. Proceedings of the National Academy of Sciences, 97(3): 1247-1251.

Rempel, A., 2007. Formation of ice lenses and frost heave. Journal of Geophysical Research: Earth Surface, 112(F2).

Rempel, A.R. and Rempel, A.W., 2016. Intrinsic evaporative cooling by hygroscopic earth materials. Geosciences, 6(3): 38.

Sen, P.N., 2004. Time‐dependent diffusion coefficient as a probe of geometry. Concepts in Magnetic Resonance Part A, 23(1): 1-21.

Sizemore, H.G., Zent, A.P. and Rempel, A.W., 2015. Initiation and growth of martian ice lenses. Icarus, 251: 191-210.

Sofie, S.W. and Dogan, F., 2001. Freeze casting of aqueous alumina slurries with glycerol. Journal of the American Ceramic Society, 84(7): 1459-1464.

Song, Y.-Q., 2013. Magnetic resonance of porous media (MRPM): A perspective. Journal of Magnetic Resonance, 229: 12-24.

Stejskal, E.O. and Tanner, J.E., 1965. Spin diffusion measurements: spin echoes in the presence of a time‐dependent field gradient. The journal of chemical physics, 42(1): 288-292.

Stillman, D.E., Michaels, T.I., Grimm, R.E. and Harrison, K.P., 2014. New observations of martian southern mid-latitude recurring slope lineae (RSL) imply formation by freshwater subsurface flows. Icarus, 233: 328-341.

Strange, J.H., Rahman, M. and Smith, E., 1993. Characterization of porous solids by NMR. Physical review letters, 71(21): 3589.

Valiullin, R. and Furó, I., 2002. Phase separation of a binary liquid mixture in porous media studied by nuclear magnetic resonance cryoporometry. The Journal of chemical physics, 116(3): 1072-1076.

Venkataramanan, L., Song, Y.-Q. and Hurlimann, M.D., 2002. Solving Fredholm integrals of the first kind with tensor product structure in 2 and 2.5 dimensions. IEEE Transactions on Signal Processing, 50(5): 1017-1026.

Weeks, W., 2010. On sea ice. University of Alaska Press.

Weeks, W.F. and Ackley, S.F., 1986. The growth, structure, and properties of sea ice, The geophysics of sea ice. Springer, pp. 9-164.

CHAPTER SIX

RECRYSTALLIZATION INHIBITION DUE TO ICE-BINDING PROTEIN ACTIVITY IN FROZEN POROUS MEDIA

Contributions of Authors and Co-Authors

Manuscript in Chapter Six

Author: Peng Lei

Contributions: Methodology, Investigation, Formal analysis, Data Curation, Visualization, Writing – Original Draft.

Co-Author: Joseph D. Seymour

Contributions: Methodology, Supervision, Project administration, Writing - Review & Editing.

Co-Author: Sarah L. Codd

Contributions: Methodology, Supervision, Project administration, Funding acquisition, Writing - Review & Editing.

Co-Author: David E. Stillman

Contributions: Methodology, Data Curation, Supervision, Funding acquisition, Writing - Review & Editing.

Co-Author: Katie Primm

Contributions: Data Curation, Writing - Review & Editing.

Co-Author: Bing-Hao Luo

Contributions: Methodology, Data Curation.

Manuscript Information Page

Peng Lei, Sarah L. Codd, Joseph D. Seymour, David E. Stillman, Katie Primm and Bing-Hao Luo

Cryobiology

Status of Manuscript: (Put an x in one of the options below)

__X__ Prepared for submission to a peer-reviewed journal

____ Officially submitted to a peer-review journal

____ Accepted by a peer-reviewed journal

___ Published in a peer-reviewed journal

Elsevier, Inc.

RECRYSTALLIZATION INHIBITION DUE TO ICE-BINDING PROTEIN ACTIVITY IN FROZEN POROUS MEDIA

Abstract

Ice binding proteins (IBP) are widely discovered in psychrophilic organisms, including fish, plants, insects and bacteria. These proteins bind ice to inhibit the growth of ice crystals and maintain the stabilization of the surrounding environment. They are interesting for industry due to their non-toxic properties compared with the chemical additives in the frozen food and the cryopreservation industries. Therefore, it's essential to understand how ice-binding proteins influence ice structure. Here nuclear magnetic resonance (NMR) techniques are used to monitor the liquid network in different concentrations of brine ice samples with and without IBP produced from the V3519-10 organism over months. This work investigates ice structure and enhances the understanding of the impact of IBP.

Introduction

Water is widely spread on Earth and can be found elsewhere in the Universe. Ice, as a phase of water, from the freezing of water under the freezing point, commonly exists during the winter, in the South Pole and the North Pole, and on some planets in the Universe like Mars. The freezing process of water is a of relevance in infrastructure maintenance during the winter (Beskow, 1947; Rempel, 2007), the food industry (Chen et al., 2021; Kaleda et al., 2018), and organism cryopreservation (Mangiagalli et al., 2020) etc. However, after freezing, frozen systems are not stable due to the dynamic status of the ice: in proper conditions, the tiny ice

crystals melt and merge into large crystals as time goes by. This phenomenon is called recrystallization. During this destructive process, the system's structure changes and brings problems to industry freezing technology applications (Chen et al., 2021).

Ice binding protein (IBP) is a protein extracted from a harsh climate tolerant organism, and improves the survivability of the organism under the freezing point by controlling the growth of ice crystals and stabilizing the chilly environment during this process (Brown et al., 2012; Brox et al., 2015; Raymond et al., 2008). It's an outstanding regulator for the growth of ice crystals and has the potential to solve the problem of ice recrystallization in the industry as a non-toxic additive or by introducing it to organisms genetically (Chen et al., 2021; Qin et al., 2007). In 2020, a $4 million market was estimated for IBPs, and by 2026 it's projected to reach $27 million (Mangiagalli et al., 2020).

Different kinds of IBPs are observed in nature. The IBPs from fishes, plants and insects have been studied extensively. These IBPs mainly work inside the organism to prevent cellular damage (Hon et al., 1995; Kaleda et al., 2018). Comparatively, other kinds of IBPs, especially from microorganisms, work outside to stabilize the freezing environment and improve viability (Brox et al., 2015). Laboratory studies are needed to expand our understanding of the interactions of complex ice structure with these kinds of IBPs. In this work, the extracellular IBP produced by the bacterium V3519-10 from the Vostok ice core at 3519m has been used (Christner et al., 2001; Raymond et al., 2008). This IBP inhibits the recrystallization process by preventing water molecules from joining along the a-axis as the IBP selectively binds to the prism facet of ice. As a non-destructive method, NMR techniques, including measurements of the molecular diffusion and the relaxation rate, are used to investigate the unfrozen brine vein

distribution and the structure of ice with the influence of IBP (Brown et al., 2012; Brox et al., 2015).

Methods

Sample preparation

The cold tolerance bacterium V3519-10 was discovered in the Vostok ice core from glacial ice at 3519m(Christner et al., 2001; Raymond et al., 2008). The extracellular recombinant IBP (rIBP) was obtained by filtering the supernatant generated from the bacterium V3519-10, grown in R2 liquid broth at 4°C to reach an 0.22 optical density OD595. The supernatant was recovered by centrifuging the culture at 5000g for 30 min at 4°C. The filters used were Ultra-15 centrifugal filters with a nominal threshold of 30kDa. Colleagues at Louisiana State University finished this process. And spectrophotometry NanoDrop ND-1000 was used to measure the concentration of the rIBP.

Brines of 30, 60 and 120 mM $MgCl_2$ solutions and rIBP were used to construct samples. Six samples were prepared at these three specific concentrations with or without rIBP added. One extra sample at 60 mM $MgCl_2$ with rIBP was specifically made to verify the reproducibility of the experiments. With a pipette, the brines were first loaded into 5 mm NMR tubes, then the rIBP was added to the solution to make the total rIBP concentration $4\mu g/mL$ in the sample. To reduce the temperature gradient during the measurement caused by nitrogen gas flow, the height of the solution in the NMR tube was approximately 3.5 cm to decrease the size of the samples. Then the samples were frozen at $-20℃ \pm 2℃$ in a deep, firm foam container to ensure the freezing rate was slow and from top to bottom; visual checks were used to drop out any samples

including air bubbles or frozen improperly. Then samples were moved to a cold room at -10℃ for ice aging. Before the sample was inserted, the NMR spectrometer was pre-cooled to -10℃ with nitrogen gas for at least 10 mins. Before the measurement, another 30 mins was allotted to allow thermal equilibrium to be reached for the whole device, including the sample. The samples were stored in the -10℃ cold room between measurements.

NMR experiments

An Avance III Bruker 250 MHZ spectrometer was used for all experiments. The NMR measurements were conducted with a standard Micro 5 NMR probe with an 8 mm RF coil. A Bruker VTU temperature control unit was used to control the temperature during the measurements. A water chiller was used to maintain the probe's temperature everywhere except in the measurement region at 20 ℃. While the temperature in the measurement region was calibrated to $-10℃$, the temperature range from bottom to top was around $-10.5 \pm 0.5℃$ to $-9.5 \pm 0.5℃$.

Unfrozen water content was measured from the NMR signal magnitude by analyzing the initial amplitude with regression analysis. A totally melted reference sample was measured first as the baseline calibration, then the frozen samples were measured, and the amplitude of initial signals were compared with the result from the reference sample to obtain a calibrated unfrozen water content percentage since only the liquid water in the sample generates an NMR signal. A standard Carr-Purcell-Meiboom-Gill (CPMG) spin-echo train was used to measure the unfrozen water content and the T_2 distribution with a fixed pulse power of 50 W, 90º RF pulse time 6.0-8.0 μs, echo time of 400 μs and echo number of 1600. 1D Laplace inverse analysis in MATLAB was used to analyze the T_2 relaxation distribution. (Callaghan, 2011; Venkataramanan et al.,

2002). The self-diffusion experiments used the pulsed gradient spin echo (PGSE) sequence with variable observation times to track the displacement over times Δ from 10 to 1000 ms with parameters: gradient duration time (δ) of 2 ms, an echo time (2τ) of 8.38 ms and 16 steps of gradient amplitude from the minimum gradient of 0.0649 T/m to the maximum gradient value ranging from 1 to $0.145\ T/m$ depending on the sample and the diffusion observation time Δ used. A standard Stejskal-Tanner plot was used to calculate the effective diffusion coefficient D as a function of Δ (Stejskal and Tanner, 1965).

A standard multi-spin-multi echo (MSME) sequence was used to generate the NMR images (MRI) with the same probe and RF coil. The axial images were obtained from a 0.5 mm thickness of the frozen sample in the center of the RF coil with a 43 × 43 μm spatial resolution of the axial transverse cross-section over a 128×128 matrix size and $5.5\ \times\ 5.5$ mm field of view. The sagittal images were obtained with the same parameters except for a $256\ \times\ 128$ matrix size and $11\ \times\ 5.5$ mm field of view were used.

Experimental protocol

Freeze samples around $-20\ ℃ \pm 2℃$ in a deep, firm foam container for around 2 to 4 hours, then move to a $-10\ ℃$ cold room for storage.

Run CPMG, PGSE (Δ range [10,1000] ms) and MRI at $-10\ ℃$ over a several month time period.

Data analysis

Diffusion Coefficients

Stejskal-Tanner plots were used to obtain Diffusion coefficients D over a range of observation times Δ (Stejskal and Tanner, 1965). Effective diffusion coefficients are close to the free diffusion coefficient in the short time regime due to limited interaction of molecules with the boundary. The free diffusion coefficients were obtained by extrapolating the diffusion coefficients in the short time regime back to zero. This value was considered to be a constant for all of the datasets at the same concentration while the temperature was fixed. Here, for 30mM, the free diffusion coefficient D_0 was set at $6.04 \times 10^{-10}\ m^2/s$; for 60 mM, it was $7.16 \times 10^{-10}\ m^2/s$; and for 120 mM, it was $5.97 \times 10^{-10}\ m^2/s$. For the same reason, in porous media with a pore length a, when the observation time is short and satisfies the condition $\Delta \ll a^2/D_0$, only the motion of protons within the diffusion length $\sqrt{D_0\Delta}$ of the surface S of the boundary in the pore space V is restricted (Latour et al., 1993; Mitra et al., 1993; Mitra et al., 1992). The effective diffusion in this situation can be written as (Hürlimann et al., 1994):

$$\frac{D_{\text{eff}}(\Delta)}{D_0} = 1 - \frac{4\sqrt{D_0\Delta}}{9\sqrt{\pi}}\frac{S}{V}. \tag{6.1}$$

and the pore property S/V, in this case, can be extracted.

In the long time regime, the motion of all protons is limited by the boundary of the pore formed by the ice and water, and the effective diffusion is directly associated with the tortuosity α, the ratio of the actual travel path of a proton to the geometric path (Bear, 1988):

$$\frac{D_{eff}(\infty)}{D_0} = \frac{1}{\alpha} \tag{6.2}$$

Due to the relaxation of the spin during the measurement, the time required to access the long time regime is usually out of the time range that can be measured. Thus, with the calculated free diffusion coefficient and the S/V, a Pade approximation was used to extract the tortuosity α and the fitting parameter θ, which is the time scale to diffuse to reach the α limit (Callaghan, 2011; Hürlimann et al., 1994):

$$\frac{D_{\text{eff}}(t)}{D_0} = 1 - \left(1 - \frac{1}{\alpha}\right) \frac{\frac{4}{9\sqrt{\pi}} \frac{S}{V_{\text{p}}} \sqrt{D_0 t} + \left(1 - \frac{1}{\alpha}\right) \frac{t}{\theta}}{\left(1 - \frac{1}{\alpha}\right) + \frac{4}{9\sqrt{\pi}} \frac{S}{V_{\text{p}}} \sqrt{D_0 t} + \left(1 - \frac{1}{\alpha}\right) \frac{t}{\theta}}, \tag{6.3}$$

Calculation of S/V from CPMG data

The S/V data can be extracted from the PGSE data. However, the data from the CPMG is also associated with S/V with the diffusion term and bulk T_2 term also having an influence on the T_2 measured at the same time (Callaghan, 2011):

$$\frac{1}{T_2} = \frac{1}{T_{2,\text{bulk}}} + \rho_2 \frac{S}{V} + \frac{\gamma^2 \langle G_0^2 \rangle D_0 (2\tau)^2}{12} \tag{6.4}$$

The CPMG data was measured with different τ times, which influence the diffusion term. Here $1/T_{2\,\text{shift}}$ was introduced to define the influence on the diffusion term from $\tau = 40\mu s$ to $400\mu s$. By calibrating the T_2 distribution data with $T_{2\,\text{shift}}$ and introducing a surface relaxivity from our previous project (Chapter 5) of characterization of unfrozen brine vein distribution and

structure in model packed beds, the S/V can be directly extracted from the CPMG data and was compared and discussed with the data from the PGSE experiment in the result and discussion section (Lei et al., 2022).

Monitoring the ice recrystallization process

The samples were frozen at $-20\ ℃ \pm 2℃$ in a deep, firm hole in a foam container. This specific way of freezing the sample ensured they were frozen from top to bottom slowly. Freezing from top to bottom causes the unfrozen water to distribute uniformly in the frozen sample rather than being rejected to the sample's center and forming a single vertical unfrozen pore where freezing occurs from the sides. Freezing slowly forbids the formation of cloud ice structure or developing a layer of unfrozen water in the horizontal direction due to the rapid formation of ice from the top direction applying a high pressure to the rest of the sample. The sample was measured with CPMG, PGSE and MRI at day 1, day 3, day 5 until around 45 days. During this process, the ice structure changes were monitored by comparing the same measurements at different ice aging times.

Result and Discussion

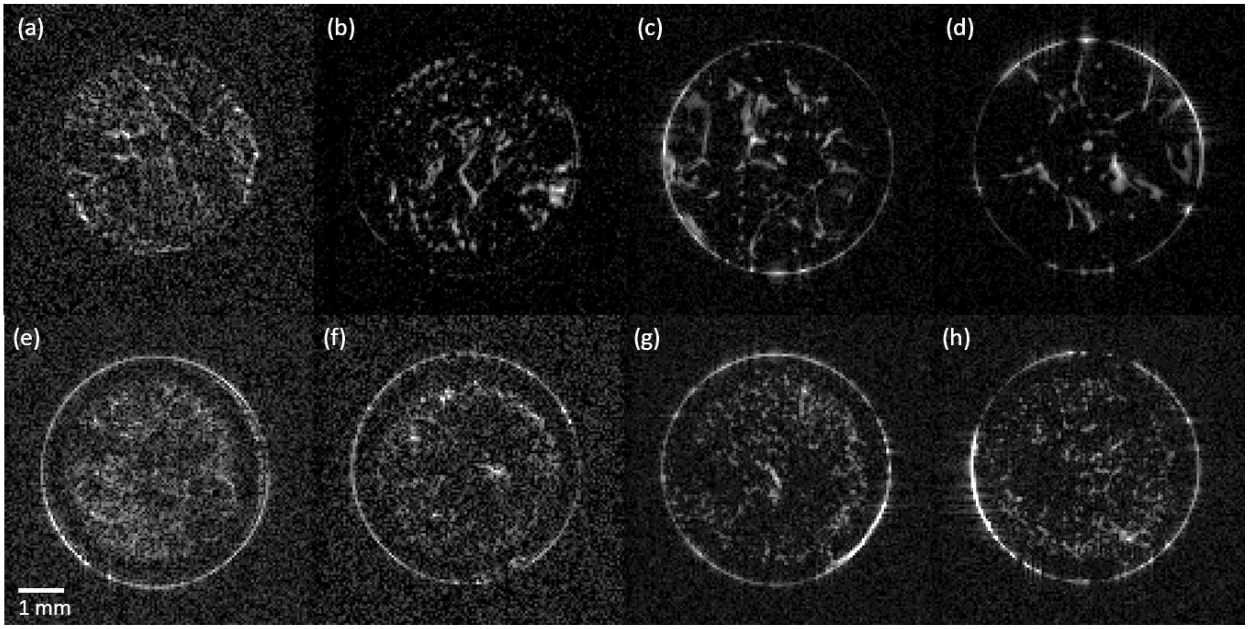

Figure 6.1: Cross-sectional MR images of vein network in ice samples at -10 ℃. Top: 60mM $MgCl_2$ ice sample. Bottom: 60mM $MgCl_2$ with $4\mu g/mL$ rIBP ice sample. The aging time after initial freezing for (a) to (d) is 1, 6, 23, 44 days; for (e) to (h) is 1, 8, 23, 44 days.

The top row of Fig.6.1 shows the top transverse cross-section images of the 60mM $MgCl_2$ (brine) ice sample from day 1 to day 44; the bottom row shows the images of 60mM $MgCl_2$ with $4\mu g/mL$ rIBP ice sample in the same time frame. The ice recrystallization phenomenon was observed as the size of the ice crystals in the 60mM $MgCl_2$ ice sample kept increasing during the 44 days. In contrast, the change in the ice crystal size for the 60mM $MgCl_2$ with $4\mu g/mL$ rIBP ice sample is much smaller. The wider distribution of unfrozen water in the ice with rIBP indicates the existence of smaller ice crystals and a smaller vein network formed

by these ice crystals. In some areas, the black parts suggests the formation of some big ice crystals, compared with the 60mM $MgCl_2$ ice sample without rIBP; the smaller size of the black areas and the dispersed nature of the black areas strongly indicates the stabilization ability of the rIBP in the frozen porous media. The following section presents a more detailed analysis by combining CPMG and PGSE data.

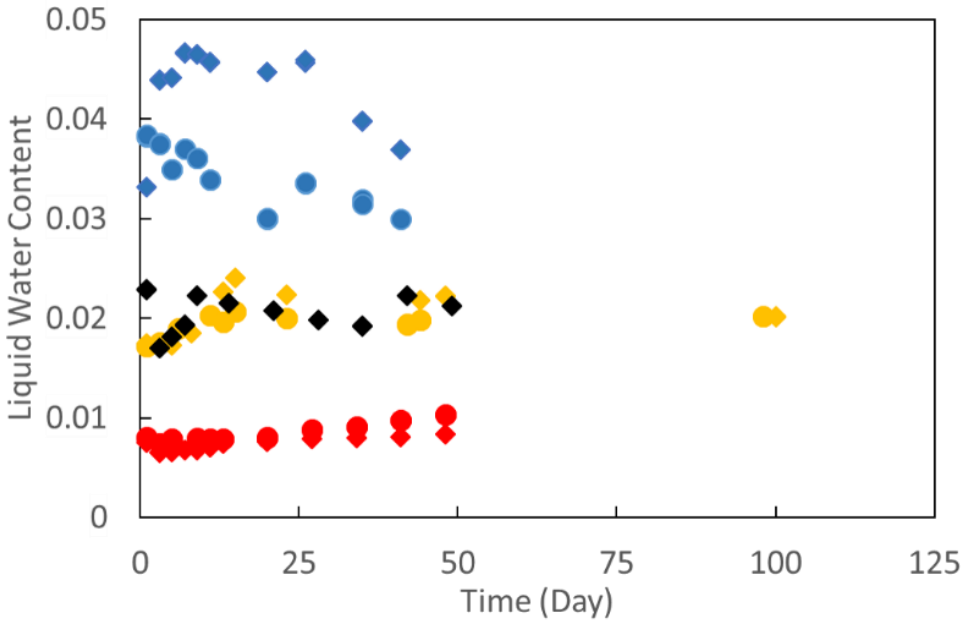

Figure 6.2: Liquid water content as a function of time at -10°C. Samples include 30 mM (red). 60mM (yellow), 120mM (blue) $MgCl_2$ brine with 4µg/mL rIBP (diamond) or without rIBP (filled circle), and one repeat 60mM brine with 4µg/mL rIBP (black diamond).

Liquid water content changes at first but then stays relative constant after around 13 days. After the liquid water content stablizes, they match our data from the previous ice-particle project in Chapter 5 (Lei et al., 2022). More experiments are needed to explore the change of water content in the first few days.

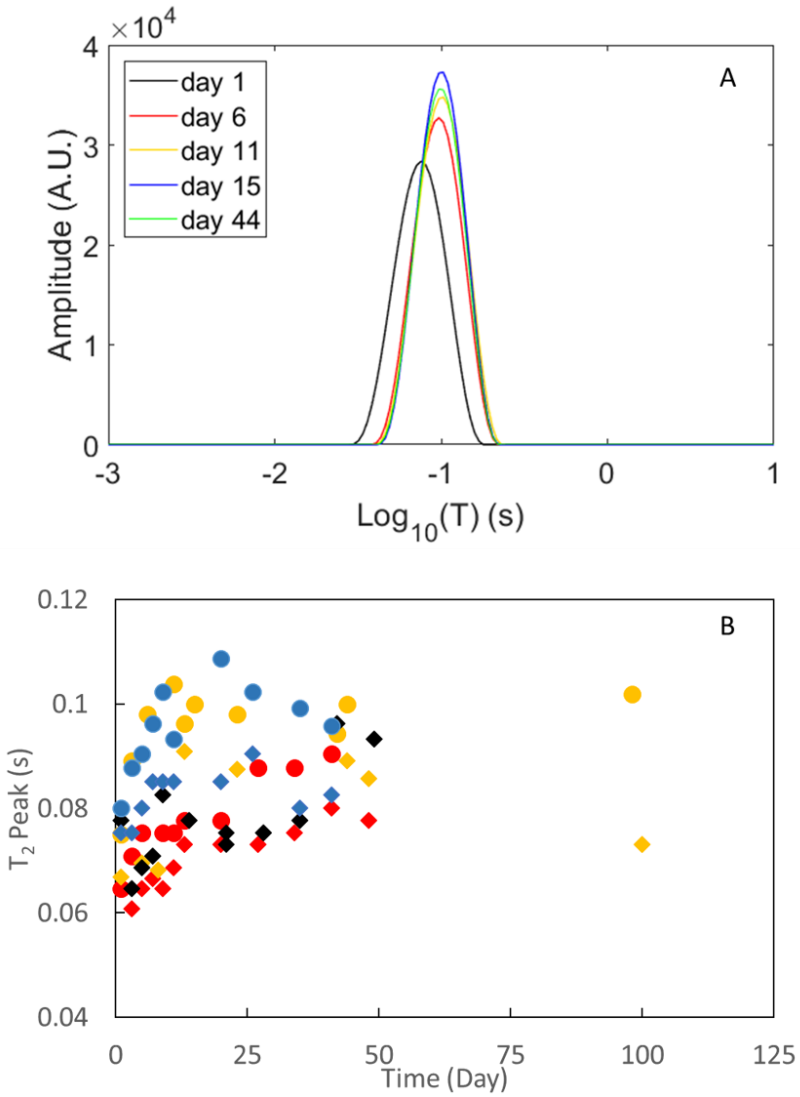

Figure 6.3: Representative T_2 relaxation time distributions as a function of time at $-10°C$ for, (A) 60mM brine at day 1 (black), day 6(red), day 11(yellow), day 15(blue), day 44 (green); (B) Changes in the T_2 relaxation time corresponding to the maximum signal for each day plotted for all samples. Samples include 30 mM (red). 60mM (yellow), 120mM (blue) $MgCl_2$ brine with 4µg/mL rIBP (diamond) or without rIBP (filled circle), and one repeat 60mM brine with 4µg/mL rIBP (black diamond).

T_2 distributions for the 60mM without rIBP at different aging times are shown in Figure 6.3(A). As the aging time increases, it is apparent that the T_2 distribution amplitude increases a

little in the beginning then stays relatively constant, and the whole T_2 distribution shifts to the right, which indicates an increase in mobility of the molecules. The distribution did not change much after day 13. The change in the amplitude and area under the peak reflects the increase in unfrozen water content in the first two weeks, then it maintains a relatively stable unfrozen water content in the 60mM without rIBP samples, the same result presented in Figure 6.2. The preference of the T_2 distribution for longer times indicates a structural change in the ice porous media towards larger pores and a related increase in S/V.

The extracted T_2 peak for these samples is shown in Figure 6.3(B). The brine sample has a longer T_2 value than the sample containing rIBP at the same concentration and ice aging time. And as time goes by, especially in the first two weeks, the increase in the T_2 peak value for the rIBP sample is much less than the sample without rIBP, indicating a smaller S/V ratio change. After two weeks, the rate change for the T_2 peak for the brine sample slows down due to the restrictions of the ice sample tube. As 5mm NMR tubes were used to make samples, the growth rate may be influenced by the boundary of the NMR tube when the size of the ice crystal approaches the same magnitude as the tubes. However, the 5mm NMR tube was selected as the optimal size. The temperature control is much more accurate than for a larger sample tube and a larger sample also means more energy for the NMR excitation, which may disturb the ice structure as protons will absorb the energy and melt the ice.

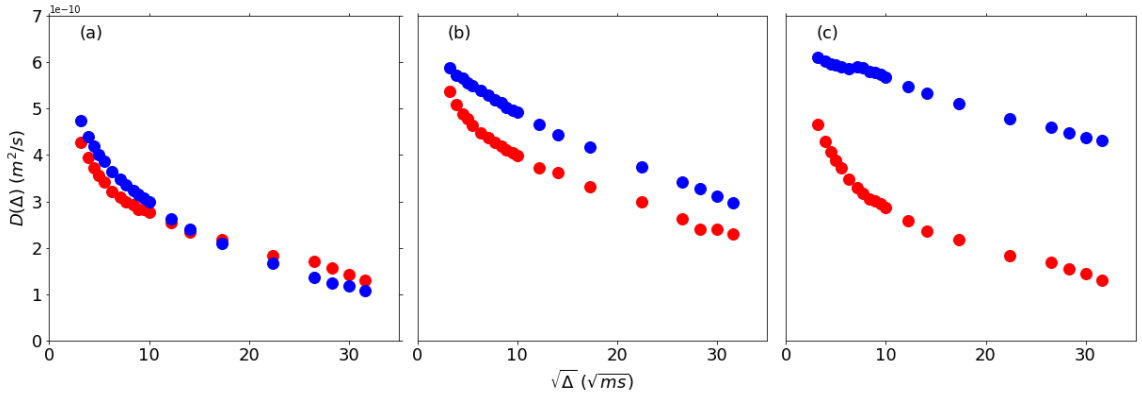

Figure 6.4: Diffusion coefficient as a function of square root of observation time at $-10°C$. Samples include 60mM $MgCl_2$ brine (blue dot) and 60mM $MgCl_2$ with 4µg/mL rIBP (red dot). The aging time after initial freezing for (a) is 1 day; for (b) is 23 days; for (c) is 98 days (60mM $MgCl_2$ brine sample) and 100 days (60mM $MgCl_2$ with 4µg/mL rIBP sample) respectively.

In Figure 6.4, the diffusion data correlates to the CPMG and MRI results since the effective diffusion coefficients for the 60mM $MgCl_2$ brine sample can be seen to increase with aging. In contrast, 60mM $MgCl_2$ with 4µg/mL rIBP sample did not change as significantly as the brine sample; at 100 days, the diffusion coefficients are close to those found on day 1. The increasing effective diffusion coefficient as the ice ages indicates a change in the ice structure reflecting the size of the vein network increasing so fewer protons are influenced by the boundary of the vein formed by ice crystals. The diffusion coefficients for the 60mM $MgCl_2$ brine sample on day 100 have an unexpected increase during displacement observation time $\Delta =$ 50 to 100 ms. Diffusion coefficients are expected to decrease as Δ increases. The 30mM diffusion data also demonstrated this increase even more significantly. This increase may be due to the convection of unfrozen water within the sample under the influence of the temperature gradient. The experiments need to be repeated before publication to enable solid conclusions.

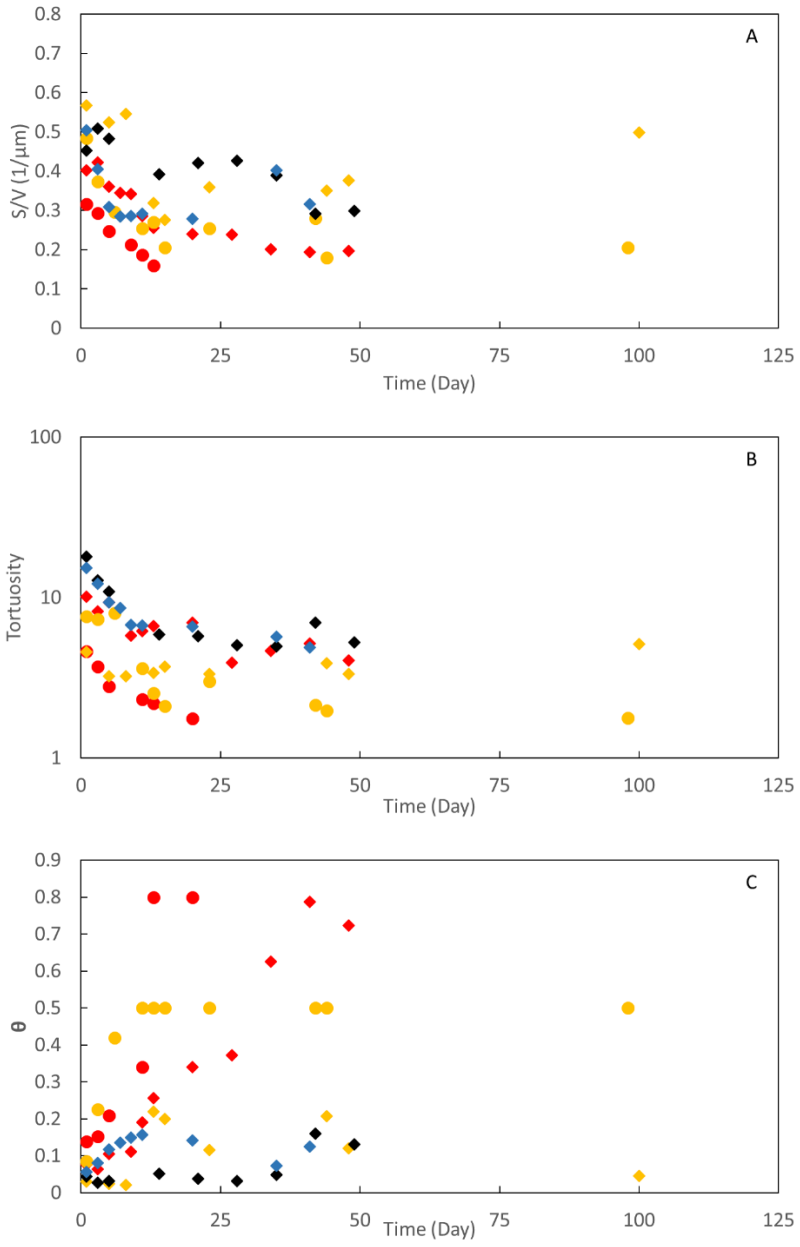

Figure 6.5: (A)Surface to volume ratio (calculated from PGSE data) as a function of time $-10°C$. (B) and (C) Tortuosity and fitting parameter θ from Pade fitting as a function of time $-10°C$. Samples include 30 mM (red). 60mM (yellow), 120mM (blue) $MgCl_2$ brine with 4µg/mL rIBP (diamond) or without rIBP (dot), and one repeat 60mM brine with 4µg/mL rIBP (black diamond).

As described above in Equations 6.1 and 6.2, the value of the effective diffusion coefficient D_{eff} over the short and long-times (Δ) is influenced by different geometric properties of the frozen porous media. Over the short time regime, the pore property S/V can be extracted from fitting to the dataset of diffusion coefficients in the observation time Δ up to $50\ ms$, and the result is shown in Figure 6.5(A). For the long-time observation time Δ, all protons have been influenced by the boundary so the tortuosity can be extracted with a Pade approximation fit according to Equation 6.2 and 6.3. The results are shown in Figure 6.5(B), and the fitting parameter θ, which indicates the time needed to reach the tortuosity limit, is shown in Figure 6.5(C). Same as discussion above, the experiments need to be repeated.

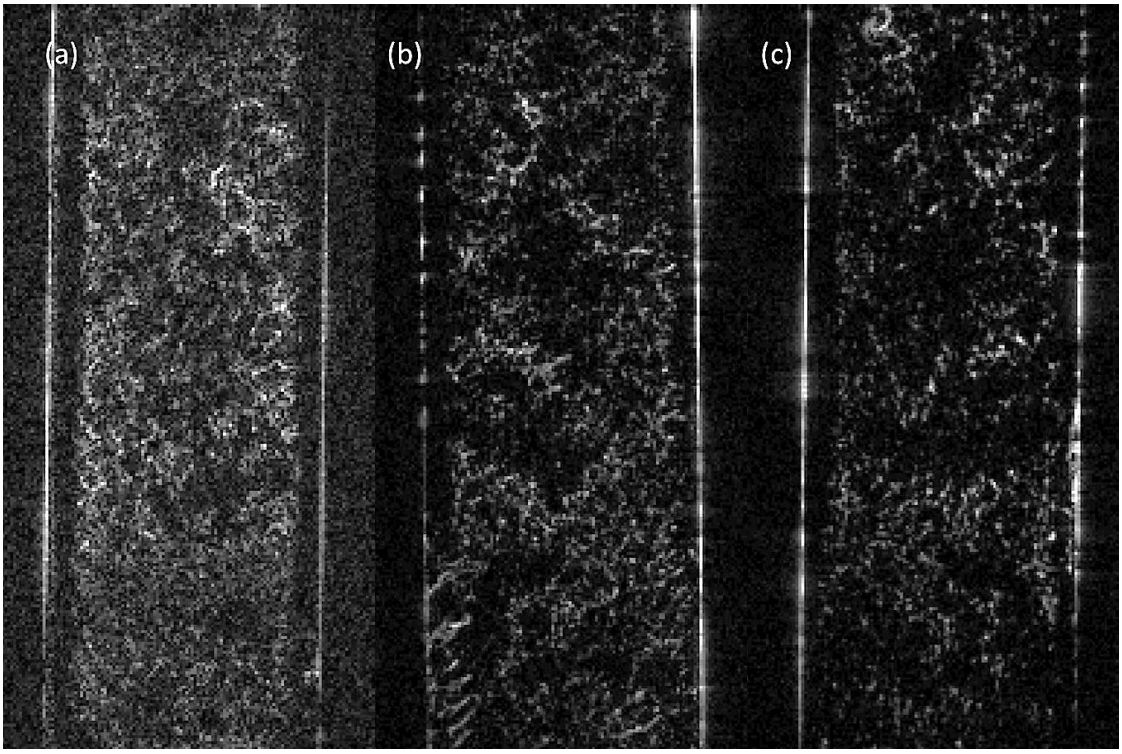

Figure 6.6: Vertical-sectional MR images of vein network in 60mM $MgCl_2$ with $4\mu g/mL$ rIBP ice sample at -10 ℃. The aging time after initial freezing for (a) to (c) is 1, 23, 44 days.

Recent studies suggest that the rIBP help to form a 3D network of tiny ice crystals(Kaleda et al., 2018). Even with the protein binding to the prism facet of the ice crystal, the ice crystal could still grow at these free sites and, in the end, form an inordinate but continuous giant ice crystal when IBP does not fully occupy the ice crystal growth site (Wang et al., 2016). At the same time, in regions that are saturated with IBP, the ice crystals remain in small size, therefore forming a continuous system which consists of one or several giant inordinate ice crystals with lots of small ice crystals aggregating around them and in this way forms a uniform 3D porous structure of ice. This phenomenon is also observed in our study as shown in Figure 6.1 and Figure 6.6: the imaging of the 60mM sample with rIBP clearly showed the formation process of big inordinate big ice crystals with lots of small ice crystals gathered around them. In contrast, the 60mM sample without rIBP shows separates ice crystals. This fact also explains why for the sample containing rIBP, the tortuosity decreased while the S/V didn't change much in the first five days: in these first few days, these isolated or semi-isolated pores began to connect under the influence of the rIBP and combine the vein network (or enlarge the vein network). During this process, the ice crystal size didn’t change much but the vein network formed (not only the network of unfrozen water but also a continuous network of ice) during this aggregate process which caused the tortuosity to change much quicker than S/V while for brine sample without rIBP both parameters changed quickly. The exception is the 120mM sample with rIBP, in which S/V also changes quickly during this process; this may be due to the higher water content, which enhanced the increase of vein size in the first few days and is shown in Figure 6.8. Notably, this confirms our understanding of the impact of IBP: to keep the water network open in the frozen systems to let bacteria survive in the harsh environment(Chen et al., 2021).

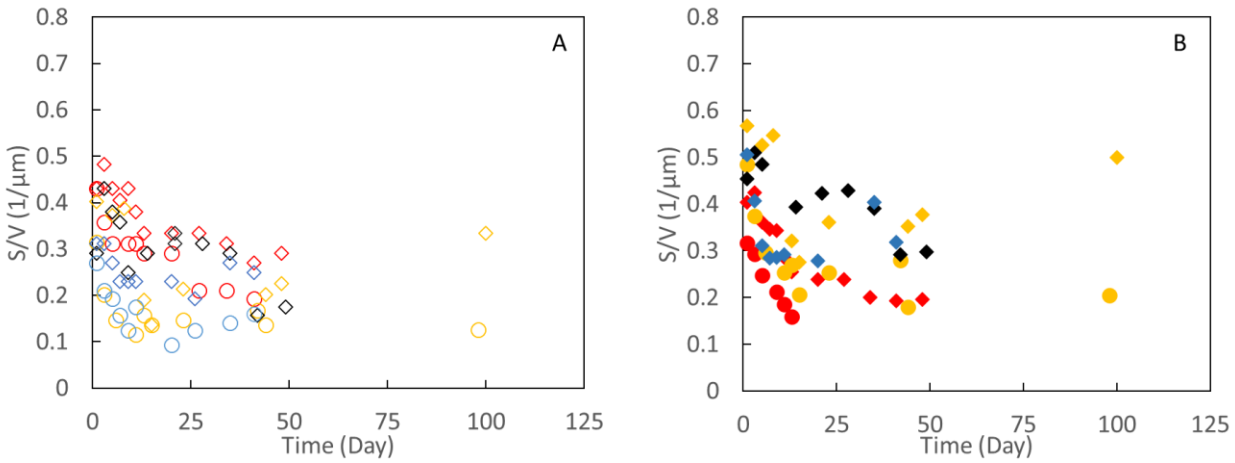

Figure 6.7: (A)Surface to volume ratio (calculated from CPMG data) as a function of time $-10°C$ (no fill). (B) Surface to volume ratio (calculated from PGSE data) as a function of time $-10°C$ (solid fill). Samples include 30 mM (red). 60mM (yellow), 120mM (blue) $MgCl_2$ brine with 4μg/mL rIBP (diamond) or without rIBP (filled circle), and one repeat 60mM brine with 4μg/mL rIBP (black diamond).

As described above, with the S/V from PGSE, the surface relaxivity can be calculated then used to calibrate the CPMG data to obtain S/V. Here, we use ρ = 18.62063 micron/s, obtained in our previous study, and we define a term $^1/_{T_{2shift}} = 6.81\ s^{-1}$, representing the diffusion term enhanced by the long τ time in Equation 6.4 and a constant bulk relaxation rate of 0.985s (Lei et al., 2022). The extracted S/V is from the CPMG data is shown and compared with the S/V from PGSE experiments in Figure 6.7. The results show the S/V calculated in these two different ways are similar, which confirms the accuracy of our method to calibrate the data from CPMG. This method introduces an accurate way to measure S/V from the CPMG sequence. The classic method PGSE is limited by the unfrozen water content percent and the reduced signal that occurs when applying a gradient. Compared with the PGSE method, the CPMG method is more

sensitive to much lower water content, which means CPMG can work with lower salt concentrations and much lower temperatures when less liquid water is present. In other words, this method shows the possibility to extend the sample type and temperature range of NMR technique application in frozen systems.

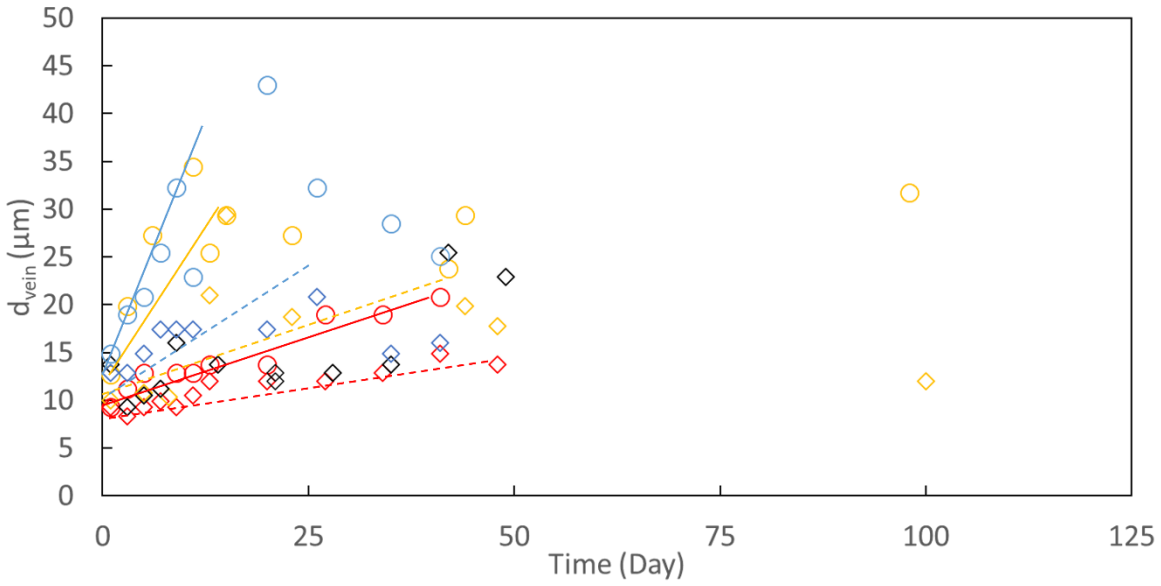

Figure 6.8: The size of vein network calculated from surface to volume ratio (from CPMG data) as a function of time $-10°C$. Samples include 30 mM (red). 60mM (yellow), 120mM (blue) $MgCl_2$ brine with 4µg/mL rIBP (diamond) or without rIBP (circle), and one repeat 60mM brine with 4µg/mL rIBP (black diamond). Lines are to guide the eye only: sample with rIBP (dash line) or without rIBP (solid line).

By modeling the vein network as three-grain junctions that treat the ice grain as a cylinder, the relationship between S/V and the vein size can be described as: $d_{vein} = \frac{4}{S/V}$ (Price, 2000). In Figure 6.8, all samples have a similar starting point of vein size, then the vein size of the 120mM and 60mM samples increases rapidly in the first few days before slowing down due

to the limitation of the NMR tube size. At the same time, the vein size of samples with rIBP grow at a much lower rate. The vein size for the 30mM sample increased slower than the 120mM and 60mM samples due to the lower water content limiting the growth rate of the vein size, but it's still clear that the size is larger than the 30mM sample with rIBP.

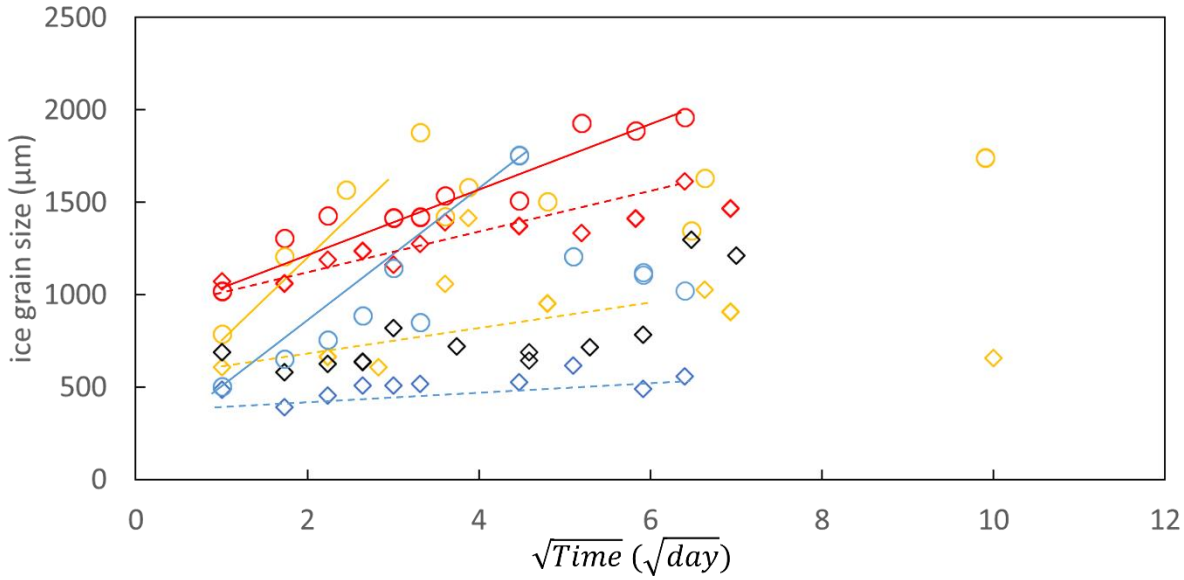

Figure 6.9: The size of ice grain calculated as a function of square root of time at $-10°C$. Samples include 30 mM (red). 60mM (yellow), 120mM (blue) $MgCl_2$ brine with 4μg/mL rIBP (diamond) or without rIBP (dot), and one repeat 60mM brine with 4μg/mL rIBP (black diamond). Lines are to guide the eye only: sample with rIBP (dash line) or without rIBP (solid line).

With known liquid water content ω, and the mean vein diameter d_m, the ice grain size can be estimated with the relationship $d_m = 0.34\delta\omega^{3/4}$ (Grimm et al., 2008; Price, 2000). In Figure 6.9, the results are shown as a function of the square root of time. Ice grain size growth is $t^{1/2}$ dependent: for samples containing rIBP, their ice grain growth shows a cursory linear

relationship with $t^{1/2}$ over the whole time (Ashton, 1989; Rempel, 2007). For samples without rIBP, it's clear that the ice grain grows quickly at a significant linear rate of $t^{1/2}$ in the first few days, then reaches the sample size limitation in two weeks, which matches our MRI, S/V and d_{vein} data.

Conclusions

With non-destructive NMR techniques, the dynamic structure of the unfrozen vein network with and without the influence of rIBP at different salt concentration have been studied as a function of time. MRI, PGSE and CPMG data confirmed that significant ice recrystallization occurred in the brine sample while the sample containing rIBP underwent a less significant change in ice crystal size in the same time frame. It indicates the rIBP inhibition influence on the growth of ice crystals. The method to estimate S/V directly from CPMG with calculated surface relaxivity and calibration to minimize the influence of diffusion has been tested, and the results match the results from the more traditional PGSE method. These findings provide firsthand data to describe the complex and dynamic structure of the unfrozen vein network. In future studies, with more advanced temperature control technology, the larger size of the sample may be able to introduce and track the ice grain growth rate over a longer time frame may with NMR techniques.

Acknowledgments

Solar System Workings Grant NNX15AH99G supported this study. JDS and SLC thank the M.J. Murdoch Charitable Trust and NSF MRI program for equipment funding.

References

Markets and markets. Antifreeze Proteins Market, https://www.marketsandmarkets.com/Market-Reports/antifreeze-protein-market-264931272.html.

Ashton, G.D., 1989. Thin ice growth. Water Resources Research, 25(3): 564-566.

Bear, J., 1988. Dynamics of fluids in porous media. Courier Corporation.

Beskow, G., 1947. Soil freezing and frost heaving with special application to roads and railroads.

Brown, J.R., Brox, T.I., Vogt, S.J., Seymour, J.D., Skidmore, M.L. and Codd, S.L., 2012. Magnetic resonance diffusion and relaxation characterization of water in the unfrozen vein network in polycrystalline ice and its response to microbial metabolic products. Journal of Magnetic Resonance, 225: 17-24.

Brox, T.I., Skidmore, M.L. and Brown, J.R., 2015. Characterizing the internal structure of laboratory ice samples with nuclear magnetic resonance. Journal of Glaciology, 61(225): 55-64.

Callaghan, P.T., 2011. Translational dynamics and magnetic resonance: principles of pulsed gradient spin echo NMR. Oxford University Press.

Chen, X., Shi, X., Cai, X., Yang, F., Li, L., Wu, J. and Wang, S., 2021. Ice-binding proteins: A remarkable ice crystal regulator for frozen foods. Critical Reviews in Food Science and Nutrition, 61(20): 3436-3449.

Christner, B.C., Mosley‐Thompson, E., Thompson, L.G. and Reeve, J.N., 2001. Isolation of bacteria and 16S rDNAs from Lake Vostok accretion ice. Environmental Microbiology, 3(9): 570-577.

Grimm, R.E., Stillman, D.E., Dec, S.F. and Bullock, M.A., 2008. Low-frequency electrical properties of polycrystalline saline ice and salt hydrates. The Journal of Physical Chemistry B, 112(48): 15382-15390.

Hon, W.-C., Griffith, M., Mlynarz, A., Kwok, Y.C. and Yang, D.S., 1995. Antifreeze proteins in winter rye are similar to pathogenesis-related proteins. Plant physiology, 109(3): 879-889.

Hürlimann, M.D., Latour, L.L. and Sotak, C.H., 1994. Diffusion measurement in sandstone core: NMR determination of surface-to-volume ratio and surface relaxivity. Magnetic resonance imaging, 12(2): 325-327.

Kaleda, A., Tsanev, R., Klesment, T., Vilu, R. and Laos, K., 2018. Ice cream structure modification by ice-binding proteins. Food chemistry, 246: 164-171.

Latour, L.L., Mitra, P.P., Kleinberg, R.L. and Sotak, C.H., 1993. Time-Dependent Diffusion Coefficient of Fluids in Porous Media as a Probe of Surface-to-Volume Ratio. Journal of Magnetic Resonance, Series A, 101(3): 342-346.

Lei, P., Young, M.W., Seymour, J.D., Stillman, D.E., Primm, K., Sizemore, H.G., Rempe, l.W. and Codd, S.L., 2022. NMR Characterization of unfrozen brine vein distribution and structure in model packed beds. Cold Regions Science and Technology.

Mangiagalli, M., Brocca, S., Orlando, M. and Lotti, M., 2020. The "cold revolution". Present and future applications of cold-active enzymes and ice-binding proteins. New biotechnology, 55: 5-11.

Mitra, P.P., Sen, P.N. and Schwartz, L.M., 1993. Short-time behavior of the diffusion coefficient as a geometrical probe of porous media. Physical review. B, Condensed matter, 47(14): 8565.

Mitra, P.P., Sen, P.N., Schwartz, L.M. and Le Doussal, P., 1992. Diffusion propagator as a probe of the structure of porous media. Physical review letters, 68(24): 3555.

Price, P.B., 2000. A habitat for psychrophiles in deep Antarctic ice. Proceedings of the National Academy of Sciences, 97(3): 1247-1251.

Qin, W., Doucet, D., Tyshenko, M. and Walker, V., 2007. Transcription of antifreeze protein genes in Choristoneura fumiferana. Insect molecular biology, 16(4): 423-434.

Raymond, J.A., Christner, B.C. and Schuster, S.C., 2008. A bacterial ice-binding protein from the Vostok ice core. Extremophiles, 12(5): 713-717.

Rempel, A., 2007. Formation of ice lenses and frost heave. Journal of Geophysical Research: Earth Surface, 112(F2).

Stejskal, E.O. and Tanner, J.E., 1965. Spin diffusion measurements: spin echoes in the presence of a time ‐ dependent field gradient. The journal of chemical physics, 42(1): 288-292.

Venkataramanan, L., Song, Y.-Q. and Hurlimann, M.D., 2002. Solving Fredholm integrals of the first kind with tensor product structure in 2 and 2.5 dimensions. IEEE Transactions on Signal Processing, 50(5): 1017-1026.

Wang, C., Oliver, E.E., Christner, B.C. and Luo, B.-H., 2016. Functional Analysis of a bacterial antifreeze protein indicates a cooperative effect between its two ice-binding domains. Biochemistry, 55(28): 3975-3983.

CHAPTER SEVEN

CONCLUSION

The research presented in this thesis explores the ability to utilize nuclear magnetic resonance (NMR) techniques to characterize the internal liquid phase structure of ice and frozen porous media. The unfrozen water exists in ice and frozen porous media due to the freezing point depression caused by the solute effect, surface energy and wetting (Chen et al., 2020; Hardy, 1977). For these ice-liquid coexistence systems, the unfrozen water exists as wetting films in the interface of ice crystals or particles and forms a liquid vein network. The presence of solid particulates and ice-binding protein (IBP) increase the systems complexity relative to purewater ice. By studying the structure and distribution of LVNs with NMR methods, the internal structure properties, including unfrozen water content, characteristic length scale surface to volume ratio (S/V) and tortuosity of ice and frozen porous media can be extracted. With these data, the mean vein size of the LVNs and ice crystal size in the systems can be estimated. An overview of the basic NMR and advanced NMR topics related to relaxation, self-diffusion measurement and magnetic resonance imaging (MRI) were introduced in Chapter 2 and Chapter 3. Chapter 4 presented the physical basis of the ice-solid particulate mixture and explained the application of NMR techniques and analysis methods to this system. The Carr-Purcell-Meiboom-Gill sequence (CPMG) was used to measure the unfrozen water content and T_2 distribution. The Pulsed Gradient Spin Echo (PGSE) method was used to measure the effective diffusion coefficient at varying displacement observation time from 10 ms to 1000 ms. Due to the restricted motion of the protons on the unfrozen water, S/V and tortuosity can be determined by Pade fitting the effective diffusion coefficient (Callaghan, 2011; Hürlimann et al., 1994; Mitra et

al., 1992). Subsequently, the S/V determined from the diffusion data was used to calibrate the T_2 distribution data to calculate a specific surface relaxivity, allowing the S/V to be directly extracted from CPMG relaxation data after calibration.

These methods were applied to characterize the distribution and structure of LVNs in frozen porous media consisting of model packed beds with varying particle sizes and $MgCl_2$ at different concentrations, and was presented in Chapter 5. Seven separate samples were measured to capture the specific LVN properties as a function of salt concentration, particle size and temperature. The results indicate the water content is dominated by the surface energy, which is enhanced by high curvature, when the particle size is small enough. Conversely, the solute effect is the most important process when the particle size is larger. The PGSE and MRI experiments clearly track the significant ice recrystallization process for the ice samples without solid particles. In contrast, the LVN structure changed less in the presence of the solid particles due to the crystal growth limitation imposed by the particles. However, with larger particles (102.2 μm), ice crystals can still grow until they reach the boundary of the solid particles, while the smaller particle (10 μm) pins the ice crystals in the particle lattice inhibiting growth (Lei et al., 2022). Notably, the S/V, vein size and ice crystal size calculated from CPMG data confirmed this. The similar value of S/V from CPMG compared to PGSE over multiple samples confirmed the possibility of utilizing CPMG to calculate S/V after calibration. As the CPMG experiment is more sensitive and can be robustly implemented in low field permanent magnets and down the well bore systems, the NMR techniques can be used to quantify S/V and structure in cold room and field settings (Morriss et al., 1997). This finding extends the application range of NMR techniques to characterize frozen porous media. Overall, unique data on the structure of LVNs in

frozen porous media has been provided, and it lays a solid foundation for future ice structure studies in porous constructs.

As a non-invasive technique, NMR is ideal for tracking the development of LVNs due to ice recrystallization. In Chapter 6, the dynamic structure of LVNs has been studied with and without the influence of IBP as a function of time and salt concentration while the temperature is fixed. The inhibition of the growth of ice crystals by IBP is confirmed. The difference in liquid water content due to different salt concentrations did play an essential role in the structure and distribution of LVNs. However, it did not affect the inhibition feature of IBP significantly at the concentrations measured. In the presence of IBP, the structure of the ice consists of inordinate ice crystals, and small ice crystals around them have been observed (Kaleda et al., 2018). This result suggests the process that in the early stage of ice aging, while IBP binding to several sites of ice crystals, the connectivity of LVNs increases as the S/V doesn't change much, and as time goes by, several big ice crystals with an inordinate shape formed with lots of small ice crystals binding to them via IBP (Kaleda et al., 2018). The findings presented here enhance the understanding of the mesoscale structural impacts of the inhibition mechanism of the specific extracellular IBP from bacterium V3519-10. The S/V has been calculated from CPMG and compared to the value from PGSE as in Chapter 5, and the result again confirms the reliability of this method and shows the possibility of a broader application in frozen porous systems research.

NMR techniques have many advantages in being able to non-invasively study molecular dynamics in opaque systems, but also have some disadvantages in the studies of ice structure and frozen porous media. During CPMG measurements, to limit power deposition from rf excitation energy which can melt the sample, the echo time τ has been set to 400 ms to decrease the

number of echoes and power deposition, which means relaxation faster than <400 ms is only indirectly detected. Consequently, the unfrozen water content measured from CPMG signal intensity will be systematically lower and should be calibrated. Temperature control in high field magnets have a temperature gradient during the measurements as the Avance III Bruker 250 MHZ spectrometer controls the temperature by nitrogen gas flow with active heater control from the bottom of the probe. This temperature gradient may introduce convection to our sample and make the diffusion coefficient measurement inaccurate, as discussed in Chapter 6. To decrease the temperature gradient, the size of the sample in the vertical direction was fixed at around 3.5 cm, and 5mm NMR tubes were used in an 8 mm rf coil, rather than a sample filling 5 mm rf coil, for a more uniform temperature due to enhanced heat transfer at the sample walls. The small size of the NMR samples set a limit to the maximum ice crystal size.

This dissertation contributes firsthand data to the study of biologically impacted ice and frozen media and builds a foundation for future works. It is demonstrated that NMR can be used to monitor ice-binding protein and model packed beds, which can be combined to simulate IBP in soils. The methods also could be applied to monitor frozen food or cryotechnology systems in industry using low magnetic field permanent magnets. Advanced temperature control technology, modified sample holders and permanent magnet custom build systems will allow larger samples with a more uniform temperature to be studied! Potentially the most important extension of this work will be extrusion to the study of ice dynamics in soils and glaciers using permanent magnet well logging or inside out magnet devices (Brox et al., 2015; Kleinberg et al., 1994b; Morriss et al., 1997).

References

Brox, T.I., Skidmore, M.L. and Brown, J.R., 2015. Characterizing the internal structure of laboratory ice samples with nuclear magnetic resonance. Journal of Glaciology, 61(225): 55-64.

Callaghan, P.T., 2011. Translational dynamics and magnetic resonance: principles of pulsed gradient spin echo NMR. Oxford University Press.

Chen, J., Mei, S., Irizarry, J.T. and Rempel, A.W., 2020. A Monte Carlo approach to approximating the effects of pore geometry on the phase behavior of soil freezing. Journal of Advances in Modeling Earth Systems, 12(10): e2020MS002117.

Hardy, S., 1977. A grain boundary groove measurement of the surface tension between ice and water. Philosophical Magazine, 35(2): 471-484.

Hürlimann, M.D., Latour, L.L. and Sotak, C.H., 1994. Diffusion measurement in sandstone core: NMR determination of surface-to-volume ratio and surface relaxivity. Magnetic resonance imaging, 12(2): 325-327.

Kaleda, A., Tsanev, R., Klesment, T., Vilu, R. and Laos, K., 2018. Ice cream structure modification by ice-binding proteins. Food chemistry, 246: 164-171.

Kleinberg, R.L., Kenyon, W.E. and Mitra, P.P., 1994b. Mechanism of Nmr Relaxation of Fluids in Rock. Journal of Magnetic Resonance Series A, 108(2): 206-214.

Lei, P., Young, M.W., Seymour, J.D., Stillman, D.E., Primm, K., Sizemore, H.G., Rempe, l.W. and Codd, S.L., 2022. NMR Characterization of unfrozen brine vein distribution and structure in model packed beds. Cold Regions Science and Technology.

Mitra, P.P., Sen, P.N., Schwartz, L.M. and Le Doussal, P., 1992. Diffusion propagator as a probe of the structure of porous media. Physical review letters, 68(24): 3555.

Morriss, C., Rossini, D., Straley, C., Tutunjian, P. and Vinegar, H., 1997. Core analysis by low-field NMR. The log analyst, 38(02).

REFERENCES CITED

Markets and markets. Antifreeze Proteins Market, https://www.marketsandmarkets.com/Market-Reports/antifreeze-protein-market-264931272.html.

Andersland, O.B. and Ladanyi, B., 2013. An introduction to frozen ground engineering. Springer Science & Business Media.

Ashton, G.D., 1989. Thin ice growth. Water Resources Research, 25(3): 564-566.

Bear, J., 1988. Dynamics of fluids in porous media. Courier Corporation.

Beskow, G., 1947. Soil freezing and frost heaving with special application to roads and railroads.

Bloch, F., 1946. Nuclear induction. Physical review, 70(7-8): 460.

Bramson, A.M., Byrne, S., Putzig, N.E., Sutton, S., Plaut, J.J., Brothers, T.C. and Holt, J.W., 2015. Widespread excess ice in Arcadia Planitia, Mars. Geophysical Research Letters, 42(16): 6566-6574.

Bray, A.J., 2002. Theory of phase-ordering kinetics. Advances in Physics, 51(2): 481-587.

Brown, J.R., Brox, T.I., Vogt, S.J., Seymour, J.D., Skidmore, M.L. and Codd, S.L., 2012. Magnetic resonance diffusion and relaxation characterization of water in the unfrozen vein network in polycrystalline ice and its response to microbial metabolic products. Journal of Magnetic Resonance, 225: 17-24.

Brown, J.R., Seymour, J.D., Brox, T.I., Skidmore, M.L., Wang, C., Christner, B.C., Luo, B.-H. and Codd, S.L., 2014. Recrystallization inhibition in ice due to ice binding protein activity detected by nuclear magnetic resonance. Biotechnology Reports, 3: 60-64.

Brownstein, K.R. and Tarr, C., 1979. Importance of classical diffusion in NMR studies of water in biological cells. Physical review A, 19(6): 2446.

Brox, T.I., Skidmore, M.L. and Brown, J.R., 2015. Characterizing the internal structure of laboratory ice samples with nuclear magnetic resonance. Journal of Glaciology, 61(225): 55-64.

Callaghan, P.T., 1993. Principles of nuclear magnetic resonance microscopy. Oxford University Press on Demand.

Callaghan, P.T., 2011. Translational dynamics and magnetic resonance: principles of pulsed gradient spin echo NMR. Oxford University Press.

Caprihan, A. and Fukushima, E., 1990. Flow measurements by NMR. Physics Reports, 198(4): 195-235.

Carr, H.Y. and Purcell, E.M., 1954. Effects of diffusion on free precession in nuclear magnetic resonance experiments. Physical review, 94(3): 630.

Chen, J., Mei, S., Irizarry, J.T. and Rempel, A.W., 2020. A Monte Carlo approach to approximating the effects of pore geometry on the phase behavior of soil freezing. Journal of Advances in Modeling Earth Systems, 12(10): e2020MS002117.

Chen, J. and Rempel, A.W., 2019a. Ice in granular media, https://gitlab.com/jzchenjz/ice-in-granular-media.

Chen, J. and Rempel, A.W., 2019b. Packing of spherical particles, https://gitlab.com/jzchenjz/packing-of-spherical-particles.

Chen, X., Shi, X., Cai, X., Yang, F., Li, L., Wu, J. and Wang, S., 2021. Ice-binding proteins: A remarkable ice crystal regulator for frozen foods. Critical Reviews in Food Science and Nutrition, 61(20): 3436-3449.

Christner, B.C., Mosley‐Thompson, E., Thompson, L.G. and Reeve, J.N., 2001. Isolation of bacteria and 16S rDNAs from Lake Vostok accretion ice. Environmental Microbiology, 3(9): 570-577.

Dash, J., 1989. Thermomolecular pressure in surface melting: motivation for frost heave. Science, 246(4937): 1591-1593.

Dash, J., Rempel, A. and Wettlaufer, J., 2006. The physics of premelted ice and its geophysical consequences. Reviews of modern physics, 78(3): 695.

De Gennes, P.-G., Brochard-Wyart, F. and Quéré, D., 2004. Capillarity and wetting phenomena: drops, bubbles, pearls, waves, 315. Springer.

Dedovets, D., Monteux, C. and Deville, S., 2018. Five-dimensional imaging of freezing emulsions with solute effects. Science, 360(6386): 303-306.

Defay, R., Bellemans, A. and Prigogine, I., 1966. Surface tension and adsorption. Wiley.

Deville, S., 2017. Freezing colloids: observations, principles, control, and use: applications in materials science, life science, earth science, food science, and engineering. Springer.

Donhowe, D., Hartel, R. and Bradley Jr, R., 1991. Determination of ice crystal size distributions in frozen desserts. Journal of dairy science, 74(10): 3334-3344.

Eide, L.I. and Martin, S., 1975. The Formation of Brine Drainage Features in Young Sea Ice∗. Journal of Glaciology, 14(70): 137-154.

Elster, A.D. and Burdette, J., 1994. Questions and Answers in Magnetic Resonance Imaging, Mosby, St. Louis, MI.

Ewart, K., Lin, Q. and Hew, C., 1999. Structure, function and evolution of antifreeze proteins. Cellular and Molecular Life Sciences CMLS, 55(2): 271-283.

Gibbard, H.F. and Gossmann, A.F., 1974. Freezing points of electrolyte mixtures. I. Mixtures of sodium chloride and magnesium chloride in water. Journal of Solution Chemistry, 3(5): 385-393.

Gregg, S.J., Sing, K.S.W. and Salzberg, H., 1967. Adsorption surface area and porosity. Journal of The Electrochemical Society, 114(11): 279C-279C.

Grimm, R.E., Stillman, D.E., Dec, S.F. and Bullock, M.A., 2008. Low-frequency electrical properties of polycrystalline saline ice and salt hydrates. The Journal of Physical Chemistry B, 112(48): 15382-15390.

Hahn, E.L., 1950. Spin echoes. Physical review, 80(4): 580.

Hardy, S., 1977. A grain boundary groove measurement of the surface tension between ice and water. Philosophical Magazine, 35(2): 471-484.

Hon, W.-C., Griffith, M., Mlynarz, A., Kwok, Y.C. and Yang, D.S., 1995. Antifreeze proteins in winter rye are similar to pathogenesis-related proteins. Plant physiology, 109(3): 879-889.

Hürlimann, M.D., Latour, L.L. and Sotak, C.H., 1994. Diffusion measurement in sandstone core: NMR determination of surface-to-volume ratio and surface relaxivity. Magnetic resonance imaging, 12(2): 325-327.

Kaleda, A., Tsanev, R., Klesment, T., Vilu, R. and Laos, K., 2018. Ice cream structure modification by ice-binding proteins. Food chemistry, 246: 164-171.

Kaptay, G., 2012. The Gibbs equation versus the Kelvin and the Gibbs-Thomson equations to describe nucleation and equilibrium of nano-materials. Journal of Nanoscience and Nanotechnology, 12(3): 2625-2633.

Kleinberg, R., Kenyon, W. and Mitra, P., 1994a. Mechanism of NMR relaxation of fluids in rock. Journal of Magnetic Resonance, Series A, 108(2): 206-214.

Kleinberg, R.L., Kenyon, W.E. and Mitra, P.P., 1994b. Mechanism of Nmr Relaxation of Fluids in Rock. Journal of Magnetic Resonance Series A, 108(2): 206-214.

Latour, L.L., Mitra, P.P., Kleinberg, R.L. and Sotak, C.H., 1993. Time-Dependent Diffusion Coefficient of Fluids in Porous Media as a Probe of Surface-to-Volume Ratio. Journal of Magnetic Resonance, Series A, 101(3): 342-346.

Lei, P., Young, M.W., Seymour, J.D., Stillman, D.E., Primm, K., Sizemore, H.G., Rempe, l.W. and Codd, S.L., 2022. NMR Characterization of unfrozen brine vein distribution and structure in model packed beds. Cold Regions Science and Technology.

Mangiagalli, M., Brocca, S., Orlando, M. and Lotti, M., 2020. The "cold revolution". Present and future applications of cold-active enzymes and ice-binding proteins. New biotechnology, 55: 5-11.

Meiboom, S. and Gill, D., 1958. Modified spin‐echo method for measuring nuclear relaxation times. Review of scientific instruments, 29(8): 688-691.

Mitchell, J., Webber, J.B.W. and Strange, J.H., 2008. Nuclear magnetic resonance cryoporometry. Physics Reports, 461(1): 1-36.

Mitra, P.P., Sen, P.N. and Schwartz, L.M., 1993. Short-time behavior of the diffusion coefficient as a geometrical probe of porous media. Physical review. B, Condensed matter, 47(14): 8565.

Mitra, P.P., Sen, P.N., Schwartz, L.M. and Le Doussal, P., 1992. Diffusion propagator as a probe of the structure of porous media. Physical review letters, 68(24): 3555.

Morriss, C., Rossini, D., Straley, C., Tutunjian, P. and Vinegar, H., 1997. Core analysis by low-field NMR. The log analyst, 38(02).

Nye, J., 1989. The geometry of water veins and nodes in polycrystalline ice. Journal of Glaciology, 35(119): 17-22.

Petrov, O.V. and Furó, I., 2009. NMR cryoporometry: Principles, applications and potential. Progress in Nuclear Magnetic Resonance Spectroscopy, 2(54): 97-122.

Price, P.B., 2000. A habitat for psychrophiles in deep Antarctic ice. Proceedings of the National Academy of Sciences, 97(3): 1247-1251.

Qin, W., Doucet, D., Tyshenko, M. and Walker, V., 2007. Transcription of antifreeze protein genes in Choristoneura fumiferana. Insect molecular biology, 16(4): 423-434.

Raymond, J.A., 2011. Algal ice-binding proteins change the structure of sea ice. Proceedings of the National Academy of Sciences, 108(24): E198-E198.

Raymond, J.A., Christner, B.C. and Schuster, S.C., 2008. A bacterial ice-binding protein from the Vostok ice core. Extremophiles, 12(5): 713-717.

Raymond, J.A. and DeVries, A.L., 1977. Adsorption inhibition as a mechanism of freezing resistance in polar fishes. Proceedings of the National Academy of Sciences, 74(6): 2589-2593.

Rempel, A., 2007. Formation of ice lenses and frost heave. Journal of Geophysical Research: Earth Surface, 112(F2).

Rempel, A., 2012. Hydromechanical Processes in Freezing Soils, Vadose Zone J.

Rempel, A., Wettlaufer, J. and Worster, M., 2001. Interfacial premelting and the thermomolecular force: thermodynamic buoyancy. Physical review letters, 87(8): 088501.

Rempel, A.R. and Rempel, A.W., 2016. Intrinsic evaporative cooling by hygroscopic earth materials. Geosciences, 6(3): 38.

Sen, P.N., 2004. Time‐dependent diffusion coefficient as a probe of geometry. Concepts in Magnetic Resonance Part A, 23(1): 1-21.

Sizemore, H.G., Zent, A.P. and Rempel, A.W., 2015. Initiation and growth of martian ice lenses. Icarus, 251: 191-210.

Sofie, S.W. and Dogan, F., 2001. Freeze casting of aqueous alumina slurries with glycerol. Journal of the American Ceramic Society, 84(7): 1459-1464.

Song, Y.-Q., 2013. Magnetic resonance of porous media (MRPM): A perspective. Journal of Magnetic Resonance, 229: 12-24.

Song, Y.-Q., Cho, H., Hopper, T., Pomerantz, A.E. and Sun, P.Z., 2008. Magnetic resonance in porous media: Recent progress. The Journal of Chemical Physics, 128(5): 052212.

Stejskal, E.O. and Tanner, J.E., 1965. Spin diffusion measurements: spin echoes in the presence of a time‐dependent field gradient. The journal of chemical physics, 42(1): 288-292.

Stillman, D.E., Michaels, T.I., Grimm, R.E. and Harrison, K.P., 2014. New observations of martian southern mid-latitude recurring slope lineae (RSL) imply formation by freshwater subsurface flows. Icarus, 233: 328-341.

Strange, J.H., Rahman, M. and Smith, E., 1993. Characterization of porous solids by NMR. Physical review letters, 71(21): 3589.

Torrey, H.C., 1956. Bloch equations with diffusion terms. Physical review, 104(3): 563.

Valiullin, R. and Furó, I., 2002. Phase separation of a binary liquid mixture in porous media studied by nuclear magnetic resonance cryoporometry. The Journal of chemical physics, 116(3): 1072-1076.

Venkataramanan, L., Song, Y.-Q. and Hurlimann, M.D., 2002. Solving Fredholm integrals of the first kind with tensor product structure in 2 and 2.5 dimensions. IEEE Transactions on Signal Processing, 50(5): 1017-1026.

Wang, C., Oliver, E.E., Christner, B.C. and Luo, B.-H., 2016. Functional Analysis of a bacterial antifreeze protein indicates a cooperative effect between its two ice-binding domains. Biochemistry, 55(28): 3975-3983.

Wang, C., Pakhomova, S., Newcomer, M.E., Christner, B.C. and Luo, B.-H., 2017. Structural basis of antifreeze activity of a bacterial multi-domain antifreeze protein. PLoS One, 12(11): e0187169.

Weeks, W., 2010. On sea ice. University of Alaska Press.

Weeks, W.F. and Ackley, S.F., 1986. The growth, structure, and properties of sea ice, The geophysics of sea ice. Springer, pp. 9-164.

Xu, X., Liu, Y., Cui, Z., Wei, Y. and Zhang, L., 2012. Effects of osmotic and cold shock on adherent human mesenchymal stem cells during cryopreservation. Journal of biotechnology, 162(2-3): 224-231.

Zachariassen, K.E. and Kristiansen, E., 2000. Ice nucleation and antinucleation in nature. Cryobiology, 41(4): 257-279.

Zhu, Z., Zhou, Q. and Sun, D.-W., 2019. Measuring and controlling ice crystallization in frozen foods: A review of recent developments. Trends in Food Science & Technology, 90: 13-25.

Zielinski, L.J., 2004. Effect of internal gradients in the nuclear magnetic resonance measurement of the surface-to-volume ratio. The Journal of Chemical Physics, 121(1): 352-361.